University of Sussex

Liquid phase exfoliation and interfacial assembly of two-dimensional nanomaterials

Sean P. Ogilvie

Submitted for the degree of Doctor of Philosophy
University of Sussex
May 2019

Declaration

I hereby declare that this thesis has not been and will not be submitted in whole or in part to another University for the award of any other degree.

Signature:

Sean P. Ogilvie

UNIVERSITY OF SUSSEX

Sean P. Ogilvie, Doctor of Philosophy

Liquid phase exfoliation and interfacial assembly of two-dimensional nanomaterials

Liquid phase exfoliation (LPE) has been demonstrated to be a powerful and versatile technique for scalable production of two-dimensional (2D) nanomaterials, such as graphene and molybdenum disulfide (MoS_2) which allows for their processing into a wide range of structures. LPE can be understood in terms of the chemical physics of the interactions of the liquid with the nanosheets.

Here, it is shown that the prototypical solvent for LPE of 2D materials, *N*-methyl-2-pyrrolidone, undergoes chemical modification during exfoliation which gives rise to increased absorption and photoluminescence, making it particularly unsuitable for dispersion of photoluminescent nanomaterials such as MoS_2.

A subsequent study identifies the influence of solvent properties on the exfoliation process and presents a model which allows for consistent size selection of few-layer nanosheets from any chosen solvent.

Using this understanding, applications-driven solvent selection can be used to identify alternative solvents which facilitate processing of liquid-exfoliated nanosheets into composite and thin film structures. This approach allows for exfoliation into water-immiscible solvents to enable assembly of liquid-exfoliated 2D materials can be assembled at the interface between two immiscible liquids as solid-stabilised emulsions where the nanosheets act as both stabiliser and functional material. An understanding of the chemical physics of these emulsions is developed in terms of surface energies which allows for both measurement of the surface properties of the stabilising nanosheets and design of emulsions for potential applications as inks, composites, sensors and energy storage devices.

In addition, Langmuir deposition can be used to assemble densely-packed ultra-thin films at the air/water interface. This method is used to prepare few-layer MoS_2 nanosheet networks, which exhibit interesting spectroscopic properties. Furthermore, these films exhibit high conductivity which is attributed to doping by nanosheet edges. The combination of nanoscale film thickness and increased conductivity highlights their potential for optoelectronic devices.

As such, this study demonstrates that, through understanding of exfoliation and size selection, interfacial assembly represents a promising approach for realisation of functional composites and thin films, enabled by ultra-thin interfacial films of 2D nanosheets.

Publications

Elements of this thesis have contributed (in part or in their entirety) to the following publications:

1. Matthew J. Large, **Sean P. Ogilvie**, Sultan Alomairy, Terence Vöckerodt, David Myles, Maria Cann, Helios Chan, Izabela Jurewicz, Alice A. K. King, and Alan B. Dalton (2017) Selective mechanical transfer deposition of Langmuir graphene films for high-performance silver nanowire hybrid electrodes. Langmuir, 33 (43). pp. 12038-12045.

2. **Sean P. Ogilvie**, Matthew J. Large, Giuseppe Fratta, Manuela Meloni, Ruben Canton-Vitoria, Nikos Tagmatarchis, Florian Massuyeau, Christopher P. Ewels, Alice A. K. King, and Alan B. Dalton (2017) Considerations for spectroscopy of liquid-exfoliated 2D materials: emerging photoluminescence of *N*-methyl-2-pyrrolidone. Scientific Reports, 7 (16706).

3. Matthew J. Large, **Sean P. Ogilvie**, Alice A. K. King and Alan B. Dalton (2017) Understanding solvent spreading for Langmuir deposition of nanomaterial films: a Hansen solubility parameter approach. Langmuir, 33 (51). pp. 14766-14771.

4. Matthew J. Large, **Sean P. Ogilvie**, Manuela Meloni, Aline Amorim Graf, Giuseppe Fratta, Jonathan P. Salvage, Alice A. K. King and Alan B. Dalton (2018) Functional liquid structures by emulsification of graphene and other two-dimensional nanomaterials. Nanoscale, 10 (4). pp. 1582-1586.

5. Sebastian Nufer, Matthew J. Large, Alice A. K. King, **Sean P. Ogilvie**, Adam Brunton, and Alan B. Dalton (2018) Edge selective gas detection using Langmuir films of graphene platelets. ACS Applied Materials and Interfaces, 10 (25), pp. 21740–21745.

6. **Sean P. Ogilvie**, Matthew J. Large, Marcus A. O'Mara. Peter J. Lynch, Cheuk Long Lee, Alice A. K. King, Claudia Backes and Alan B. Dalton (2019) Size selection of liquid-exfoliated 2D nanosheets. 2D Materials, doi:10.1088/2053-1583/ab0dc3

7. **Sean P. Ogilvie** et al., High conductivity thin films of liquid-exfoliated MoS_2 nanosheets (in preparation)

8. **Sean P. Ogilvie** et al., Emulsions stabilised by pristine few-layer nanosheets (in preparation)

Acknowledgements

Firstly, I would like to thank Alan for giving me the opportunity to pursue the research career I'd always hoped to, for having the vision to steer a project in what always turns out to be the right direction (it *was* the edges all along...), while trusting me to pursue what I feel is important, and for his continued efforts to convince me that the best science happens after a beer.

I would also like to thank Matt for being the "king of the lab" that he is, for passing a little of that on and for showing me that there's data and understanding to be gleaned from even the most Friday afternoon of experiments. I hope we can continue to bounce ideas off each other wherever we end up.

Thank you to Alice for insisting on getting everyone together in the pub and also for the science discussions, for often being the fresh pair of eyes that notices an important result or where something sits in the bigger picture.

I would like to thank Peter for joining the group at the right time and reassuring me that my exfoliation techniques weren't crazy – and for growing the Gaelic contingent and always reminding me that I can leave my friends behind...

Thanks also to Marcus for making sure there is never a dull moment between enthusiasm, frustration, laughter and hysteria. Never change.

I would like to thank everyone else in Materials Physics; Seb, Giuseppe, Manuela, Aline, Annie, Yuanyang, Manoj, Frank, Abdullah and Conor, for their support.

I am also grateful to our various collaborators, particularly Claudia Backes at Universität Heidelberg for the numerous enlightening discussions at conferences and collaborating on our size selection model.

Thank you to my friends for their support and interest in my PhD; particularly Dave and Tim who explained a lot of physics to me when we were undergrads but also to Oli, Kathryn, Chris, Paul and Selina.

Thanks to my brothers, Michael, Marc and Ciaran, for being younger than me and thereby making me feel like it's ok to be a student for so long and for their interest in my PhD.

To my Mum and Dad, I will always be incredibly grateful for everything they've done to help me and encourage me to get this point. Since deciding I wanted to do a PhD, their continued support and interest made me feel better about all the times they'll have to tell people it's "not that kind of doctor".

Finally, to my wife, Lily, I want to thank you for being there for me from school to university to university to university. Your brilliance every day, whether in teaching, art, proofreading this thesis, being your hilarious self or being determined to "live your best life", makes me want to try to be as half as brilliant at what I do. Your faith and compassion throughout my PhD is the reason I have got this far. You are the most incredible person to have shared this journey with and I'm looking forward to what the future holds.

Contents

List of Figures

Chapter 1

Introduction

Why nano?

The emergence of the field of nanoscience was based on the idea that manipulation of matter on a near-atomic scale could lead to new technologies with unprecedented functionality. Subsequent efforts to achieve this level of nanoscale control led to the invention of the scanning tunnelling microscope [1] and the atomic force microscope [2], with the former successfully used to manipulate individual atoms in 1989 [3].

Around the same time, nanomaterials comprised of tens to thousands of atoms in well-defined low-dimensional structures, such as fullerenes [4] and carbon nanotubes [5], were discovered. Further studies seeking to harness the functional properties of these materials highlighted that nanotechnology could be developed through macroscopic processing. This includes solution processing where the dispersion of isolated nanoparticles in liquids can preserve their pristine properties and facilitate low-cost, scalable and versatile subsequent processing into of a variety of structures with enormous potential for applications.

Such low-cost large-scale processing will be important for applications such as next-generation composite materials and as such will require nanoscale fillers compatible with this processing. Furthermore, wearable or Internet of Things flexible devices will be printed and therefore need to be assembled from functional materials with particle sizes below 1 µm to be compatible with inkjet and other printing techniques. Indeed, nanoscale materials are almost a pre-requisite for solution processing in

order to prepare dispersions of high-density particulates which are stable against reaggregation and sedimentation over timescales of months and small enough to act as low loading level fillers or survive deposition techniques.

Why 2D?

The low-dimensional family of carbon nanomaterials including zero-dimensional fullerenes and one-dimensional carbon nanotubes was completed with the isolation of graphene, the first and only truly two-dimensional (2D) material, by Geim and Novoselov in 2004 [6]. This sparked a renaissance in research into the exfoliation of graphene and related materials into atomically-thin sheets. The properties of specific materials will be discussed in subsequent sections but it is worth considering why high aspect ratio nanomaterials are generally considered to have more promise for applications than isotropic nanomaterials or bulk materials.

Nanomaterials are typically defined as having at least one dimension in the size range 1-100 nm, meaning that isotropic nanoparticles are approximately spherical with a diameter less than 100 nm. Any structure or device based on such materials will often need to be larger than a single nanoparticle, for reasons of absolute performance or properties or for practicality of fabrication or integration. As such, high aspect ratio nanomaterials which exhibit nanoscale confinement in one or two dimensions but have at least one dimension of >100 nm are more suitable for single nanoparticle devices. Furthermore, this high aspect ratio allows the assembly of networks of nanoparticles with low mass per unit area or volume, i.e. reduced percolation thresholds in films and composites compared with isotropic nanoparticles or bulk materials [7]. These properties highlight the potential of 2D materials for applications such as low-cost, flexible ultra-thin coatings and low-loading fillers in macroscopic structures. Being both atomically-thin and high aspect ratio, graphene is the prototypical 2D material where all atoms are at the surface, making assemblies of graphene ideal candidates for applications such as mechanical reinforcement in composites and electrochemical devices, where high specific surface area provides large interfacial areas for stress transfer and charge storage respectively.

Why graphene?

The isolation of graphene from graphite demonstrated exfoliation of stable atomic monolayers and subsequent characterisation identified ballistic electronic transport, resulting in high mobility and conductivity [6]. However, the conductivity of even very high quality graphene is only a factor of three greater than the basal plane conductivity of graphite [8, 9, 10], so while mechanically-exfoliated isolated monolayer graphene is of interest for studies of new transport physics, similar conductivity should be achievable in any suitably assembled graphene ensembles. Furthermore, high conductivity in an atomically-thin material still corresponds to quite large sheet resistance, which can only be reduced further by vertical assembly of graphene, such as in printed networks of liquid-exfoliated nanosheets [8, 11].

Similar arguments can be made about the high thermal conductivity [12] and the high Young's modulus [13] of graphene. These properties are typically most pronounced in isolated monolayers and there is always reduction in network properties due to inter-nanosheet electron or phonon transport (or nanosheet-matrix stress transfer in mechanically-reinforced composites). Nevertheless, liquid-exfoliated nanosheets have intrinsic properties comparable to graphene produced by other methods and the potential to be realised across networks with developments in processing to improve alignment and reduce inter-nanosheet resistance. The prospect of exfoliating nanosheets with high electrical conductivity from a low-cost naturally-abundant raw material has established liquid-exfoliated graphene as a promising material for application in conductive composites and thin films.

Beyond graphene

One of the most useful aspects of the solution processing approach used in this thesis is that it is largely transferable from graphene to other layered materials. The nature of the interlayer bonding means that layered materials have very similar surface properties even if they have very different functional properties. As such, the same techniques can be used to assemble nanosheet networks across the full range of electronic properties; graphene as conductor, MoS_2 and other transition

metal dichalcogenides (TMDs) as semiconductors and BN as insulator. Thermal and mechanical properties give similar scope for design of heterostructure or composite devices. In addition, the sensitivity of the optical properties to size and thickness, particularly for semiconducting nanosheets, is a powerful diagnostic tool, used to understand nanosheet populations and networks thereof throughout this thesis.

Thesis outline

In practise, the greatest challenge is the processing and assembly of these nanosheets into networks which maintain the desired properties of the individual nanosheets. This requires an understanding of the chemical physics of the nanomaterials to optimise their exfoliation and control their assembly for subsequent applications.

This thesis investigates a relatively unexplored area in the overlap between liquid phase exfoliation and interfacial assembly. While the former is a well-developed approach for solution processing of pristine layered materials [14, 15], the latter is more well-studied for more conventionally amphiphilic nanomaterials such as graphene oxide [16]. By confining 2D materials to a pseudo-2D space, interfacial assembly of pristine nanosheets has the potential to preserve exfoliation and surface area, minimise percolation thresholds and isolate ultra-thin nanomaterial films for a range of applications.

This study aims to address three key questions:

- How can we understand exfoliation and size selection of nanosheets to develop a framework for interfacial assembly?
- How can interfacial assembly help to solve current challenges in nanosheet networks?
- How can interfacial assembly allow us to study intrinsic properties of nanosheets?

The properties of interest and methods of exfoliation of these layered materials are discussed in Chapter 2, followed by an overview of the experimental processing and characterisation techniques employed in this thesis, in Chapter 3.

The subsequent experimental chapters seek to develop a framework for solution processing of layered nanomaterials, starting with a study of the degradation during liquid phase exfoliation of the prototypical solvent used for this process, *N*-methyl-2-pyrrolidone (NMP). Chapter 4 addresses the influence of this degradation on the spectroscopic characterisation of nanosheet dispersions.

Given the need for alternative solvents where the NMP degradation might affect subsequent applications, Chapter 5 describes the influence of exfoliation and size selection processes on nanosheet dispersions in different solvents and develops a model to standardise size selection of few-layer nanosheets.

These solvent selection and size selection approaches are employed to facilitate formation of nanosheet-stabilised emulsions in Chapter 6. The properties of liquid emulsions prepared from the exfoliating solvent and water are studied to understand their structure and properties. Subsequently, a range of emulsion compositions are prepared to investigate the stability criteria and orientation of emulsions; whether water-in-oil or oil-in-water based on their surface energies. Importantly, this represents a method for both measurement of the surface energy of the nanosheets and for design of emulsions. The potential for application of emulsions as nanosheet inks is considered, alongside additional methods to control emulsions which may help to realise their applications potential.

Chapter 7 presents a study of MoS_2 thin films as a means to investigate the degree of exfoliation in dispersion and on substrate based on the sensitivity of the optical properties to nanosheet dimensions. Langmuir deposition is employed to allow preparation of ultra-thin, densely-packed nanosheet networks with potential for thin film optoelectronic devices. The conductivity and photoconductivity of these few-layer nanosheet networks is studied and correlated with the nanosheet dimensions.

Together, these studies give new understanding of well-studied materials, solvents and processes which facilitates interfacial assembly to fabricate novel structures based on ultra-thin nanosheet films.

Chapter 2

2D materials and their synthesis

The idea that strongest and most conductive material known to man can be isolated from "pencil lead" has established graphene and related materials as a field where fundamental science could enable step-change developments in technology [17]. While fullerenes and carbon nanotubes are synthetic nanomaterials, two-dimensional (2D) and pseudo-2D nanomaterials can be produced from naturally-occurring layered materials with a wide range of electronic, optical, thermal and mechanical properties [18]. In practise, the range of applications in which 2D materials have been envisaged will require processing that is more scalable and versatile than the Scotch tape method [19]. This chapter will discuss the structure, properties and applications of graphene and related 2D materials, followed by methods for their exfoliation, with a focus on liquid phase exfoliation as a suitably scalable and versatile technique to enable 2D materials to realise their applications potential.

2.1 Graphene

Graphene was the last of the set of different dimensionalities of carbon (3D graphite, 0D fullerenes and 1D carbon nanotubes) to be isolated but is actually considered the parent material from which all other graphitic carbon can be assembled, as shown in Figure 2.1. Graphene consists of a monolayer of carbon atoms arranged in a hexagonal lattice. It is possible to isolate such monolayers from bulk graphite

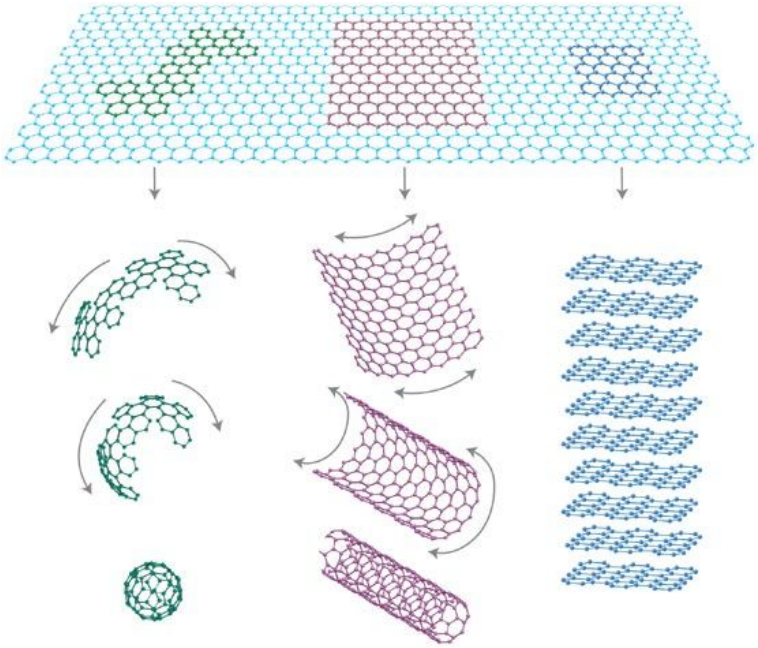

Figure 2.1: Graphene as the parent material of sp^2 carbons; fullerenes, nanotubes and graphite. Image from [20].

because its structure is simply vertically-stacked layers of graphene.

Graphite has been associated with the north west of England since the mid-16th century, with deposits in Cumbria initially used by farmers to mark their sheep, before leading to the establishment of the local pencil industry. Less than 100 miles away (and 450 years later, in 2004) at the University of Manchester, Geim and Novoselov successfully isolated monolayer graphene from graphite in 2004 by micromechanical cleavage [6]. Not only was the monolayer found to be stable, it was demonstrated to be a semi-metal with strong electric field effect and high carrier mobility ($\sim$10000 cm^2/Vs). The simplicity of their exfoliation process using Scotch tape and the potential of graphene and related materials for new physics and applications alike sparked renewed interest in the field of layered materials [21].

The remarkable properties of graphene are as a result of its structure and this is in turn a consequence of the bonding in carbon. The four valence electrons in elemental carbon have a configuration of $2s^2 2p^2$ but tend to form hybrid orbitals between the $2s$ and $2p$ states which facilitate the formation of different structures. In diamond, one of the s orbital electrons is promoted to the p_z orbital to take part in orbital hybridisation to form an sp^3 orbital where four bonds maximise the angle

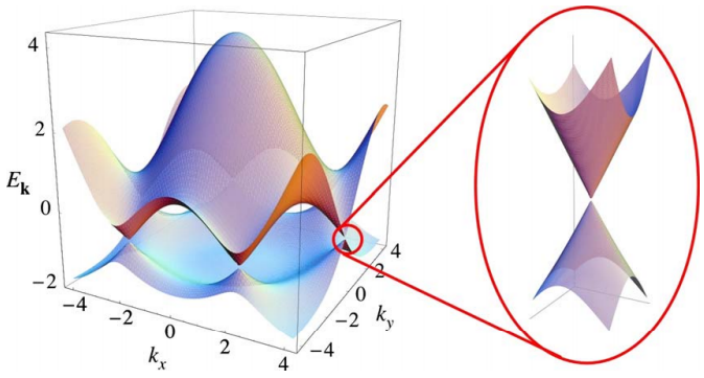

Figure 2.2: Band structure of graphene illustrating linear dispersion relation (Dirac cone) at the K point. Image from [20].

between themselves and result in the tetrahedral zincblende structure. In graphene, only two of the three p orbitals take part in hybridisation to give an sp^2 structure where three bonds can maximise the angle between them as 120° in plane [22]. This gives the hexagonal and layered structure of graphene with the unhybridised p_z orbital responsible for the weak interplanar bonding.

In addition, overlapping orbitals in graphene lead to the formation of σ and π bonds, for s and p orbitals respectively. σ bonds represent delocalised states which facilitate in plane electronic transport [22]. They are also among the strongest chemical bonds which confers the record Young's modulus of graphene [13] due to the high energy of defect formation or dislocation movement. Whereas π bonds have little overlap in the z-axis resulting in highly anisotropic electronic transport [9] and weak interplanar bonding that can be easily overcome to isolate graphene from graphite.

π bonds are however responsible for the unique in-plane electronic properties of graphene, giving bonding and anti-bonding orbitals close to the Fermi level [22]. These orbitals meet at the K-point with linear dispersion relation, as shown in Figure 2.2, making graphene a semi-metal (or zero-gap semiconductor) whose carriers have zero effective mass and therefore ballistic (scattering-free) electronic transport [23]. These electronic properties result in remarkable device-level performance in terms of mobility and conductivity [24, 25], as illustrated in Figure 2.3. However, it is worth

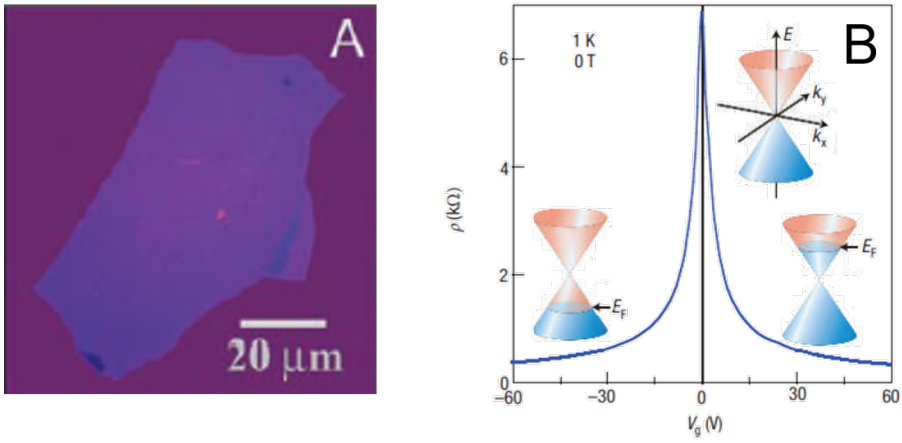

Figure 2.3: Optical micrograph of graphene flake from [6] and electric field effect from [21], showing modulation of 2D resistivity ρ as a function of gate voltage V_g.

noting that these superlative properties are only strictly manifested in single-layer, single-flake, in-plane measurements screened from external influences [26].

It is therefore important to consider how the ensembles of few-layer nanosheets with in- and out-of-plane transport and various external influences studied in this thesis, relate to idealised graphene. Bilayer and trilayer graphene were also reported in Geim and Novoselov's original paper as exhibiting "essentially identical electronic properties characteristic for a 2D semimetal which differed from a more complex (2D plus 3D) behavior observed for thicker, multilayer graphene as well as from the properties of 3D graphite" [6]. While this thickness dependence was in terms of their electric field effect and attributed to screening effects, graphitic multilayers have qualitatively the same semi-metallicity from single-layer graphene to pseudo-infinitely-thick graphite.

The main difference is that overlap of the p_z orbitals gives rise to quadratic (rather than linear) dispersion relations at the K-point near the Fermi level in multilayer structures [20]. As such, carriers with zero effective mass which experience ballistic transport in single-layer graphene have non-zero effective mass and experience increased scattering in bilayers and above. While bilayer graphene has some desirable properties in itself (such as the presence of a band gap for optoelectronics [27]), as a general rule, scattering effects in multilayers result in mobilities and conductivities

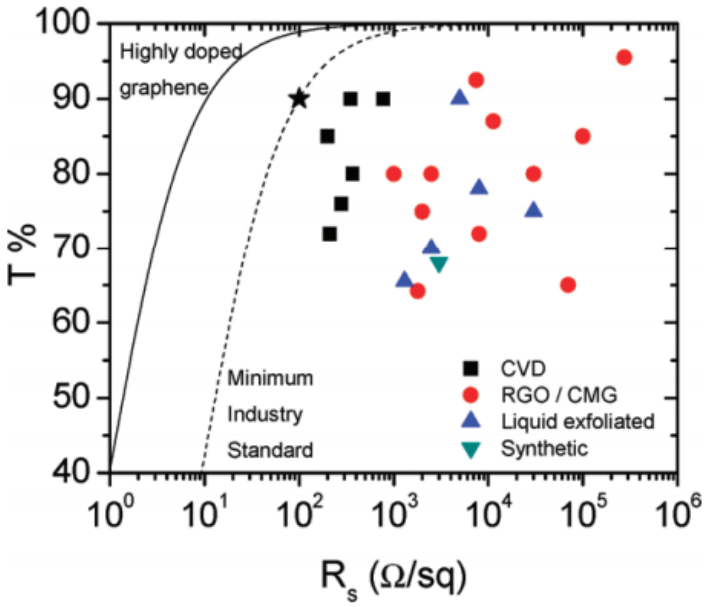

Figure 2.4: Transmittance-sheet resistance plot for various graphene materials, illustrating relative performance mono- and multi-layer materials and comparison of continuous flake (black squares) vs nanosheet networks (red circles, blue triangles). Star represents minimum industry standard for indium tin oxide. Image from [8].

which tend towards those associated with bulk graphite [20, 28, 29, 30, 9, 10].

Nevertheless, most of the properties of graphene are quite robust to increasing layer number, including conductivity ($\sim 10^6$ S/m [9, 8, 10]), transparency [31], high surface area [32], thermal conductivity [33], mechanical properties [34] and processability [35, 14]. This means few-layer graphene remains a material with great applications potential [19]. Few-layer graphene typically finds applications where versatile processing is accepted at the expense of electronic performance.

One application area which allows for comparison of different graphenes and processing techniques is transparent electrodes, where the requirements are of low sheet resistance (<10 Ω/sq) and high optical transparency ($>90\%$, related to film thickness). So while there is no explicit threshold on conductivity or mobility, the sheet resistance must be realised with an effective thickness of less than 4 monolayers [31], meaning a conductivity of $>10^7$ S/m is required. As shown in Figure 2.4, this places nanosheet networks of solution-processed graphenes (from both chemically-modified and pristine graphene) far from the industrial standard for transparent conductors. Even high-quality vapour-phase-deposited graphene does

not offer sufficiently low sheet resistance but highly-doped graphene *is* capable of fulfilling the requirements for this stringent application [8, 10]. This illustrates that the superlative but often thickness-normalised properties of graphene can fall short of performance requirements based on absolute device properties and that few-layer and/or solution-processed graphene can be competitive with higher electronic quality monolayers for such applications.

In reality, applications for graphene are likely to come from across the whole performance-cost-scale parameter space. Printed electronics [36, 11] is one such example; graphene can be used as an electrode material despite the required solution processing typically giving low monolayer content because graphite-like electronic properties are sufficient. In such applications, few-layer graphene takes the form of nanosheets assembled into a network and the properties are determined by the network characteristics as much as the nanosheet characteristics, inter-sheet transport, alignment, etc. These effects will be considered in later sections of this thesis.

Graphene is the most well-known and well-studied layered material, perhaps because of its isolation from an inexpensive and naturally-occurring bulk material, but the family of layered materials is large. Boron nitride (BN) is arguably the closest relative of graphene given its structural similarities and sometimes referred to as "white graphene". While BN is only studied briefly in this thesis, it is worth addressing its relationship to and differences from graphene to understand the transferability of findings and the potential applications.

BN, specifically hexagonal boron nitride, is structurally analagous to graphene with three strong in-plane covalent bonds forming each layer with weak interplanar bonds which have some ionicity due to the alternating stacking of boron and nitrogen atoms [37, 38]. As a result of this structure, BN exhibits thermal [39] and mechanical [40] properties approaching those of graphene. Its electronic properties however differ from graphene as the two different atoms in the unit cell give non-vanishing terms in the band structure. This gives rise to a wide electronic gap of 5-6 eV, making BN an insulator [41].

As such, initial work found atomically-thin BN to be an excellent dielectric substrate for graphene electronics due to its lack of dangling bonds, near-perfect lattice parameter matching and subsequent reduction in electronic scattering and increase in mobility compared with other substrates [42]. Subsequently, BN has been used in dielectric capacitors, both as single-flake [43] and nanosheet-ensemble [44, 45] devices which exhibit dielectric constants as high as 6. BN has also found applications where thermal conductivity without electronic conductivity is desirable, such as thermal management fluids [46].

Indeed, for both BN and graphene, the most significant technological developments based on layered materials are likely to require the versatile processing to enable applications which are not possible with conventional materials. The range of applications of semi-metallic graphene and insulating BN also highlights the potential for "van der Waals heterostructures" for electronics, with the following section introducing the most well-studied class of layered semiconductors to complete the potential building blocks of next-generation all-2D material devices.

2.2 Transition metal dichalcogenides

Transition metal dichalcogenides are a class of layered materials with the chemical formula MX_2 where M is a transition metal and X is a chalcogen. While these materials had been studied and even isolated as monolayers over a decade before graphene [47], the renewed interest around layered materials has established it as a field in its own right where TMDs are often the first "beyond graphene" materials that are considered to have comparable applications potential. The most well-studied of these are the naturally-occurring MoS_2 and WS_2, studied in this thesis, but dozens of TMDs with a range of properties have been studied in recent years [48].

Notably, while TMDs had been studied for many years before their post-graphene renaissance, this was predominantly through chemical exfoliation to produce materials analogous to graphene intercalation compounds [47]. Chemical exfoliation typically involves the intercalation of lithium ions between the layers of a TMD. However, this

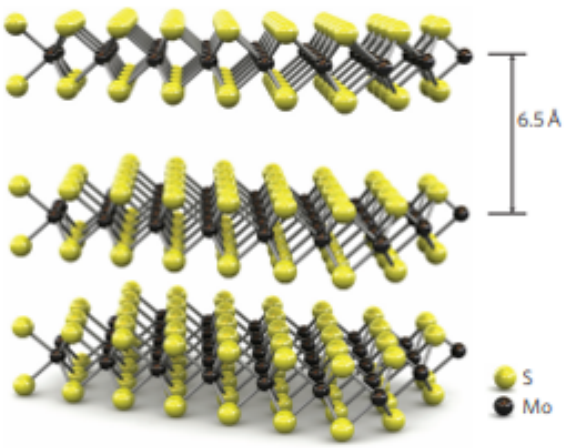

Figure 2.5: Crystal structure of MoS_2. Image from [49].

results in a phase transition from the naturally-occurring and stable semiconducting 2H phase to the metastable metallic 1T phase [50]. Clearly, this is undesirable if the semiconducting properties of the TMD are required for the subsequent application. As such there have been efforts to maintain the 2H phase with post-processing [51] or, more recently, alternative intercalants [52].

MoS_2 is the prototypical layered semiconductor and was successfully isolated by micromechanical cleavage shortly after graphene [23]. It consists of a layer of molybdenum atoms sandwiched between two layers of sulfur atoms, as shown in Figure 2.5 and is therefore not strictly 2D but does exhibit interesting thickness-dependent properties [53, 48]. MoS_2 is a model system to illustrate the effects of quantum confinement in layered materials. The bandstructure of MoS_2 and WS_2 at the Γ point is strongly influenced by sulfur p_z electronic states. The energies of these out-of-plane states are affected by exfoliation from bulk to monolayer with the conduction band minimum raised and the valence band maximum (VBM) lowered, resulting in widening of the indirect gap as expected in a confined system [54]. In the monolayer limit, this indirect gap from the VBM at the Γ point exceeds the direct gap at the K point, resulting in the indirect-to-direct band gap transition characteristic of MoS_2 and WS_2 [53], as shown in Figure 2.6.

It is worth noting that the same confinement effects also result in blueshifting of the direct transition with layer number, albeit to a lesser degree because of the

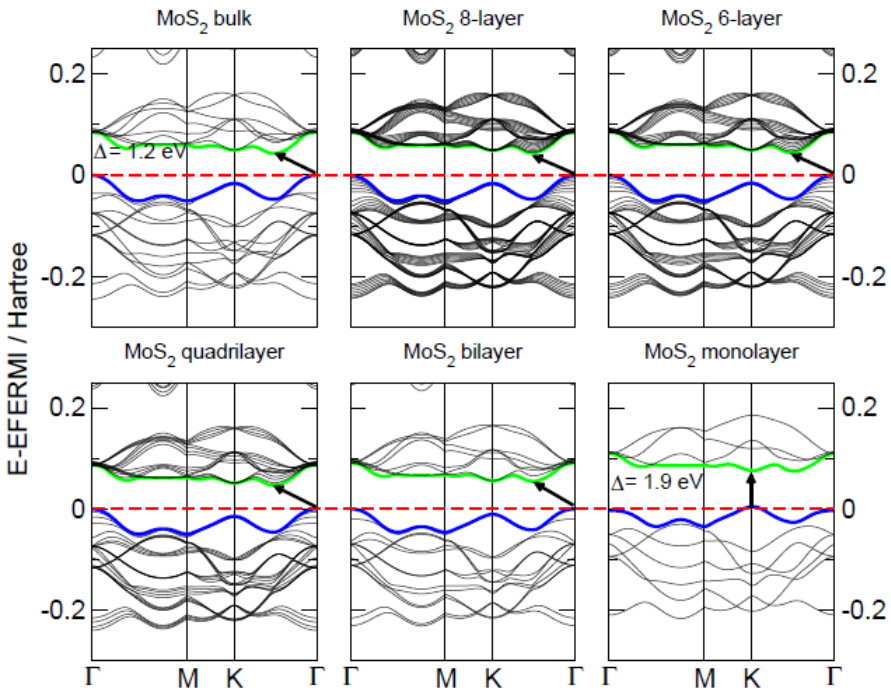

Figure 2.6: Bandstructure of bulk, 8-, 6-, 4-, bi- and, mono-layer MoS_2 illustrating thickness dependence of bandgap and transition to direct gap in the monolayer limit. Image from [54].

reduced contribution of out-of-plane electronic states at the K point (with these being mostly due to localised *d* orbitals of the metal atoms). Indeed, the energy of this transition has even been described as "relatively unchanged" by exfoliation [48]. Nevertheless, characterising this transition has two distinct advantages. Firstly, that its smaller shifts allows unambiguous spectroscopic identification in the visible, compared with the band gap which shifts by over 0.6 eV. Secondly, the direct nature of this transition facilitates correlation of absorption [55, 56] *and* photoluminesence [53, 51] measurements. The robustness of these shifts is the basis of the now-well-established spectroscopic metrics for MoS_2 and WS_2 [56, 57] used in this thesis.

As mentioned above, the direct nature of the band gap of monolayer MoS_2 and WS_2 results in strong photoluminesence (PL) not observed for multilayers [53, 58]. The PL intensity is around 10000 times higher for monolayers as a result of the weak process of phonon-assisted PL in indirect gap multilayers [53], as shown in Figure 2.7. As a result of this strong light-matter interaction [59], monolayer MoS_2 and WS_2 have been studied as a potential active material in optoelectronic devices

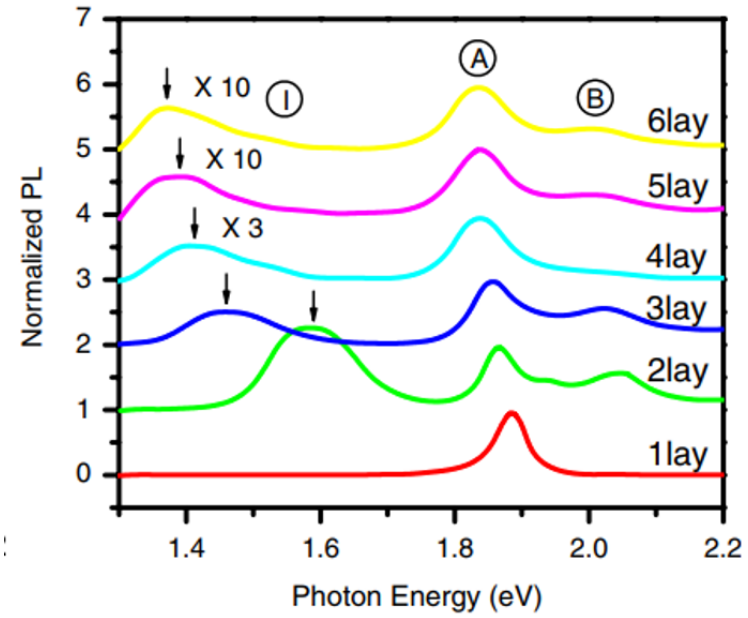

Figure 2.7: Normalised photoluminescence spectra of MoS_2 showing indirect gap, A- and B-exciton PL, labelled I, A and B respectively, redshifting with increasing layer number due to confinement effects. Image from [53].

including photovoltaics [59, 60, 61], photodetectors [62], photodiodes [63], saturable absorbers [64] and electroluminescent devices [65] including light-emitting diodes [66]. While device efficiencies are respectable, the main attraction of 2D materials for such applications is the prospect of ultra-thin flexible devices and, potentially, solution processability. Given that PL is such a robust indicator of the monolayer content of a TMD sample, it has been elusive in high-multilayer-content dispersions typically produced by liquid exfoliation. However, recent studies of monolayer enrichment [56, 67, 57] (discussed further in later sections) demonstrated PL from solution-processed TMDs and illustrated their potential for integration within optoelectronic devices.

While optically-active devices represent a promising application area, the most intense area of study of MoS_2 and WS_2 has been in electrostatically-gated electronics, specifically field-effect transistors [49, 68, 69, 70, 71]. Compared to graphene, which has ultrahigh mobility and zero band gap, semiconducting TMDs have lower but nevertheless reasonable mobilities ($\sim$500 cm^2/Vs, limited by the high effective mass of carriers) but the sizeable band gap results in excellent on-off ratios ($>10^8$). These

findings have helped to establish that 2D materials beyond graphene are likely to have excellent transport properties specifically because of their layered structure; this ensures that they are free from dangling bonds, therefore stable, and have reduced electronic scattering due to reduced interlayer coupling. While carrier mobilities are still lower than for state-of-the-art compound semiconductors, reported values for MoS_2 are comparable with graphene nanoribbons and thin film silicon [49] and their other attributes may make them competitive with III-V materials for certain low-power applications [72].

Another point to consider is the variability of electronic properties reported for MoS_2 and sensitivity to their environment [49, 70]. Bulk MoS_2 actually exhibits mobility of up to 500 cm^2/Vs but this is reduced to 0.1-10 cm^2/Vs for exfoliated layers on substrate and a high dielectric constant passivation layer (such as HfO_2 [68] or Al_2O_3 [70]) is required to restore the mobility to values above that of the bulk. In addition, the contacts are found to have a strong influence on device performance [70, 71]. Such effects can promote or suppress scattering mechanisms which results in quite variable performance even for single-flake devices [73]. Coupled to these extrinsic effects is the well-acknowledged role of sulfur vacancies in doping MoS_2 [71, 74]. These vacancies are prevalent even in MoS_2 exfoliated from bulk crystals and result in Fermi level pinning close to the conduction band [75, 76, 77]. This provides an explanation for both the near-universal observation of n-type semiconduction by MoS_2 [74] and the variability of device mobilities. The prevalence and influence of such defects in WS_2 is less well-studied and perhaps significantly different given that both n- and p-type behaviour often found for this material [78, 79].

The inherent n-doping of MoS_2 is also found to result in a zero Schottky barrier at the interface between monolayer MoS_2 and several common contact metals [49, 71]. This phenomenon also applies, albeit with non-zero but reduced Schottky barrier, to multilayer MoS_2 devices [70, 80, 81] and seemingly solution-processed nanosheet networks [82, 83] similar to those studied in this thesis. These effects and their transferability to nanosheet networks, as well as the potential to manipulate them to

develop novel solution-processed devices, make semiconducting TMDs, particularly MoS_2, exciting materials for a range of appplcations.

2.3 Synthesis of 2D materials

As a result of its remarkable properties, graphene has been hailed as a wonder material for applications including field-effect transistors, transparent electrodes, mechanically-reinforced and conductive polymer composites and energy storage devices [19]. However, it is worth noting that most of these applications require processing which is not possible with graphene as produced by micromechanical cleavage. This may include direct deposition, transfer, or assembly into three-dimensional structures. Such a range of applications will require similarly versatile processing while prioritising high-quality (defect-free) graphene which can be produced by cost-effective and scalable techniques.

Micromechanical cleavage, or the Scotch tape method, is a simple and therefore low cost method of producing very high quality graphene (with only the defects present in the raw material) and relatively large sheets (up to hundreds of microns), but its applicability is severely limited by the lack of scalability [19]. In addition, while materials can be transferred by various techniques, devices are typically fabricated around the as-exfoliated material and fabrication of more diverse structures, such as networks or composite materials, is not possible.

For applications where high electronic quality is required with improved throughput and integration, chemical vapour deposition (CVD) has emerged as an alternative to micromechanical cleavage. CVD involves decomposition of precursor gases over a catalyst under carefully-controlled conditions to minimise defect density. By overcoating with polymer transfer films and etching substrates, CVD materials can be more readily integrated within other structures [19]. In addition, direct deposition of three-dimensional structures by CVD has also been demonstrated [84]. CVD can be considered scalable in that it can facilitate high area applications (such roll-to-roll production of 75 cm transparent electrodes for touch screens [85]) but the

atomically-thin nature of these films mean mass throughput is low and applications which require greater processability remain elusive. Furthermore, the equipment, precursors and high temperatures result in an increased cost of CVD materials compared with other techniques.

Intuitively, low-cost scalable production requires solution processing. In practise, preparation of graphene in solution is challenging because of its poor dispersability; graphite and other bulk layered materials do not spontaneously disperse as for some other colloids nor can they be debundled by mild agitation as for carbon nanotubes. The dispersability of graphite is especially poor in water but can be overcome by oxidising the graphite to form graphite oxide with hydrophilic functional groups allowing exfoliation in water to yield dispersions of graphene oxide (GO) [86]. This process is well developed, relatively low cost and can be scaled to high throughput. However, the addition of functional groups to improve dispersability inevitably influences electronic properties [87].

GO is an inhomogeneous material with conductive sp^2 domains alongside functionalised insulating sp^3 regions [88]. The exact electronic properties are dependent on the degree of oxidation, best characterised by the C/O ratio. For typical C/O ratios in the range 2-5, this results in near-insulating character with a wide band gap of around 3-4 eV and conductivity around 10^{-3} S/m [89]. As such, much research has been carried out to take advantage of the processability of graphene oxide and subsequently reduce it to restore the electronic properties to those of graphene [86, 90, 91, 51]. The most effective of these reduction techniques typically require high temperature under vacuum or harsh chemical treatment such as hydrazine [87, 86]. While less aggressive methods have been developed, such as reduction by vitamin C [92] or microwave treatment [93], it remains challenging to recover high electronic quality with conductivities typically limited to $\sim 10^3$ S/m [87, 89]. This difficulty and the need for post-processing represents a barrier to the adoption of reduced graphene oxide (rGO) for solution-processed applications. In addition, this oxidation-reduction approach is only possible (or at least well-developed) for

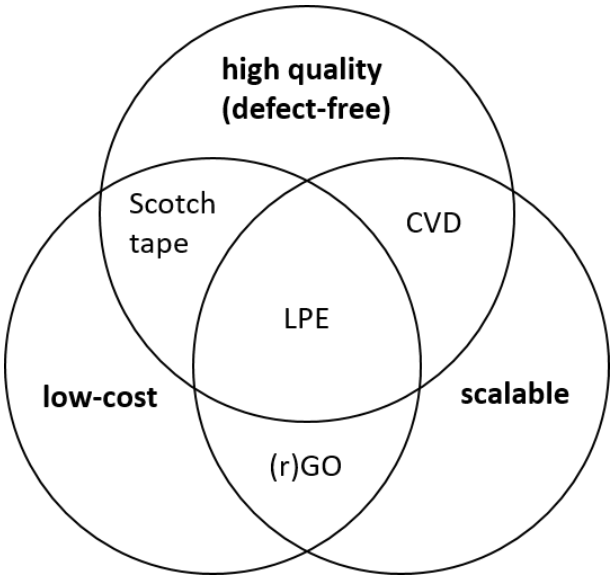

Figure 2.8: Venn diagram illustrating graphene production methods and their attributes.

graphene and is not transferrable to other layered materials and so restricts the range of applications possible with this approach.

Clearly, it would be desirable to have a synthesis technique which combines the simplicity and transferrability of the Scotch tape method, the quality-at-scale potential of CVD and versatility of solution processing associated with GO.

Liquid phase exfoliation (LPE) is an approach developed based on applying hydrodynamic shear forces to suspensions of bulk layered material powders in carefully-selected solvents to exfoliate and stabilise pristine nanosheets [14, 15]. As such, LPE is a powerful technique to enable high-quality nanosheets to be processed into a range of structures for subsequent applications, as illustrated in Figure 2.8.

2.3.1 Liquid phase exfoliation

In order to realise the potential of LPE, it is important to understand how and why it is possible to prepare 2D materials in this way. LPE involves the generation of shear forces in a dispersion of bulk layered material. This approach was first demonstrated for the exfoliation of graphite powder to graphene by ultrasonication [14]. This has subsequently been demonstrated for a wide range of materials including TMDs [15, 94, 95], BN [15], black phosphorus [96, 97] and layered double hydroxides

[98, 99]. It has also been demonstrated using both solvent [100, 101, 95] and aqueous surfactant [102, 103, 94] and polymer solutions [104, 97, 67, 105] as dispersants, with exfoliation techniques including high-shear mixing [106, 107, 108] and high-pressure homogenisation techniques [109, 105, 110].

During exfoliation, local shear forces result in exfoliation of the layered material from bulk to few-layer nanosheets. For exfoliation in aqueous surfactant solutions, this allows the hydrophobic group of the surfactant to adsorb on the nanosheet surface and the hydrophilic group to interact with the surrounding water molecules, reducing of the interfacial energy of the system. However adsorbed surfactant molecules are typically difficult to remove and inhibitive to conductivity if present at the high concentrations used for exfoliation. As such, for certain applications, solvent exfoliation might be preferable. The extent to which this is possible for any given layered material and solvent depends on the energetic cost of creating the additional solid-liquid interface which is related to their chemical composition. The enthalpy of mixing for layered materials in solvents scales with the square of the difference of the square root of their surface energies [14]. Based on analysis of attainable concentrations at which graphene, MoS_2 and BN can be exfoliated into a range of solvents, they are estimated to have very similar surface energy of around 70 mJ/m^2 [15]. This is perhaps surprising given their differences in chemical compositions but not inconceivable given the nature of the van der Waals bonding between their layers.

This argument of surface energy matching broadly describes liquid phase exfoliation of layered nanosheets. Effective solvents are those with surface energies close to the layered materials in the range 60-80 mJ/m^2, which corresponds to surface tensions of 30-50 mN/m [14, 15]. As such, layered nanosheets are considered to be neither polar like water (γ = 72 mN/m) nor non-polar like alkanes (e.g. hexane, γ = 18 mN/m) and are instead somewhere in between. Surface energy for a liquid is simply the sum of the well-defined and directly-measurable surface tension and surface entropy, which take a constant value of $\sim$29 mJ/m^2 for all liquids at room temperature [111]. The most effective solvent for LPE is *N*-methyl-2-pyrrolidone

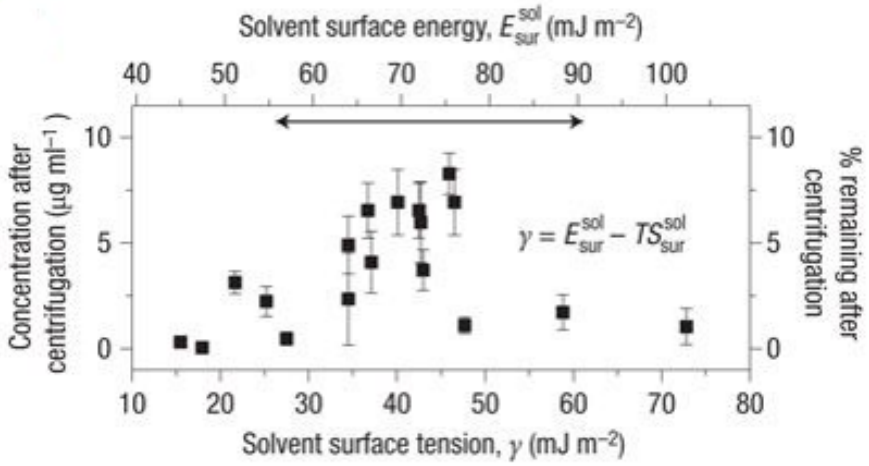

Figure 2.9: Concentration of graphene dispersions as a function of solvent surface energy, showing maximum near 70 mJ/m^2. Image from [14].

(NMP) whose surface energy is very well matched to that of these layered nanosheets [14, 15]. Nevertheless, some solvents very close in surface energy perform poorly and others which are more poorly matched perform reasonably well [14, 101]. This is attributed to the difficulty in describing the chemical interactions of a complex system with only two numbers and this can be improved by using solubility parameter theory. Hansen solubility parameters are an extension of the Hildebrand solubility parameter approach, which is itself related to the cohesive energy density of a molecule [112]. Hansen parameters seek to improve the description of the chemical interactions which contribute to the cohesive energy density by dividing these into dispersive, polar and hydrogen bonding components [112]. The Hansen parameters for a solvent essentially specify a co-ordinate in a three-dimensional parameter space of dispersive, polar and hydrogen bonding $(\delta_d, \delta_p, \delta_h)$, with different co-ordinates for all solvents and solutes. Solvents which are close in Hansen space to a layered material are chemically similar and have a lower enthalpy of mixing, allow them to be more readily dispersed at appreciable concentrations. This solubility metric is known as the Hansen interaction radius and is defined as

$$R_A = \sqrt{(2(\delta_{d,1} - \delta_{d,2}))^2 + (\delta_{p,1} - \delta_{p,2})^2 + (\delta_{h,1} - \delta_{h,2})^2} \tag{2.1}$$

where the factor of two for the dispersive parameters only is included to improve

the sphericity of good solvents, since dispersive parameters span a narrower range of values than the polar and hydrogen components. The concentration attainable in a dispersion can be shown to decay exponentially with the square of the Hansen interaction radius, making it a relatively selective screening approach for solvent selection, although many other factors also influence the exfoliation and stabilisation process. Nevertheless, this approach is found to elucidate many deviations from the predictions of surface energy alone and provides a method for identifying new solvents for exfoliation [113].

One of the most important aspects of LPE is that it has been demonstrated to yield defect-free nanosheets and therefore maintains their electronic quality. By contrast to GO, where defects are deliberately introduced to facilitate dispersion and solution processing at the expense of conductivity, the basal plane of LPE nanosheets are not chemically modified by the exfoliation process, with dispersion achieved by overcoming the interfacial energy penalty through solvent choice or use of surfactant [14, 15, 106]. Transmission electron microscopy finds the nanosheets to maintain excellent long range crystallographic order [14, 15]. Raman spectroscopy can be used to correlate defect modes with the lateral size of nanosheets and therefore can be attributed to edges rather than basal plane defects [114, 115]. This is consistent with inverse gas chromatography measurements which find that high-energy basal plane defects are sparse and only present at the same levels as in the parent graphite [116, 117]. In addition, electrical characteristics and nanosheet mobilities of semiconducting materials are found to be comparable to those produced by other defect-free techniques [118, 79].

Nevertheless, LPE is an ensemble approach which produces nanosheets with broad distributions of lateral size and thickness [14, 15]. Such variations can significantly influence nanosheet and device properties and therefore require characterisation. For most applications it is often desirable to maximise the degree of exfoliation (to increase the surface area, decrease percolation threholds, etc.) while maintaining nanosheet size to minimise the influence of inter-nanosheet junctions. The need for

rapid and representative characterisation of nanosheet size and thickness has led to the development of spectroscopic metrics [56, 57, 115, 119]. This approach allows for estimation of average layer number or lateral size for dispersions of graphene, TMDs or BN based on the influence of physical dimensions on optical or vibrational spectral features, e.g. intensity or wavelength of plasmonic or excitonic features due to interlayer coupling or relative intensities of features associated with defects due to influence of edge sites. These studies illustrate the potential of spectroscopy for both fundamental understanding and practical applicability of ensembles of nanosheets, which this thesis seeks to extend through modelling of size selection in Chapters 5 and 7.

2.3.2 Solution processing

The main advantage of liquid-exfoliated nanosheets is their versatility for solution processing [15]. Their size means they are most often assembled as networks, either alone or as hybrids or composites, which seeks to maintain the properties of the individual nanosheets in macroscopic structures. Nanosheet networks have been fabricated using a range of deposition techniques including spray deposition [102, 44], vacuum filtration [14, 15, 120], inkjet [121, 11, 122, 123, 124, 125, 45] and screen printing [105, 126, 127].

The assembly of graphene into such networks has facilitated fabrication of films with thickness-dependent sheet resistance which can be lower than that of monolayer films [102, 7, 8]. While network conductivities are typically too low for the originally-envisaged application as transparent electrodes [8], thicker films have been applied as electrodes for a range of devices including photodetectors [11], capacitors [44, 45] and transistors [121, 79]. Recently, graphene nanosheet networks have even been demonstrated as antennae for wireless electronics [126, 127].

Such devices often use other 2D materials, including MoS_2 and BN, as semiconducting or insulating materials as solution-processed van der Waals heterostructures. For example, BN nanosheet networks have been utilised as the insulating layer

in dielectric capacitors [44, 45] and transistors [124, 79]. Nanosheet networks of MoS_2 and other semiconducting TMDs have been demonstrated to exhibit good photosensitivity [11, 83, 128] and reasonable performance as field-effect transistors [122, 79, 129], although low conductivity, thick films require electrolytic gating and device performance is typically limited by the presence of charge traps and inefficient inter-nanosheet charge transport [83]. Recently, it has been demonstrated that chemical exfoliation of MoS_2 with novel intercalants can retain the semiconducting phase and allow fabrication of solution-processed films of large sheets which exhibit improved mobility and can be gated electrostatically [52].

Furthermore, hybrid films of nanosheets, such as of graphene and MoS_2, have shown promise for improving conductivity [120], photoresponse [130] or mobility [131] in electronic devices and enabling applications as dye-sensitised solar cell electrodes [132]. In addition to all-nanosheet films, networks can be formed by combining these materials with polymer matrices to form composites. Research in this area has mainly focused on graphene to yield variously flexible, transparent [133], mechanically-reinforced [134, 135, 136, 137], conductive [10] and/or electromechanically-sensitive [138, 139] composite materials. BN nanosheets have also been demonstrated to be an effective filler for mechanical reinforcement [140, 141], while semiconducting TMD nanosheets have been integrated within polymer matrices for photoluminescent composites [67] and non-linear optics [142].

2.3.3 Interfacial assembly

Such composites exhibit impressive functionality but are typically composed of random networks of nanosheets within the polymer matrix. This leads to relatively high percolation thresholds and broad distributions of inter-nanosheet resistance which results in very gradual increases in conductivity above the percolation threshold [10]. Interfacial assembly presents a route to reduction of percolation thresholds by confining nanosheets to a pseudo-2D space which templates their structure in the composite, as previously demonstrated for carbon nanotubes in polymer latex

composites [143]. This approach for solid-liquid interfaces can be extended to liquid-liquid interfaces where solid particles can act to stabilise emulsions, known as Pickering emulsions [144, 145], where a film of the particles reduces the interfacial energy of the system. These have been studied for insulating layered materials such as clays [146, 147] and graphene oxide [148], with some studies of reduced graphene oxide [149] and graphitic multilayers [150, 150, 151]. Subsequent applications include chemical [152] or strain sensing [151] or energy storage devices [149]. However, ultra-low loading composites based on this approach have yet to be realised, with emulsion-polymerised composites exhibiting droplet size-loading level values corresponding to relatively low specific surface areas [153, 150] due to poorly-exfoliated materials and/or overcoating during film formation. Nevertheless, assembly of ultra-thin interfacial films has been achieved at non-emulsified liquid-liquid interfaces, with films subsequently deposited onto substrates. This has been demonstrated for graphene for transparent conductive films [153] and WSe_2 for photoelectrochemical devices [154] but has the potential to be generalised and applied further.

While assembly of functional nanosheets at liquid-liquid interfaces has not been extensively studied, interfacial assembly at the liquid-air interface has received considerably more attention [155]. Formation of a floating film on the surface of a water subphase using a spreading solvent, followed by densification and deposition, is known as Langmuir deposition and has been successfully applied to produce films of GO [156], rGO [157, 158], liquid-exfoliated pristine graphene [159, 160] and chemically-exfoliated MoS_2 subsequently treated to restore the semiconducting phase [161, 162]. These studies typically seek to prepare ultra-thin films to enhance other properties such as transmittance [159, 160] or gas sensitivity [162]. In addition, studies of the optoelectronic properties of films of semiconducting TMD nanosheets have employed a Langmuir-based technique with confined area to yield thicker films [82, 83]. As such, Langmuir deposition has the potential to produce films which are both ultra-thin and have sufficient areal density to exhibit high (bulk-like) conductivity to facilitate applications. The initial aim of this thesis was to use

Langmuir deposition to negate the thickness-dependent conductivity scaling observed for spray- or inkjet-deposited films [7, 11] with a view to application in printed nanosheet network transistors where the improvements on the current state-of-the-art, based on electrolytic gating [79, 129], could be realised by electrostatic gating of these ultra-thin films.

The physics common to assembly at both liquid-liquid and liquid-air interfaces, that this thesis seeks to develop, is that of spreading at three-phase boundaries. Fluids which are immiscible (such as water and solvent or water and air) are so because they are sufficiently chemically different in terms of cohesive energy density, surface tension, etc. Such large mismatches in surface tension mean that liquid-liquid and liquid-air interfaces can be manipulated to form films of carefully-chosen third phases. Essentially, this third phase must exhibit spreading behaviour at the interface which arises as a result of the third phase partially wetting both immiscible phases, rather than preferentially wetting one or the other. Such three-phase interfaces are typically analysed by considering the force balance as illustrated in Figure 2.10. For liquid-liquid interfaces (emulsions), the third phase is the nanosheet stabiliser itself as shown in Figure 2.10(a) and (b), where the spreading criteria are that the water must spread at the solid/oil interface and the oil (solvent) must spread at the solid/water interface. In this case, the forces can be considered collinear and so-called spreading coefficients can be defined as

$$S_{so} = \gamma_{so} - \gamma_{sw} - \gamma_{ow} \tag{2.2}$$

$$S_{sw} = \gamma_{sw} - \gamma_{so} - \gamma_{ow} \tag{2.3}$$

where S_{so} and S_{sw} are the spreading coefficients for the solid/oil and solid/water interfaces respectively and γ_{so}, γ_{sw} and γ_{ow} are the interfacial energies of the solid/oil, solid/water and oil/water interfaces respectively.

The criterion is typically that these must both have the same sign (negative or positive) for stable emulsion formation, which places constraints on the interfacial

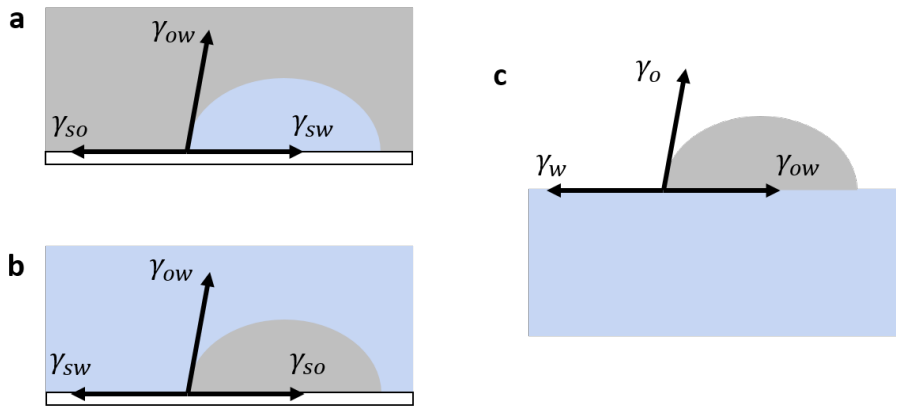

Figure 2.10: Three-phase boundaries associated with interfacial assembly: (a) oil at solid/water interface, (b) water at solid/oil interface and (b) oil (solvent) at air/water interface.

energies of the constituents and presents a route towards nanosheet-stabilised emulsion design and studies of the surface properties of the nanosheets themselves.

For liquid-air interfaces, such as those involved in Langmuir deposition, the third phase is the spreading solvent which acts as a carrier for the nanomaterial. In this case, the solvent must wet the air/water interface in order to form a thin layer and evaporate to leave the nanomaterial trapped at the interface. As such, this three-phase boundary defines the interfacial energy of solvents which are suitable for Langmuir deposition. For both emulsions and Langmuir films, this thesis aims to develop understanding of the physics of spreading and its relation to the surface and interfacial properties of liquid-exfoliated nanosheets in order to facilitate applications of these assemblies.

Chapter 3

Processing and characterisation techniques

This chapter will introduce the most important processing and characterisation techniques used in this thesis, outlining their working priniciples and relation to the studies performed.

3.1 Ultrasonication

Ultrasonication is the process of agitating a liquid or dispersion using high-frequency acoustic energy. This is typically achieved using an ultrasonic bath or ultrasonic probe where a transducer is electrically driven to oscillate at an ultrasonic frequency (∼20 kHz) to generate pressure waves in the liquid medium. Such variations in pressure results in ultrasonic cavitation, where bubbles are formed and manipulated by the applied ultrasound. Cavitation can be classified as either inertial or stable, based on whether the ultrasound causes the bubbles to collapse violently (inertial), resulting in localised extremes of pressure and temperature, or oscillate periodically (stable). In either case, cavitation exerts hydrodynamic shear forces on the liquid and any dispersed particulates, which are sufficient to result in both exfoliation and scission of layered materials. While there have been some studies of controlled acoustic cavitation for dispersion of nanomaterials [163], ultrasonication is widely

used for liquid phase exfoliation of layered materials with little attention paid to the mechanism (or consequences thereof) of the process.

In this study, probe ultrasonication (Sonics Vibra-Cell VCX130) is used routinely for liquid phase exfoliation as a means to supply the high energy required to cut starting materials into more exfoliable particles to lower the interfacial energy required for exfoliation. In addition, in Chapter 4, the influence of sonication-induced chemistry on the prototypical solvent for liquid phase exfoliation is investigated. In Chapter 5, the power output from the ultrasonic probe is correlated with the viscosity of various solvents to study how viscosity affects the yield of ultrasonic exfoliation processes.

3.2 Centrifugation

For a number of reasons, liquid phase exfoliation can be a relatively low-yield low-concentration process. This can in part be attributed to brute force exfoliation methods which must supply the high energies required for exfoliation events at a frequency which results in reasonable yields while not supplying such high energy as to result in excessive scission. In addition, the ultra-thin nature of exfoliated nanosheets means that any unexfoliated crystallites, even in the highest yield processes, constitute a significant proportion of the mass and volume in the dispersion. As such, size selection methods are required to separated the desired few-layer nanosheets from unexfoliated material. Given the small mass but appreciable lateral size of few-layer nanosheets, they are known to be far more stable against sedimentation than unexfoliated crystallites. Centrifugation is a well-established method to accelerate this sedimentation to allow high-throughput size selection of nanosheets. By subjecting a dispersion to high-rpm rotation, the relative g-force experience by dispersed nanosheets is increased and few-layer nanosheets can be isolated within minutes.

Recently, it has been demonstrated that multi-step centrifugation can be used to isolate fractions of a population of nanosheets as a function of their size [57]. Known as liquid cascade centrifugation (LCC), this approach involves successively

sedimenting different fractions under increasing relative g-force and redispersing these to produce samples. This method has the advantage of producing narrower size distributions independently of the initial population and allows for concentration and/or solvent transfer of the nanosheets. As such, LCC is utilised throughout this thesis as a powerful technique for size selection and solvent transfer.

3.3 Microscopy

3.3.1 Atomic force microscopy

One of the challenges of studying ensembles of nanoparticles is that there are inevitably distributions of sizes which influence material properties and performance. In addition, the structures of assembled networks cannot be measured or studied at sufficient resolution by optical microscopy. As such, atomic force microscopy (AFM) is employed for well-calibrated high-resolution topographic characterisation of nanosheets and networks thereof.

In AFM, a cantilever with a sharp tip is rastered across the sample surface and the influence of the sample-tip interactions on the deflection of the cantilever are measured. Readout is achieved by monitoring the reflection of a laser source from the back of the cantilever onto a spatially-resolved photodiode detector as shown in Figure 3.1. This is calibrated with a piezoelectric sensor in the z-axis to allow accurate height determination. These measurements are made point by point to build a map of the surface topography of the sample.

Furthermore, it is possible to extract additional information from a single scan by driving the oscillation of the cantilever at its resonant frequency such as in tapping mode or various proprietary "peak force" modes, such as with the Bruker Dimension Icon instrument used in this study. In tapping mode, the phase shift between the driving oscillation and the feedback provides indicative mechanical characterisation, showing contrast between soft and hard materials. In peak force AFM, multiple force-distance for the oscillation of the tip are recorded at each point and processed to

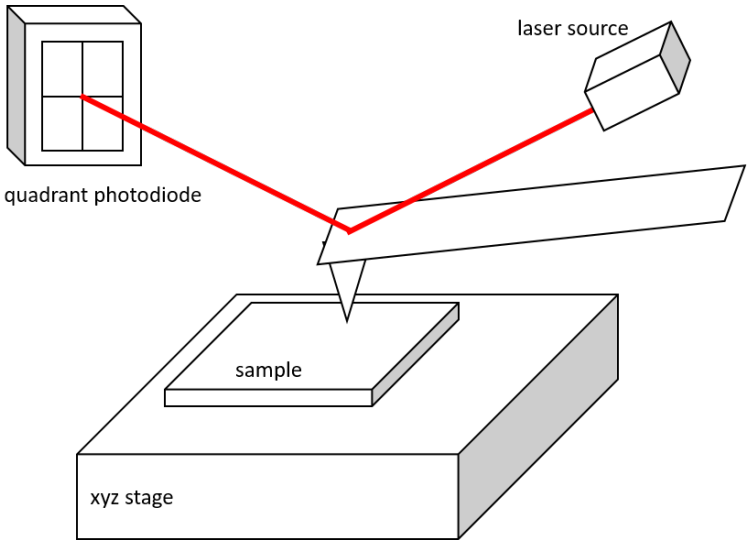

Figure 3.1: Schematic of atomic force microscopy.

extract potentially-quantitative mechanical information including modulus, adhesion and dissipation. These additional channels can be particularly helpful in identifying unexpected or undesired species which often have distinct mechanical properties to the nanomaterial of interest.

In this study, AFM (Bruker Dimension Icon) is utilised to visualise such species (NMP residue on the surface of nanosheets), perform statistical length and thickness characterisation of individual nanosheets and to determine the density and, more importantly, thickness of nanosheet networks down to tens of nanometres.

3.3.2 Scanning electron microscopy

While AFM facilitates well-calibrated high-resolution imaging of a sample surface, it is limited to relatively small areas (<100 µm) and slow scan rates. By contrast, scanning electron microscopy (SEM) allows rapid imaging of conductive samples over length scales from nanometres to hundreds of microns.

The working principle of SEM is that an electron beam is accelerated at high voltage (typically 1-10 kV) penetrates the sample surface to a depth of around 1 µm with a range of interactions resulting in signals that can be used to image with higher spatial resolution than optical microscopy. The most common imaging mode is secondary electron imaging where the intensity of electrons ejected from

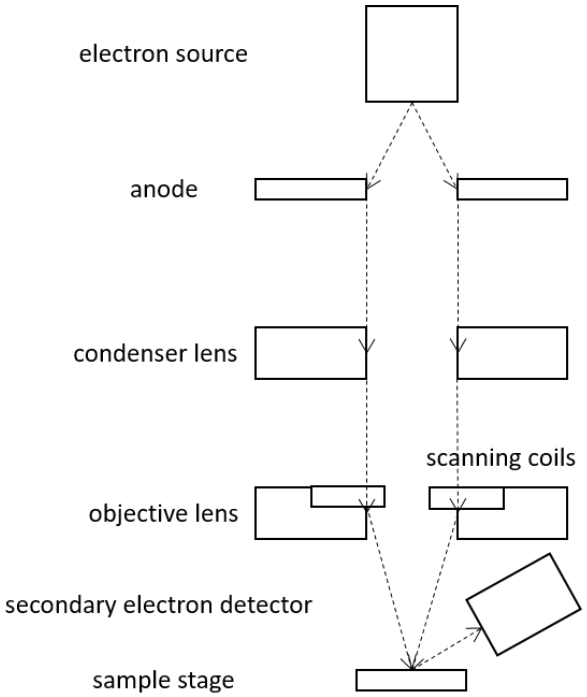

Figure 3.2: Schematic of scanning electron microscopy.

the sample surface with energies <50 eV is mapped to image the structures from which they originated. This allows high resolution topographic imaging because such low-energy electrons can only escape from close to the sample surface. It is also worth noting that non-conductive material such as organic residues are often electron-transparent due to their weak interaction with the primary beam and may not appear at all in SEM. However, if such materials are present is higher quantities, such as in low-conductivity composites, imaging can be challenging due to charging effects, especially at higher voltages required for high resolution.

SEM also has some chemical sensitivity with primary electrons backscattered with a scattering cross-section corresponding to the atomic number of the scattering centre in the sample. This has the potential to enhance contrast between low atomic number (e.g. polymer matrices/binders) and higher atomic number phases (e.g. metal-containing fillers). In addition, SEM can be used for quantitative chemical imaging due to the generation of X-rays in the samples in the presence of electron beam. Displacement of core level electrons may result in transitions of valence electrons to fill the vacancy and emission of an X-ray of characteristic energy, which

can be detected to determine the elemental composition.

In this study, SEM (Zeiss SIGMA) is used for the combination of capabilities and the potential for rapid magnification to image over a wide range of length scales is employed to confirm the structure and uniformity of films over such areas.

3.4 Spectroscopy

3.4.1 UV-visible extinction spectroscopy

UV-visible extinction spectroscopy is the technique of measuring the extinction (combined absorbance and scattering) as a function of wavelength. This is typically correlated with some known optical properties of the materials (extinction coefficient, plasmon or exciton wavelength, etc.) to characterise sample properties (concentration, layer number, thickness, etc).

A UV-visible spectrometer consists of a broadband white light source which is monochromated to allow single-wavelength illumination. The monochromated light is passed through a beam splitter to create two parallel beams to allow measurement of sample and reference simultaneously. The fraction of the light intensity which is transmitted is measured by photodiodes. A baseline measurement is performed to record the intensity of the incident light as a function of wavelength. Subsequently, the sample (usually either a dilute dispersion or semitransparent film on substrate) and a reference (either the pristine solvent used in the dispersion or the substrate on which the sample is deposited) are measured and their the difference in their transmittances attributed to the dispersed material or deposited film.

In practise, it is often more convenient to characterise the extinction of samples, related to transmittance by $A = -log_{10}(T)$. As a result of the Beer-Lambert law, extinction can be quantitatively relate to the concentration of the sample, the path length through the cuvette and its extinction coefficient to allow measurement of this concentration through the equation $Ext = C\epsilon l$. In the case of films, the extinction coefficient can be defined and measured to allow subsequent characterisation of film

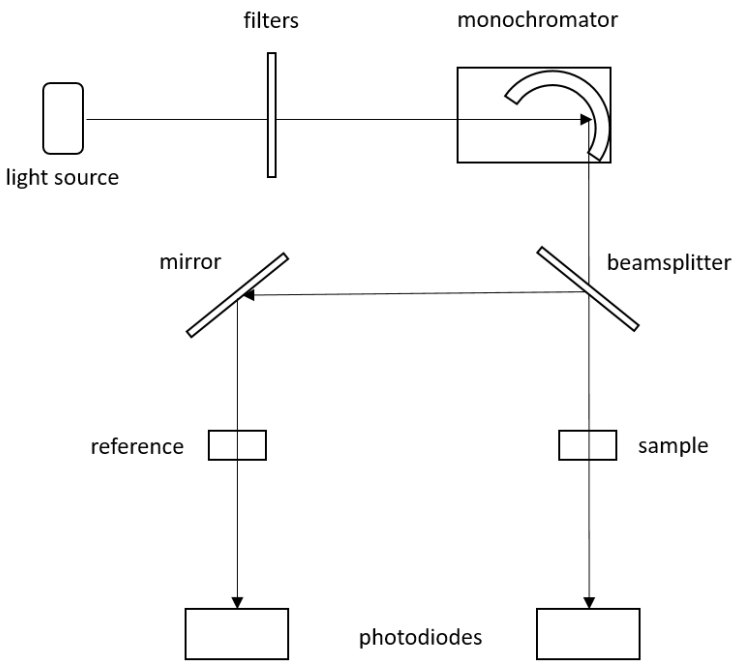

Figure 3.3: Schematic of UV-visible extinction spectroscopy.

thickness, although this is likely to be affected by sub-unity area coverage or porosity. In addition, UV-visible extinction spectroscopy provides indirect measurement of the energies of electronic transitions in a material, observed as local peaks in the spectra. As such, UV-visible spectroscopy (Shimadzu UV3600Plus spectrometer) is used to confer information about the nature of the material such as degree of exfoliation and thus have been developed into spectroscopic metrics for layer number and lateral size for a number of 2D materials [56, 115, 119], which are employed in this thesis.

3.4.2 Photoluminescence spectroscopy

Photoluminescence (PL) spectroscopy is the measurement of light emitted by a material under illumination as a function of emission wavelength. PL is a phenomenon associated with direct-gap semiconductors where emission can occur without the need for phonon transfer. The measurement is technically similar to extinction spectroscopy but spectrometers are often arranged in a right-angle geometry to minimise the incident light transmitted into the detector. For fixed excitation wavelength, the PL intensity is measured as a function of wavelength to determine the peak and width of the emission profile. When this has been identified, the measurement can be

performed in reverse, measuring the intensity at the peak emission wavelength as a function of the excitation wavelength, to ascertain the energy of the transition which is responsible for the PL. These measurements can even be formed as a continuous 3D scan where excitation and emission wavelength and PL intensity can be plotted as a colour map containing all of the information about the process. In this thesis, PL spectroscopy (Shimadzu RF-6000 spectrofluorometer) is used to characterise both monolayer MoS_2 nanosheets in dispersion and the anomolous emission from degraded solvent identified in Chapter 4.

3.4.3 Raman spectroscopy

Raman spectroscopy is a characterisation technique based on inelastic scattering of incident light by excitation of vibrations in a crystal or molecule. Most light scattering is elastic Rayleigh scattering which simply affects the number of photons transmitted or reflected, such as the scattering contribution to extinction spectroscopy or the λ^{-4} dependence that is responsible for the blue colour of the sky. By contrast, the Raman effect is far less prevalent (only affecting about 1 in 10^7 photons) but actually modifies their energy. This is achieved by an incident photon exciting a system from the electronic ground state to an electronic excited virtual state, followed by relaxation to an vibrational state just above the ground state. This results in scattering of a photon with an energy reduced by the energy difference between the ground and vibrational state, i.e. the energy of the vibrational mode as shown in Figure 3.4. This version of events, where the scattered photon is redshifted is known as Stokes Raman scattering. It is also possible for a system already in an excited vibrational state to transfer energy to the photon, via a virtual state, by relaxing into the ground state. This results in the scattered light being blueshifted and is known as anti-Stokes Raman scattering but occurs at a reduced intensity due to the lower number of molecules in the vibrational excited state at any given time.

In addition, because the vibrational modes of a molecule have well-defined energies related to the distortion of the bonds between atoms, Raman scattering has evolved

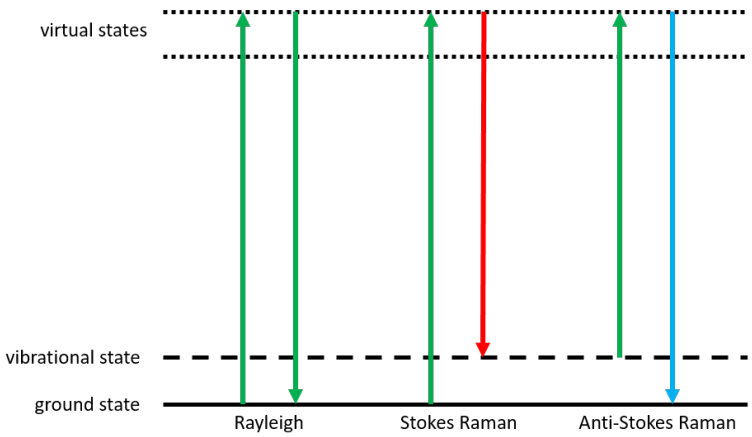

Figure 3.4: Schematic of energy levels involved in Raman spectroscopy.

into a chemical spectroscopy where molecules and nanoparticles can be identified by their vibrational signatures. A Raman spectrometer typically consists of an optical microscope to identify the sample with visible wavelength laser excitation to illuminate. A series of filters, gratings and a CCD detector are then employed to measure the intensity spectrum of the Raman scattered light free from the influence of the excitation source. The measured spectrum is outputted as a function of Raman shift, the difference in wavenumber between the excitation and scattering, which can be correlated with well-known modes to identify or characterise the material. 2D materials are particularly Raman active and the frequency and intensity of their Raman modes is often sensitive to their layer number and lateral size due to interlayer coupling and the effect of defects respectively [164, 57, 115]. Therefore, Raman spectroscopy (Renishaw inVia Raman spectrometer) is utilised in this thesis for liquid-exfoliated nanosheets where there can be broad distributions of size and thickness which must be characterised to understand their influence on material properties.

Chapter 4

N-methyl-2-pyrrolidone: Degradation during exfoliation

N-methyl-2-pyrrolidone (NMP) has been shown to be the most effective solvent for liquid phase exfoliation and dispersion of a range of 2D materials including graphene, molybdenum disulfide (MoS_2) and black phosphorus. However, NMP is also known to be susceptible to sonochemical degradation during exfoliation. It is found that this degradation gives rise to strong visible photoluminescence of NMP. Sonochemical modification is shown to influence exfoliation of layered materials in NMP and the optical absorbance of the solvent in the dispersion. The emerging optical properties of the degraded solvent present challenges for spectroscopy of nanomaterial dispersions; most notably the possibility of observing solvent photoluminescence in the spectra of 2D materials such as MoS_2, highlighting the need for stable solvents and exfoliation processes to minimise the influence of solvent degradation on the properties of liquid-exfoliated 2D materials.

4.1 Emerging absorbance and photoluminescence

N-methyl-2-pyrrolidone (NMP) is the prototypical solvent for dispersion of a range of carbon nanomaterials including fullerenes [165], conjugated polymers [166], nanotubes [167] and graphene [14]. This general applicability is attributed to the matching of

surface energy and Hansen solubility parameters with these materials [168, 169, 113]. This results in low enthalpy of mixing and allows individualised fullerenes, nanotubes and nanosheets to be dispersed at high concentration. Consequently, there is renewed interest in NMP for 2D materials beyond graphene such as molybdenum disulfide (MoS_2) and black phosphorus. These layered materials require solvents which enable exfoliation from the bulk powder and stabilisation against restacking. While the surface tensions and Hansen parameters of these materials are difficult to measure directly, and are inherently dependent on the technique, MoS_2, black phosphorus and many other layered materials can be easily exfoliated into NMP [15, 170].

While clearly an effective solvent, NMP is also known to be very susceptible to sonochemical polymerisation [171] and degradation [172] under the standard processing techniques for exfoliation of 2D materials. In addition, the yield and degree of exfoliation are also sensitive to the concentration of dissolved oxygen and water in the solvent [172, 173, 174]. Such sensitivities indicate that liquid phase exfoliation in NMP is not simply described by solubility parameter theory. The process involves chemical modification of the solvent, generating degradation and polymerisation products which influence the exfoliation process and results. While this may be desirable, the nature of these sonochemical processes can result in a wide variety of products which are difficult to characterise, and may be present as residual contaminants which influence the properties of the exfoliated nanosheets. The influence of degradation during exfoliation may lead to considerable variation of the performance of NMP as a solvent for a given nanomaterial, and potentially skewing of the measured surface energy and solubility parameters of the nanomaterial towards those of the pristine NMP [14].

Furthermore, it has been noted that the optical properties of NMP are also influenced by its degradation, with yellowing of the solvent usually attributed to increased scattering of sonication products [171]. In addition, exfoliation yield and optical absorbance of NMP have also been acknowledged to vary with the age of the solvent [172]. Optical spectroscopy of NMP dispersions is further complicated, albeit

rarely acknowledged in the literature on nanomaterials, by weak photoluminescence (PL) of the solvent [175, 176]. This PL has been found to be the enhanced with degradation, with an increase in the overall intensity and the influence of a redshifted component in both aged samples and sonicated samples. The absorbance and photoluminescence of the degraded NMP present challenges for spectroscopy of nanomaterial dispersions, with the features still observed in as-received NMP and their influence exacerbated by the sonochemical degradation processes during exfoliation of the nanomaterial.

The initial motivation for this study was the observation of visible yellowing of NMP samples with age as previously acknowledged by others [172]. Figure 1(a) shows UV-visible extinction spectra for NMP samples stored in closed containers, in the dark and under ambient conditions for one, four and nine years. The samples were not externally treated in any way. Similar discolouration is also observed for sonicated NMP, hereafter referred to as NMP(s), produced from as-received NMP (HPLC grade, >99% purity). It is evident that such changes arise from increased optical absorption in the wavelength range below 450 nm.

Given that NMP has been reported to be weakly photoluminescent [175], the samples were illuminated with a 405 nm laser. Under this excitation, all samples were observed to exhibit strong blue-green photoluminescence with PL intensity clearly increasing with both ageing and sonication of the NMP, as shown in the inset photographs in Figure 4.1. While the differences in absorbance between the samples at this wavelength are small, the differences in PL intensity are significant and therefore not simply due to the increasing absorbance. This suggests that the increasing photoluminescence is due to the emergence of new species whose concentration or PL efficiency increases with degradation. Having made these observations in the aged samples, the sonicated samples were prepared to study degradation in a more controlled and practically-relevant manner.

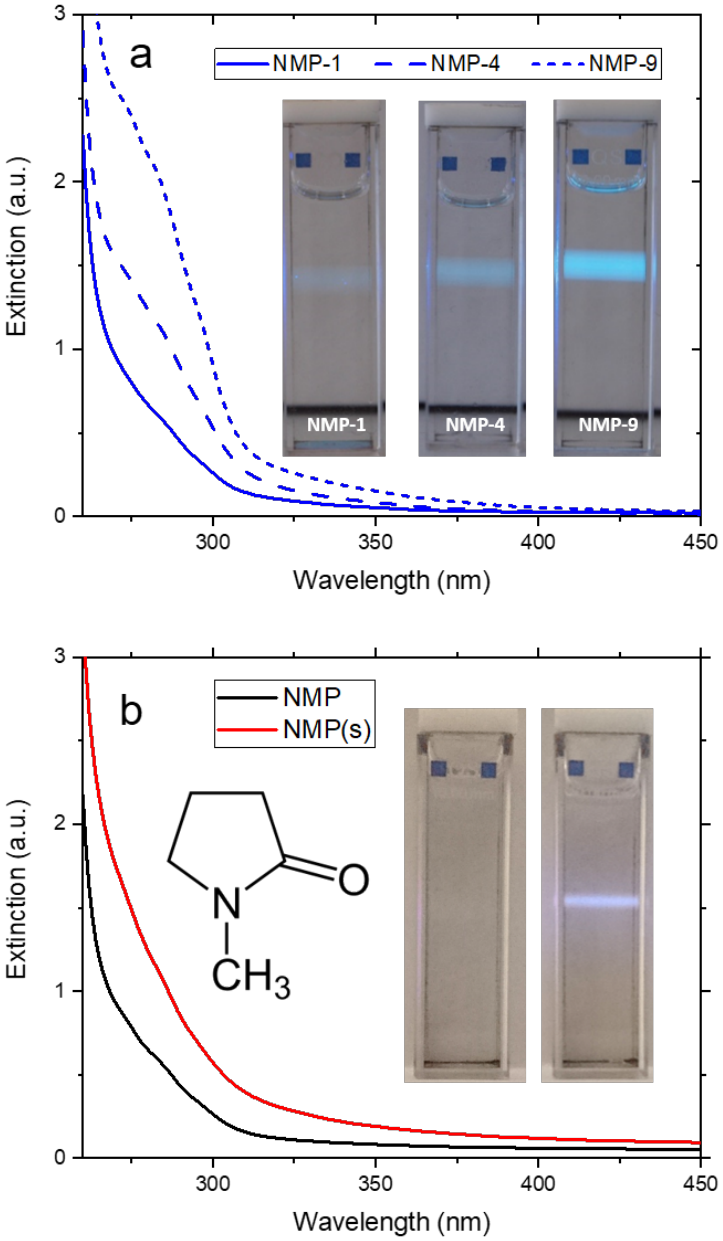

Figure 4.1: (a) UV-visible absorption spectra of NMP showing extinction below 450 nm increasing with the age of the NMP, for NMP-1, NMP-4 and NMP-9 (aged for 1, 4 and 9 respectively). Inset: Photographs of NMP-1, NMP-4 and NMP-9 exhibiting strong blue-green photoluminescence under illumination with 405 nm laser pointer. (b) UV-visible absorption spectra for as-received NMP and sonicated NMP(s). Inset: chemical structure of NMP and photographs of NMP and NMP(s) exhibiting similar blue-green under illumination with 405 nm laser pointer.

4.2 Chemical characterisation

Raman spectroscopy was performed with laser excitation at 532 nm to compare the vibrational modes of the different samples and identify any new species present. These spectra show that NMP and NMP(s) have indistinguishable vibrational modes with fixed peak positions and intensities (Figure 4.2) which are also in excellent agreement with the solvent data sheet.

Subsequently, ^{1}H nuclear magnetic resonance (NMR) spectroscopy was performed to identify any covalently-modified species which are present at trace levels and/or too similar in their vibrational modes to be detected by Raman spectroscopy. In addition to the expected proton peaks for the NMP, the NMR spectra show a number of peaks present at around 0.1% by number. The peaks with chemical shifts of around 5 ppm are attributed to alkenyl protons, suggesting the formation of RC=CH_2 species, while the peaks around 0.9 ppm correspond to protons in a methyl group. These characteristic features are also observed in a previous study of sonochemical degradation of NMP which proposes a mechanism for formation of an enamine species (-N-C=C-) which undergoes polymerisation to form oligomeric nanoparticles [171]. The observation of similar features in the NMR spectra suggest that this mechanism could describe degradation due to both sonication and ageing. Furthermore, the presence of these features in the NMR spectra of all samples suggests that any degradation product is also present, at lower concentration, in the as-received NMP. Notably, the alkenyl and methyl protons associated with the previously-proposed mechanism of enamine formation and polymerization, are present and show downfield shifts relative to the as-received NMP. This is consistent with the downfield shifting of peaks expected due to deshielding by a nearby π-system, which could be a conjugated species which gives rise to the absorption and PL in both aged and sonicated NMP.

To determine whether the emergent absorption and PL are likely to be due to the pristine NMP or from a modified species, time-dependent density functional theory calculations were performed [177]. The unmodified NMP molecule was found to have optical transitions in the UV range of the spectrum only, with the primary

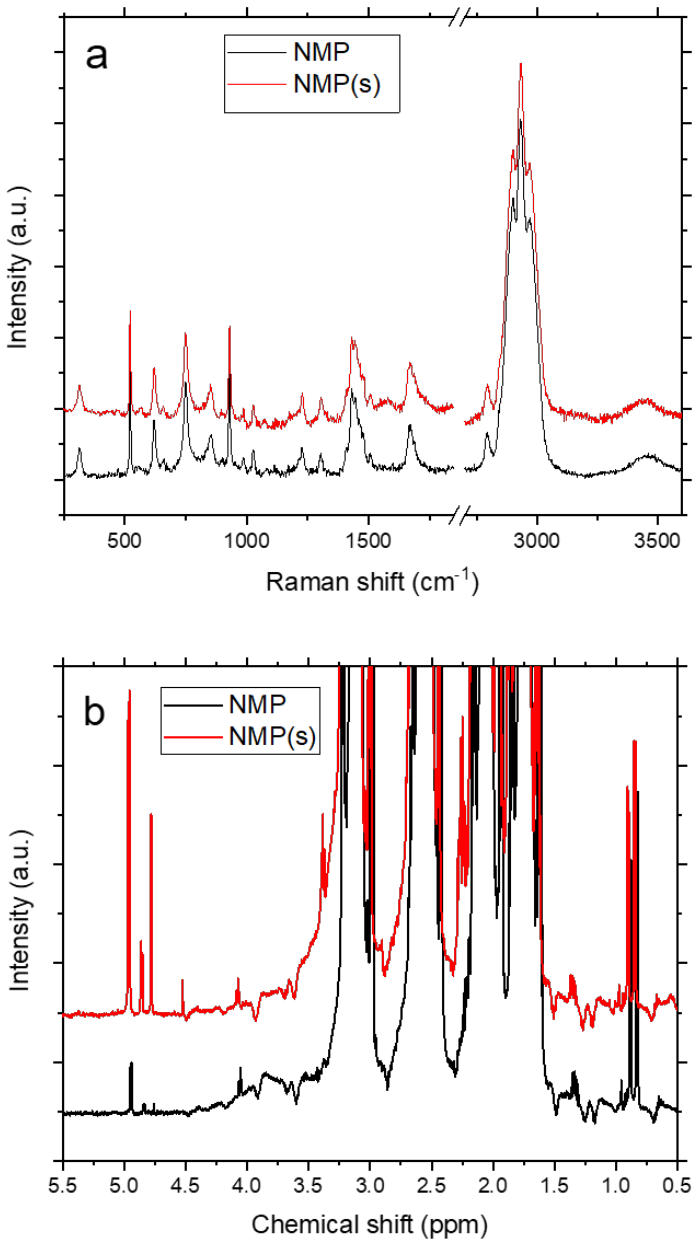

Figure 4.2: (a) Raman and (b) ^{1}H NMR spectra of NMP and NMP(s), with no discernible changes in the Raman modes but new features emerging in the NMR, most notably alkenyl protons at chemical shift of 5 ppm.

absorption and emission features around 180 and 250 nm respectively, which strongly suggests that emerging properties in the visible range are due to a modified species. Using the previously-proposed enamine species as a starting point for degradation and polymerisation, the primary optical absorption redshifts by more than 40 nm. In addition, calculations show the emergence of a strong PL transition in the visible at 470 nm. While the modified species is likely to be more complex than the NMP derivative used, such calculations demonstrate that simple structural modifications can result in significant shifts and emergent transitions in the optical spectra of NMP.

4.3 Optical spectroscopy

In order to ascertain the extent of the emission from the new species, PL spectroscopy was performed to obtain photoluminescence excitation (PLE) maps containing all excitation and emission spectra (Figure 4.3). These PLE maps indicate that NMP exhibits broad photoluminescence with peak emission around 400 nm under excitation at 325 nm. In addition, the spectroscopic changes after sonochemical degradation are illustrated by the changes in the intensity of the PL. For any given excitation wavelength, the peak PL intensity increases with the age of the NMP, resulting in the increasing brightness shown in the photographs in Figure 4.1. The as-received NMP exhibits only very weak photoluminescence, with Raman features observed as prominently as the PL peaks. For NMP(s), the PL intensity is increased by an order of magnitude with appreciable emission across the whole visible spectrum.

The PL spectra for peak emission (λ_{em} = 400 nm, λ_{exc} = 325 nm) of NMP and NMP(s) are shown in Figure 4.4 and can be fitted as the sum of two components, Gaussian in energy, at approximately 380 nm and 440 nm. Instrument-broadened Raman scattering of the excitation source (identified as the feature at ∼2900 cm^{-1} in Figure 4.2) is present in the PL spectra at ∼360 nm (Figure 4.4(a)). The relevant data ranges were neglected from the curve fitting. These two PL components correspond to two emission species in the samples. When excited at lower energy than one or both

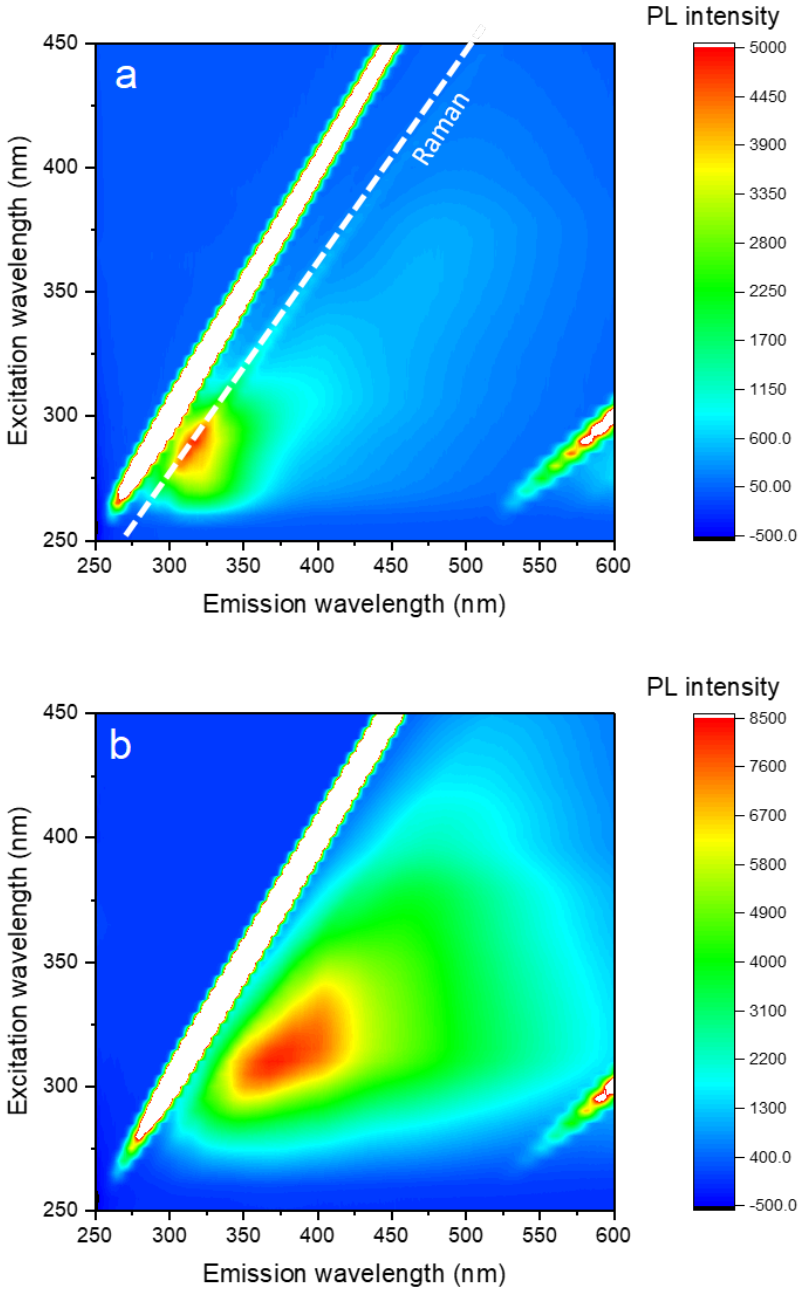

Figure 4.3: Photoluminescence excitation maps of (a) NMP and (b) NMP(s) showing significantly enhanced intensity and redshift of emission. White space corresponds to the excitation source (samples are not sufficiently absorbing at all wavelengths to quench this feature), the other linear feature at around 550 nm is the second order diffraction of the excitation source and the dashed line indicates feature associated with C-H stretch Raman at 2900 cm^{-1}.

of the species, as is common for photoluminescence measurements of 2D materials, the breadth of the features results in a redshifted contribution of that feature to the PL spectrum. This is illustrated by the significant PL intensity shown in the PLE maps for long wavelength excitation of NMP(s). The emission is dominated by the feature at 440 nm, which shows an apparent redshift with increasing excitation wavelength which, in dispersions containing nanosheets, result in secondary excitation of the dispersed nanomaterial.

The PL excitation spectrum in Figure 4.4(c) shows the wavelengths at which excitation contributes to the peak emission at 400 nm. In the absence of any other factors, it would be expected that this excitation spectrum shows features which correspond to absorption features in the extinction spectrum. While the extinction does increase with decreasing wavelength close the excitation spectrum maximum, it is not monotonic which suggests some other mechanism of extinction. This may be scattering contributions, particularly prevalent at shorter wavelength, or absorption caused by excitation between non-radiative states. In addition, the broad nature of the PL is further illustrated by PL spectra for longer wavelength excitation shown in Figure 4.4(d) and (e) where both NMP and NMP(s) exhibit non-negligible PL with similar lineshape extending across the visible spectrum under excitation at 405 nm (laser wavelength used for inset of Figure 4.1) and 450 nm (practically-relevant wavelength for excitation of photoluminescent nanomaterials).

Time-resolved photoluminescence spectroscopy was performed to provide characterisation of the photoluminescence lifetimes of the species in the NMP samples. Figure 4.5 show time-resolved photoluminescence measurements with excitation wavelength of 336 nm at an emission wavelength of 400 nm, chosen to be as comparable as possible with the steady-state spectra shown above. It is evident that the total photoluminescence lifetime is significantly increased for NMP(s) compared with NMP. These time-correlated emission measurements can be fitted as the sum of exponential components, as shown in Figure 4.5, where both samples were found to have a short-lived species with lifetime around 1 ns and a longer-lived species with

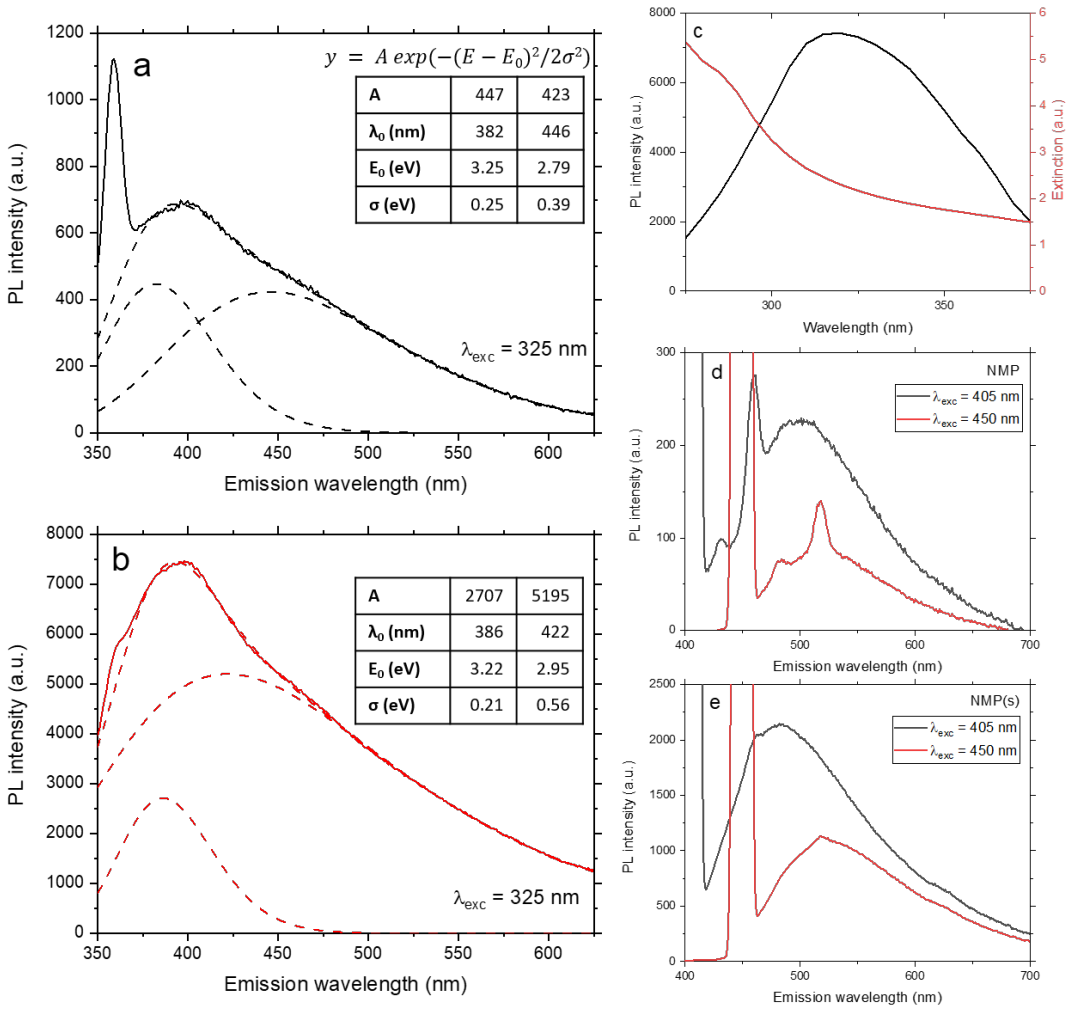

Figure 4.4: Photoluminescence spectra of (a) NMP and (b) NMP(s) with two-component fitting at peak emission wavelength. (c) Comparison of extinction and PL excitation spectrum, indicating absorption resulting in emission is centred at 325 nm and additional contributions to extinction may be scattering effects. (d) PL spectra for NMP and (e) NMP(s) for longer wavelength excitation, illustrating similar strong broad emission extending across the visible spectrum.

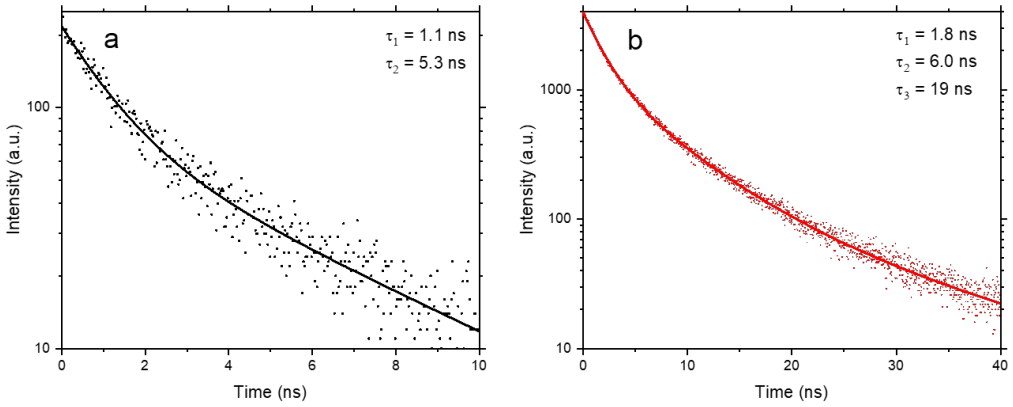

Figure 4.5: Time-resolved photoluminescence of NMP and NMP(s) showing significantly increased lifetime and additional component in fitting.

lifetime around 5 ns. In addition, NMP(s) was found to have a third component with significantly greater lifetime of 19 ns. The relative abundances of the two shorter-lived species indicate that they likely correspond to the two components from the steady-state data, while the longer-lived species in NMP(s) is a much smaller contribution which was not identified in the steady-state fitting. In addition, the increase in the individual component lifetimes could suggest that the PL observed in as-received NMP is not due to the pristine NMP but due to the onset of ambient degradation. Greater delocalisation of the electron-hole pair in the excited state leads to the observed increase in the excited state lifetime. As such, the overall increase in lifetime with degradation is consistent with the formation of a larger, possibly polymerised, species.

It has been shown that sonication of NMP results in modification of both the chemical composition and the optical properties of the solvent. Sonochemical degradation has previously been shown to influence the behavior of NMP as a solvent for exfoliation and dispersion of nanomaterials [171, 172]. The considerable changes observed with the relatively short sonication used to produce NMP(s) highlights the potential for the solvent degradation under typical exfoliation processes for 2D materials. In order to understand the influence of sonochemical degradation on liquid phase exfoliation of 2D materials, samples of graphene and MoS_2 were exfoliated by

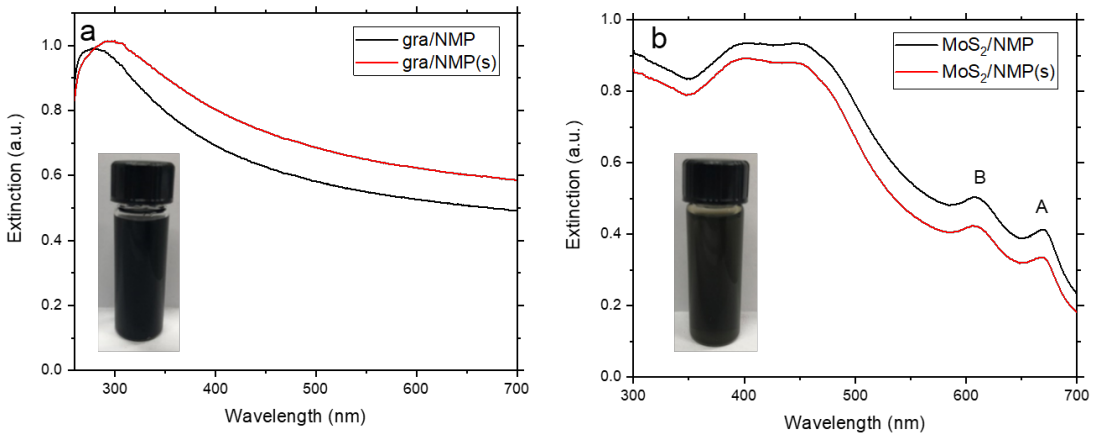

Figure 4.6: UV-visible extinction spectra of NMP-exfoliated graphene and MoS_2, with A- and B-excitonic positions labelled, with some variation in concentration for the pre-sonicated solvent.

sonication into as-received NMP and pre-sonicated NMP(s). UV-visible absorption spectra for the dispersions are shown in Figure 4.6, which show opposing influences on exfoliation into pre-sonicated NMP(s). As previously demonstrated for carbon nanotubes [171], the concentration of graphene dispersions is increased for exfoliation into NMP(s), as illustrated by the 10% increase in extinction. It is possible that this is due to solvation of the graphene nanosheets by a polymeric degradation product, similar to the polymer wrapping suggested for carbon nanotubes. While covalent modification of the nanomaterial has also been suggested as a potential mechanism [171], given that liquid phase exfoliation in NMP has been shown to produce defect-free graphene [14], it is anticipated that polymer wrapping is the more likely mechanism. By contrast, the concentration of MoS_2 dispersions is decreased for exfoliation into NMP(s), suggesting that the production of degradation products and their interaction with the 2D materials may be sensitive to the chemical composition of the system. While the properties of these liquid-exfoliated dispersions are also likely to be influenced by the process itself, the differences observed demonstrate the sensitivity of the 2D materials to degradation of the solvent which will occur dynamically during exfoliation and is therefore inevitable for sonication-based exfoliation processes.

In addition, the influence of NMP degradation on the optical properties of the solvent present previously-unacknowledged challenges for spectroscopy of dispersions and solutions in NMP. Any dispersion produced by ultrasonication will be subject to degradation of the NMP, which further increases scattering in the solvent and the dispersion [171, 172]. As such, it is not appropriate to use an untreated NMP sample as a reference for absorption spectroscopy as this will be chemically different from the sonicated NMP in the dispersion. However, if the reference sample is also sonicated, the ultrasonic cavitation field and thereby the sonochemical processes will differ significantly between the dispersion and the NMP reference sample. Importantly, this indicates that it is not possible to produce a reference sample of NMP for optical spectroscopy which is identical to the NMP in the nanomaterial dispersion. As such, the reference samples used for the spectra in Figure 4.6 were the starting solvent NMP and NMP(s) respectively, which may no longer be representative of the solvent in the dispersion and the spectra therefore represent an upper bound on the absorption due to the 2D materials. This is clearly problematic for extinction-based measurements of concentration, size and thickness [115] and highlights the need for alternative solvents and exfoliation processes.

Finally, the most significant influence of NMP degradation is in its use as a solvent for photoluminescence spectroscopy of nanomaterials, despite the solvent itself exhibiting strong and broad photoluminescence. Such nanomaterials include conjugated polymers [178], carbon nanotubes [179], transition metal dichalcogenides [180, 181] and black phosphorus [170, 96]. For most of these materials, the photoluminescence is not in the same wavelength range as the NMP but the excitation wavelengths used could result in broad background luminescence from the solvent, although there is likely to be some quenching by the nanomaterial. This presents the possibility of the NMP emitting into the absorption band of the nanomaterial and providing an undesired longer wavelength excitation. For example, excitation of a dispersion of MoS_2 or black phosphorus in NMP at 450 nm will result in PL emission from the NMP in the range 500–600 nm and further excitation of the dis-

persed nanosheets, potentially resulting in additional spectral features or influencing spectroscopic measurements of such materials. This is particularly problematic for quantitative spectroscopic measurements such as that of monolayer fraction from PL and Raman spectroscopy [57], which could be invalidated by secondary excitation of the MoS_2 by PL emission from the NMP.

To illustrate the influence of NMP degradation, the PL spectrum for MoS_2 exfoliated into NMP for excitation at 450 nm is shown in Figure 4.7. MoS_2 dispersions typically show weak PL since emission is only from monolayer nanosheets and self-absorbance reduces the outgoing signal. As such, the PL spectrum shows features at low intensity corresponding to A and B exciton PL at ∼680 nm and ∼625 nm respectively. The intense broad feature at ∼530 nm is not due to the MoS_2 but is instead due to the NMP, observed at longer wavelength under excitation at 450 nm. This feature is likely to have been incorrectly attributed to MoS_2 in previous studies [181]. To confirm this, the MoS_2 dispersion was centrifuged at high speed to sediment the nanosheets out of the dispersion. The supernatant NMP was then discarded and the material was redispersed into fresh aqueous sodium cholate solution in a manner similar to liquid cascade centrifugation [57]. Figure 4.7(a) shows the PL spectrum for the dispersion of MoS_2 in surfactant and water following solvent transfer. The broad background due to the feature at ∼530 nm is no longer present, confirming that it is indeed PL from the degraded NMP, and the spectrum shows only the PL from the MoS_2, albeit dominated by the B exciton due to self-absorbance by multilayers in the range of the A exciton. Together these spectra demonstrate the influence of NMP degradation on the PL spectra of liquid-exfoliated 2D materials and present a potential route, through sedimentation and redispersion, to transfer nanomaterials into fresh or different solvents to minimise the influence of solvent degradation on spectroscopy of 2D materials.

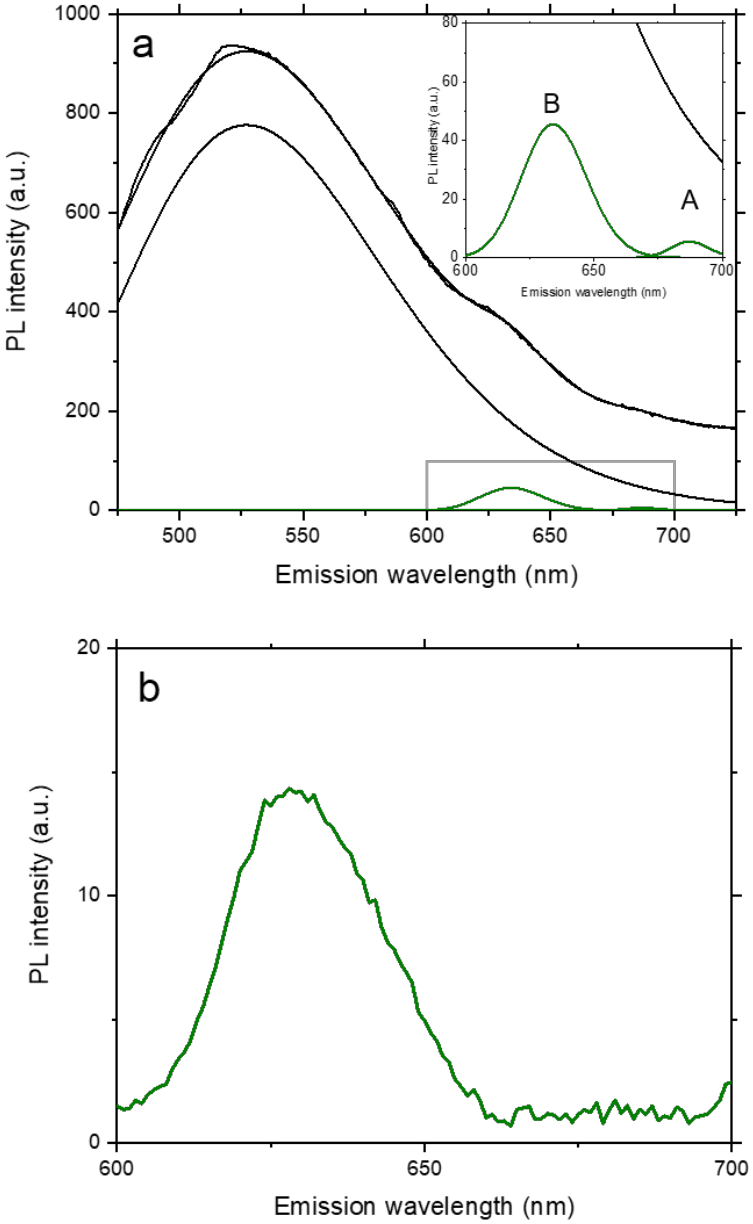

Figure 4.7: Photoluminescence spetra of NMP-exfoliated MoS_2 before (a), showing A- and B-excitionic peaks, and after (b) solvent transfer.

4.4 Conclusions

In conclusion, NMP, the most widely used solvent for 2D materials, has been shown to present significant challenges for liquid phase exfoliation due to its susceptibility to sonochemical degradation. It has been shown that NMP is even susceptible to such degradation with ageing under ambient conditions. Both ambient and sonochemical degradation result in chemically-similar products which give rise to strong visible photoluminescence of the NMP. In addition, this solvent degradation has been shown to influence the performance of NMP as a solvent for liquid phase exfoliation of 2D materials and perhaps even complicate the understanding of solubility parameters for solvent selection. Measurements of such dispersions are complicated by the increasing optical absorbance with solvent degradation and the nature of ultrasonic processing suggests that it is not possible to produce a sample of NMP as a reference sample for extinction spectroscopy, which is identical to the solvent in the dispersion. Furthermore, the emergence of photoluminescence of the degraded NMP influences spectroscopic measurements of photoluminescent materials in NMP, such as transitional metal dichalcogenides, with the PL spectrum of MoS_2 in NMP shown to be dominated by the degraded solvent. These observations indicate that the use of NMP requires careful consideration for liquid phase exfoliation and optical spectroscopy of 2D materials.

Chapter 5

Size selection of liquid-exfoliated nanosheets

Here, a size selection model for liquid-exfoliated two-dimensional nanosheets is presented. The ability to consistently select exfoliated nanosheets with desired properties is important for development of applications in all areas. The model presented facilitates determination of centrifugation parameters for production of dispersions with controlled size and thickness for different materials, solvents and exfoliation processes. Importantly, after accounting for the influence of viscosity on exfoliation, comparisons of different solvents are shown to be well described by the surface tension and Hansen parameter matching. This suggests that previous analyses may have overestimated the relative performance of more viscous solvents. This understanding can be extended to develop a model based on the force balance of nanosheets falling under viscous drag during centrifugation. By considering the microscopic aspect ratio relationships, this model can be both calibrated for size selection of nanosheets and compare the exfoliation processes themselves.

Liquid phase exfoliation has been demonstrated to be a versatile, scalable and cost-effective technique for the production of few-layer two-dimensional (2D) nanosheets for a wide range of applications [15, 182, 183, 129, 96, 184]. Although surfactants in aqueous solution have been shown to yield high-quality dispersions of few-layer

nanosheets at reasonable concentrations owing to stabilisation by the amphiphilic surfactant molecules, their presence can be undesirable for some applications [103]. Moreover, in certain cases it would be preferable to produce high-quality dispersions in organic solvents [100, 11, 151]. As a result, there has been extensive work to identify "good" solvents based on the chemical physics of their interactions with the nanosheets through surface tension and Hansen solubility parameters [15, 113, 14].

The most commonly used and well-studied method for liquid phase exfoliation of 2D materials is probe ultrasonication, where high frequency ultrasound is applied to a high mass concentration dispersion of bulk layered material in liquid [15, 14]. The sonication process both exfoliates and cuts the layered materials to yield a dispersion of particles with a wide distribution of size and thickness; from unexfoliated crystallites to monolayer nanosheets. After sonication, dispersions are typically subjected to centrifugation-based size selection where increased relative centrifugal forces result in accelerated and preferential sedimentation of the larger particles, leaving the few-layer nanosheets dispersed in the supernatant.

In addition to the considerations of surface tension and Hansen parameters, the physical properties of the solvents typically employed will influence the exfoliation, size selection and stability of the liquid-exfoliated nanosheets due to their effect on buoyancy, viscous drag, etc. An understanding of the influence of various processing parameters (sonication time and power, relative centrifugal force, etc.) on concentration, size and thickness of the exfoliated nanosheets has been developed through an iterative approach and is well described by scaling laws to maximise yield and the degree of exfoliation [106]. However, there is little physical interpretation of this understanding (i.e. of the exponents and pre-factors of these scaling laws) to generalise the applicability to different materials and solvents. Here the influence of these factors is studied to develop exfoliation processes, which apply to different 2D materials and solvents. In particular, our results point to the role of viscosity in determining exfoliation yield during probe sonication and size selection during centrifugation. Accordingly, a model can be developed based on the force balance

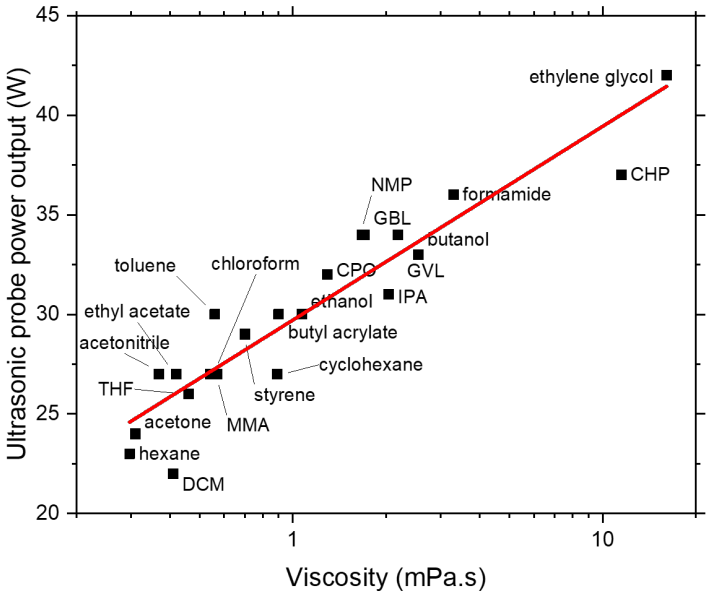

Figure 5.1: Dependence of ultrasonic probe power output on solvent viscosity, showing a logarithmic relationship.

of nanosheets falling under viscous drag during centrifugation that well describes size selection. This will allow others in the field to produce dispersions with desired properties for their chosen applications.

5.1 Viscosity effects

During sonication, a probe oscillates at a fixed ultrasonic frequency and the amplitude (as a percentage of the maximum tip displacement) can be controlled as an experimental parameter. Although this complicated process depends on many factors such as vessel size and shape [163], the absolute power delivered by the probe is determined by the resistance to oscillation and therefore is primarily related to the viscosity of the liquid being sonicated. As such, the power output and therefore total energy delivered during ultrasonication-based exfoliation cannot be independently controlled, preventing a direct comparison of the exfoliation processes in solvents with different viscosities.

Figure 5.1 shows the ultrasonic power output for a range of organic solvents as a

function of their viscosity. The power output shows a clear logarithmic dependence, which results in low viscosity solvents such as acetone being subjected to only 60% of the power of high-viscosity solvents such as cyclopentanone (CPO). Notably, many of the good solvents identified for liquid phase exfoliation have viscosity >1 mPas [15, 14]. While high viscosity is typically correlated with high surface tension and Hansen parameters through the cohesive energy density, it is possible that previous analyses, which have neglected the effect of viscosity, may have overestimated the relative performance of more viscous solvents. It is worth noting however that the viscosity-dependent power delivered by the tip is not all delivered to the dispersed nanomaterial or even the solvent; differences in the heat capacities of different solvents and power loss through the walls of the vial will influence the power available for exfoliation.

In addition to its influence on the ultrasonic power output, the viscosity of the liquid will influence centrifugation-based size selection, since viscous drag forces oppose the sedimentation of dispersed particles. Nanosheets in higher viscosity liquids will experience greater viscous drag than nanosheets of the same size and mass in a lower viscosity liquid. As such, they sediment more slowly leaving a higher concentration of larger and thicker nanosheets dispersed in the supernatant than for lower viscosity liquids. This leads to higher post-centrifugation mass concentrations in these higher viscosity liquids when centrifuged under the same conditions as lower viscosity dispersions, due to the inclusion of these larger nanosheets.

In order to illustrate the significance of the twofold contribution of viscosity to exfoliation and size selection yield, analysis has been performed using data from O'Neill et al. [101] on the concentrations of graphene in both 'good' and 'bad' solvents with both low and high viscosity where single centrifugation steps at different speeds have been used to size select the nanosheets in the supernatant. To show the influence of viscosity, acetone and isopropanol (IPA) are considered as two so-called poorer solvents. Although both solvents have a large mismatch in relative surface tension and Hansen parameters compared to graphene, IPA has a

six-times-greater viscosity η than acetone, ($\eta_{acetone}$ = 0.31 mPa.s, η_{IPA}= 2.04 mPa.s [185]). For comparison, cyclohexanone (CHO), *N*-methyl-2-pyrrolidone (NMP) and dimethylformamide (DMF) have been included as three so-called good solvents which are similarly well matched to graphene in surface tension and Hansen parameters but also with a range of different viscosities (η_{CHO}= 2.02 mPa.s, η_{NMP}= 1.67 mPa.s, η_{DMF}= 0.92 mPa.s [185]).

Figure 5.2 shows the concentration of graphene in the different solvents as a function of the relative *g*-force used for the centrifugation-based size selection. The differences in concentration between the good solvents and the poorer solvents can be attributed to the yield of few-layer nanosheets during the ultrasonic exfoliation process which is determined by the surface tension and Hansen parameter matching [101], although NMP is also known to be susceptible to sonochemical degradation which may influence exfoliation [177, 172], as discussed in Chapter 4. As the relative *g*-force is increased, larger and thicker nanosheets are preferentially sedimented, leaving smaller and thinner populations of nanosheets dispersed, as shown by the decreasing concentration, which is well described by a series of near-parallel power laws for all solvents.

Interestingly, at low relative *g*-force centrifugation, DMF has the highest relative graphene concentration, despite its lower viscosity, while the highest viscosity solvent, CHO, has the lowest concentration with NMP being intermediate. This suggests that initially, the detailed performance of good solvents is dictated by the chemical physics of surface tension and Hansen parameters more so than the fluid physics of viscosity. Conversely, as the centrifugation process proceeds to higher relative *g*-force the already-thinner population of nanosheets in DMF is subjected to further sedimentation which decreases the concentration below both CHO and NMP, where higher viscosity results in retention of larger and thicker nanosheets and therefore higher concentration.

Clearly, a viscosity-based normalisation of the centrifugation parameters is required in order to quantitatively compare solvents and more importantly to allow

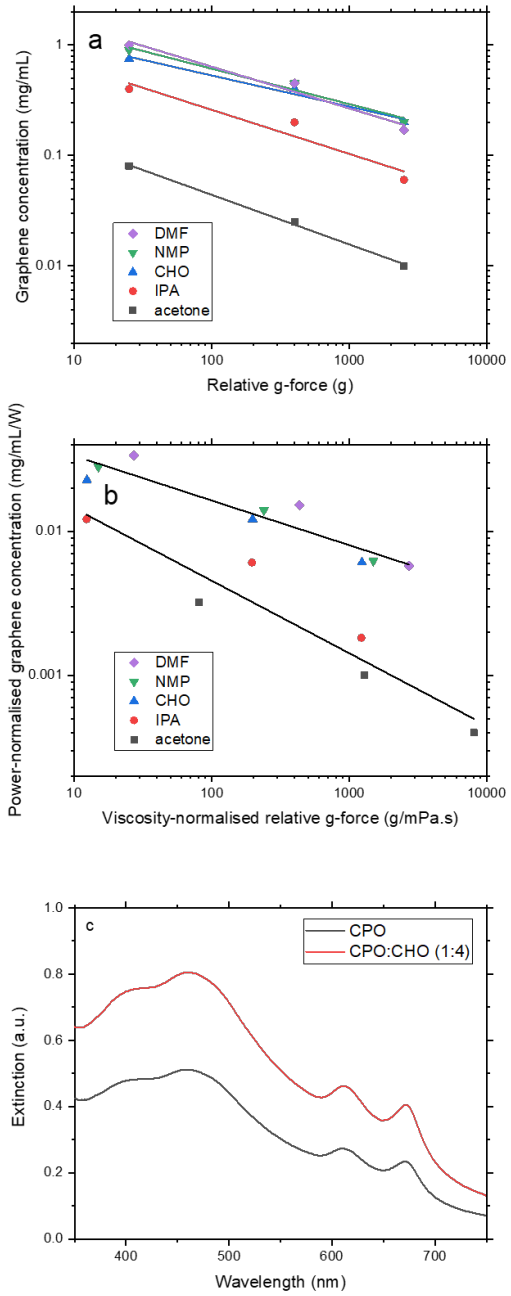

Figure 5.2: (a) Graphene concentration in a range of "good" and "bad" solvents as a function of the relative g-force applied during centrifugation-based size selection, adapted from [101]. (b) Graphene concentration from (a) normalised to ultrasonic power output, as a function of viscosity-normalised relative g-force, to account for the influence of viscosity on both exfoliation and size selection. (c) UV-visible extinction spectra for MoS_2/CPO dispersion diluted into CPO and CHO before further centrifugation to illustrate the influence of viscosity.

consistent size selection of few-layer nanosheets with controlled size and thickness. As concentration increases approximately linearly with the energy-per-unit-volume applied during exfoliation [106], the concentration dependence on relative g-force can be normalised to the ultrasonic power delivered as shown in Figure 5.2. The sedimentation rate of a given size will be proportional to the relative g-force R (contributing to the weight) and inversely proportional to η contributing to the viscous drag. This additional normalisation accounts for the variation in viscous drag experienced by nanosheets of the same size and mass under the same centrifugation conditions in solvents of different viscosity. As such, R/η allows for comparison of equivalent centrifugation conditions.

With this normalisation, CHO, NMP and DMF (and other "good" solvents) can be compared when subjected to equivalent centrifugation, which indicates that DMF shows higher concentration relative to its viscosity-normalised centrifugation conditions than NMP and CHO. This suggests that for this exfoliation and size selection process, DMF is genuinely the best solvent in terms of concentration of the graphene relative to the centrifugation conditions, i.e. the DMF dispersion contains nanosheets which are thinner and/or smaller and at higher concentration than in NMP and CHO.

For the poorer solvents, acetone and IPA, the viscosity normalisation results in an even more significant shift where the 2500 g centrifugation in IPA is shown to be nearly equivalent to the 400 g centrifugation in acetone (roughly equal to the ratio of their viscosities). Under these viscosity normalised centrifugation conditions, the concentrations of graphene in acetone and IPA are comparable and the data could be considered to converge on a single power law for poorer solvents, where the surface tension and Hansen parameter mismatch makes these viscosity effects markedly more pronounced. Indeed, it is even possible that if physical properties of the solvent could be suitably accounted for (by controlling power delivered, correcting centrifugation for viscosity, etc.), acetone and IPA could be equally good (or bad) solvents for the exfoliation of few-layer graphene and other 2D materials.

To further illustrate the effect of viscosity on sedimentation, molybdenum disulfide (MoS_2) was exfoliated in cyclopentanone (CPO) by probe ultrasonication, with a centrifugation step applied to remove unexfoliated material. CPO has surface tension and Hansen parameters almost equivalent to the six-membered-ring analogue CHO [112], but has significantly lower viscosity (η_{CPO}= 1.23 mPa.s, η_{CHO}= 2.02 mPa.s [185]). To isolate the influence of this viscosity difference for these otherwise very similar solvents, the MoS_2/CPO dispersion was diluted by a factor of 5 into both CPO and CHO and subjected to further centrifugation. The similarities between CPO and CHO make it possible to have an identical population of nanosheets in solvents of different viscosities without requiring changes to the exfoliation and size selection procedures.

Figure 5.2 shows the UV-visible extinction spectra of the CPO- and CHO-diluted dispersions after the second centrifugation step. The concentration of the CHO-diluted sample, measured from the minimum at ∼350 nm is around 50% higher than for the CPO-diluted sample, highlighting the effect of the increased viscosity in reducing sedimentation rate and leaving a greater mass of nanosheets dispersed than in the CPO sample. In addition, there is a slight redshift of the A-exciton for the CHO-diluted sample suggesting higher average layer number. Moreover, using the length metric calculation outlined by Backes et al. [56] the nanosheets are on average 5% larger. It is evident that the slower sedimentation rate allows larger particles to remain suspended in the high-viscosity system, where they would be removed from a dispersion with lower viscosity. This highlights the importance of accounting for viscosity (at least in centrifugation-based size selection) to ensure the size, thickness and concentration of the 2D nanosheets being selected is consistent between different solvents.

5.2 Modelling centrifugation

With this empirical understanding of the influence of viscosity and concentration on centrifugation, it would be desirable to develop a quantitative model for size

selection of few-layer nanosheets of a given size or thickness in arbitrary solvents. This approach facilitates consistent selection irrespective of the efficiency of the exfoliation process itself. By extending the arguments about viscous drag and sedimentation rate, it is possible to develop a simple metric for the centrifugation parameters required to sediment nanosheets based on their physical properties and those of the solvent.

Firstly, it is necessary to consider the force balance on nanosheets while falling under their weight, buoyancy and viscous drag due to the liquid, as shown in Figure 5.3(a), to determine their terminal velocity and therefore sedimentation time for a given height of centrifuge tube. The net force due to weight F_g and buoyancy F_b for a nanosheet can be related to the density of the material ρ_{2D} and that of the liquid ρ_l, the volume of the nanosheet V, relative g-force R and acceleration due to gravity g by

$$F_g - F_b = (\rho_{2D} - \rho_l) V R g \tag{5.1}$$

The effective drag radius of the nanosheets is estimated to be proportional to the geometric mean of the length, width and thickness, i.e. the cube root of the volume V with some constant α, accounting for the non-cubic nature of the nanosheets, such that the drag force can be related to the viscosity of the liquid η, the drag radius $\alpha V^{1/3}$ and the velocity v by

$$F_d = 6\pi\eta\alpha V^{1/3} v \tag{5.2}$$

The above equations are equal assuming terminal velocity and this velocity can be expressed as $v = h/T$, where T is the time taken to sediment through a centrifuge tube of height h, such that

$$(\rho_{2D} - \rho_l) V R g = 6\pi\eta\alpha V^{1/3} h/T \tag{5.3}$$

This can be expressed in terms of the g-time product (g-force Rg and time T in

seconds) as

$$RgT = \frac{6\pi\eta h}{(\rho_{2D} - \rho_l)\alpha V^{2/3}} \tag{5.4}$$

In order for RT to yield a number of g-minutes (divide by 60 seconds per minute), this can be further simplified as

$$RT = \frac{\pi\eta h}{10(\rho_{2D} - \rho_l)\alpha V^{2/3}} \tag{5.5}$$

Effectively, the model describes the centrifugal processing required to draw sheets of volume V from the top of a centrifuge tube to the bottom. Interestingly, it suggests that there is a direct equivalence between relative centrifugal force and time. For instance, this suggests that 1 minute at 15000 g will result in equivalent sedimentation as 1 hour at 250 g or even 15000 minutes under gravity, provided the effects of diffusion-driven reaggregation are negligible.

In order to test this model, dispersions of MoS_2, tungsten disulfide (WS_2), graphene and boron nitride (BN) were prepared in aqueous sodium cholate solution by ultrasonic exfoliation and liquid cascade centrifugation [57]. In this process, the samples are produced by sedimentation and redispersion of the desired nanosheets which results in narrower size distributions compared with a single centrifugation step. The process is repeated under increasing centrifugation conditions to yield a series of samples with nanosheets of decreasing size and thickness. Specifically, in each step, the centrifugal acceleration was increased, but the time held at 2 hours. Identical vial geometries were used across the four data sets. The size-selected samples were characterised by statistical atomic force microscopy. The longest dimension (L), dimension perpendicular to this (width, W) and thickness were measured on 200-250 individual nanosheets. The apparent thickness was converted to layer number by the reported step height analysis of the material [106, 56, 119]. From such a statistical analysis, mean length $\langle \mathrm{L} \rangle$, width $\langle \mathrm{W} \rangle$ and layer number $\langle \mathrm{N} \rangle$ for all samples was calculated and analysed as a function of their centrifugation g-time product.

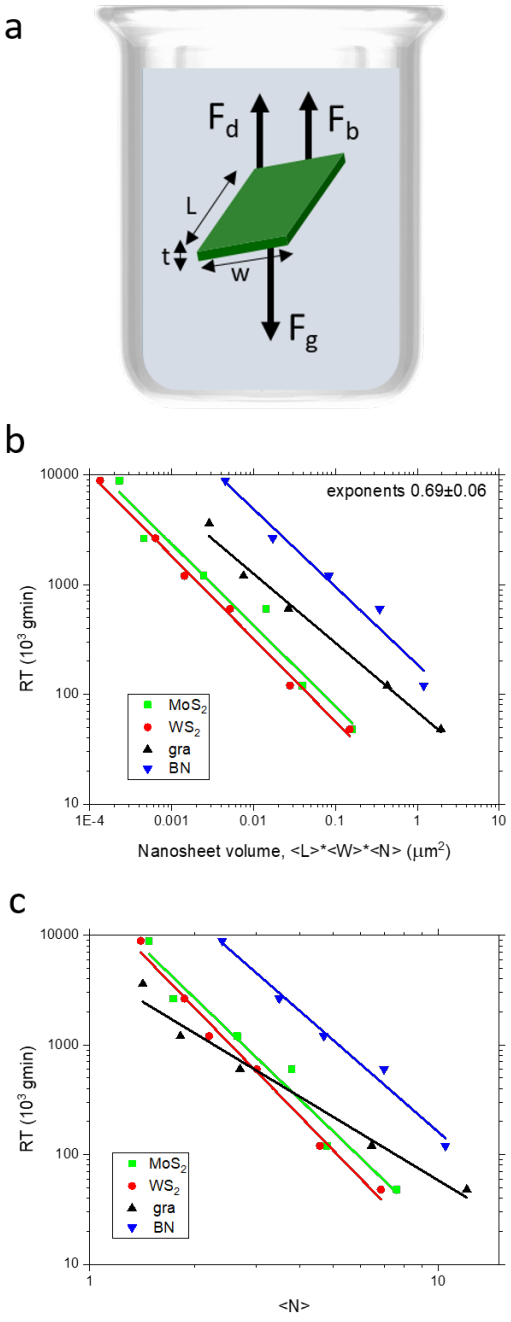

Figure 5.3: (a) Schematic showing force balance on a nanosheet falling under centrifuge-induced g-force, buoyancy and viscous drag. (b) Centrifugation g-time product as a function of nanosheet volume, measured from AFM, for size-selected dispersions of MoS_2, WS_2, graphene and BN, with power law fitting and exponents of 0.69±0.06. (c) Centrifugation g-time product as a function of average layer number for size-selected dispersions with power law fitting showing variation due to aspect ratio effects.

These statistics can be used to calculate a mean nanosheet volume for each size-selected sample V=⟨L⟩⟨W⟩⟨N⟩ which facilitates fitting of the data according to Equation 1. This data with the appropriate fitting is shown in Figure 5.3; in all cases, the g-time product also exhibits power law scaling with the volume with all exponents in the range 0.69 ± 0.06, indicating that the relationship RT ∼ $V^{-2/3}$ well describes the size selection process.

While models similar to Equation 5.5 have been proposed [109] and verified [108] previously, little attention has been devoted to understanding the influence of aspect ratio on centrifugation. In practise, the volume of a nanosheet population is difficult to relate directly to the individual dimensions of interest; in particular the average layer number ⟨N⟩, which is most indicative of the degree of exfoliation. In contrast to the volume scaling, the power-law exponents for the g-time product variation with ⟨N⟩ vary significantly between different materials, as shown in Figure 5.3, presumably due to material-specific variance in the basal plane area. In order to better understand this variability between scaling laws, it would be desirable to account for the various aspect ratio relationships that contribute to the volume. The microscopic power law relationships between ⟨L⟩ and ⟨W⟩ and ⟨N⟩ are shown in Figure 5.4. The pre-factors and exponents of these power laws relate to the length and width of the nanosheets at any given thickness with graphene and BN exhibiting larger pre-factors and smaller exponents than MoS_2 and WS_2, suggesting "better" exfoliation to larger nanosheets at lower layer number.

These well-defined aspect ratio relationships facilitate parameterisation of the effective volume of a nanosheet in terms of ⟨N⟩ with pre-factors and exponents which are characteristic of the exfoliation process, $\langle V\rangle \equiv \langle L\rangle\langle W\rangle\langle N\rangle \sim \langle N\rangle^a\langle N\rangle^b\langle N\rangle = \langle N\rangle^{a+b+1}$. Accordingly, by also parameterising the effective drag radius as $r \sim r_0\langle N\rangle^c$, the centrifugation g-time product for size selection can be expressed in terms of the nanosheet thickness $\langle N\rangle$;

$$RT = \frac{\pi\eta h}{10(\rho_{2D} - \rho_l)k^2\langle N\rangle^n} \tag{5.6}$$

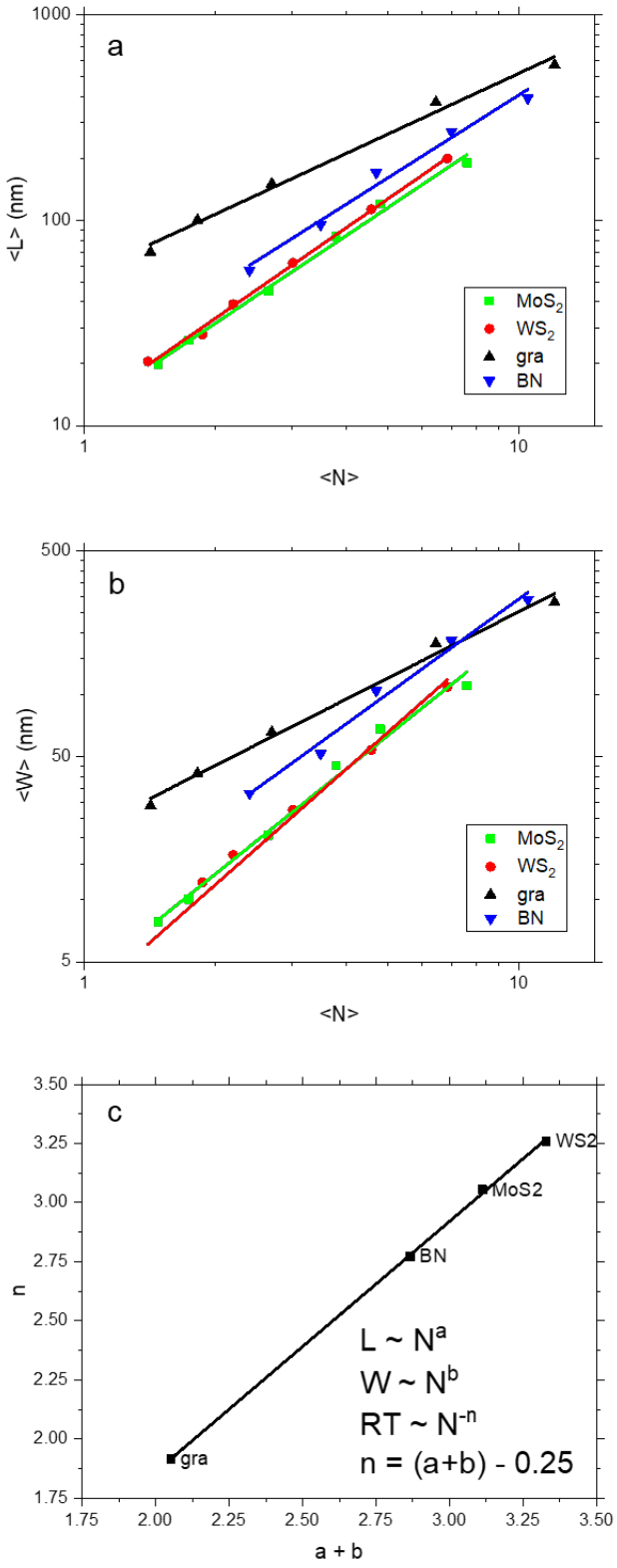

Figure 5.4: (a) Length and (b) width of size-selected dispersions as a function of average layer number to account for variability in g-time-$\langle N \rangle$ scaling in Figure 5.3. (c) Scaling exponent for g-time against the sum of scaling exponents for length and width for different materials, indicating variability in Figure 5.3 is fully accounted for by aspect ratio relationships.

where k is a "shape factor" related to the product of the prefactors of the aspect ratio scalings of the nanosheets which appears as k^2 since the term derived from $V^{2/3}$ must have units of area, meaning that k is correlated with the monolayer size for a given population of nanosheets and the exponent n=a+b+1-c. This approach gives justification to the selection of centrifugation parameters to sediment a given size of nanosheets from a dispersion and potentially allows for the standardisation of size selection to ensure few-layer dispersions.

Figure 5.4 shows that the relationship between RT and ⟨N⟩ is well described by these underlying aspect ratio relationships. The exponent n increases linearly with the sum of the length and width exponents. In addition, the intercept (-0.25) indicates that the drag radius exponent c=1.25 takes an empirical universal value for all of these materials. Given the drag radius has previously been shown to scale with volume with an exponent of 1/3, these relations can be equated to indicate that, on average, volume can be parameterised in terms of average layer number without the need to directly evaluate the aspect ratio of the nanosheets, such that $V \sim N^{15/4}$. This can be used to determine an average and idealised value for the exponent n of 2.5, since $RT \sim V^{-2/3} \sim N^{-5/2}$.

The idealised value of the exponent n quoted above, as an average of the data in Figure 5.3 for populations of well-exfoliated nanosheets, represents the ideal scaling for broad initial distributions of ⟨N⟩. In these samples there is sufficient content of few-layer nanosheets to allow progressively lower average layer number to be achieved through successive centrifugation steps, resulting in the expected scaling as observed in previous studies [57, 119]. Deviations from this exponent can be attributed to variations in pre-centrifugation distribution such as in dispersions of large few-layer nanosheets wherein the average layer number will be reduced more gradually with centrifugation, since the nanosheet volume decreases more gradually with layer number.

This results in reduced exponents (n<2.5) and larger shape factors compared with the average case. By contrast, while dispersions with high-few layer content but

smaller nanosheets can be considered well exfoliated, the nanosheet volumes scale more sharply with layer number and result in increased exponents (n>2.5) and small shape factors. In addition, dispersions of comparatively poorly-exfoliated nanosheets with low few-layer content will retain higher average layer number after successive centrifugations, resulting in arbitrarily large exponents and unphysical shape factors, where the intuitive aspect ratio scalings above do not apply. As such, this approach can be used not only for size selection from dispersion but also for characterisation of the exfoliation process and degree of exfoliation achieved.

5.3 Calibrating the model

A calibration experiment can be performed to determine the shape factor and exponent for any given material and processing parameters. This involves exfoliation of the bulk material followed by liquid cascade centrifugation of the exfoliated nanosheets. The average layer number of each sample would be characterised, either by statistical atomic force microscopy (AFM) or using spectroscopic metrics [56, 119, 115], and this would be used to fit against the g-time product to determine the exponent n and shape factor k for that material and process. Given this calibration, Equation 5.6 can be applied to determine centrifugation parameters to select nanosheets of any given thickness in future experiments. Figure 5.5 shows a centrifugation cascade with the RT values selected to give the greatest possible applicability for a range of solvent viscosities, material densities, shape factors and exponents, where the average layer numbers sedimented can be characterised by spectroscopic metrics in order to perform a calibration experiment.

The UV-visible extinction spectra for dispersions of MoS_2 exfoliated in sodium cholate solution (as for the data in Figure 5.3) and size selected by liquid cascade centrifugation are shown in Figure 5.5. These exhibit a clear blueshift of the A-exciton with increasing RT, associated with decreasing average layer number. The $\langle N \rangle$ values are determined from the respective spectroscopic metrics [56, 57, 119, 115] and fitted to determine the shape factor and exponent, shown in Figure 5.5. Note that in

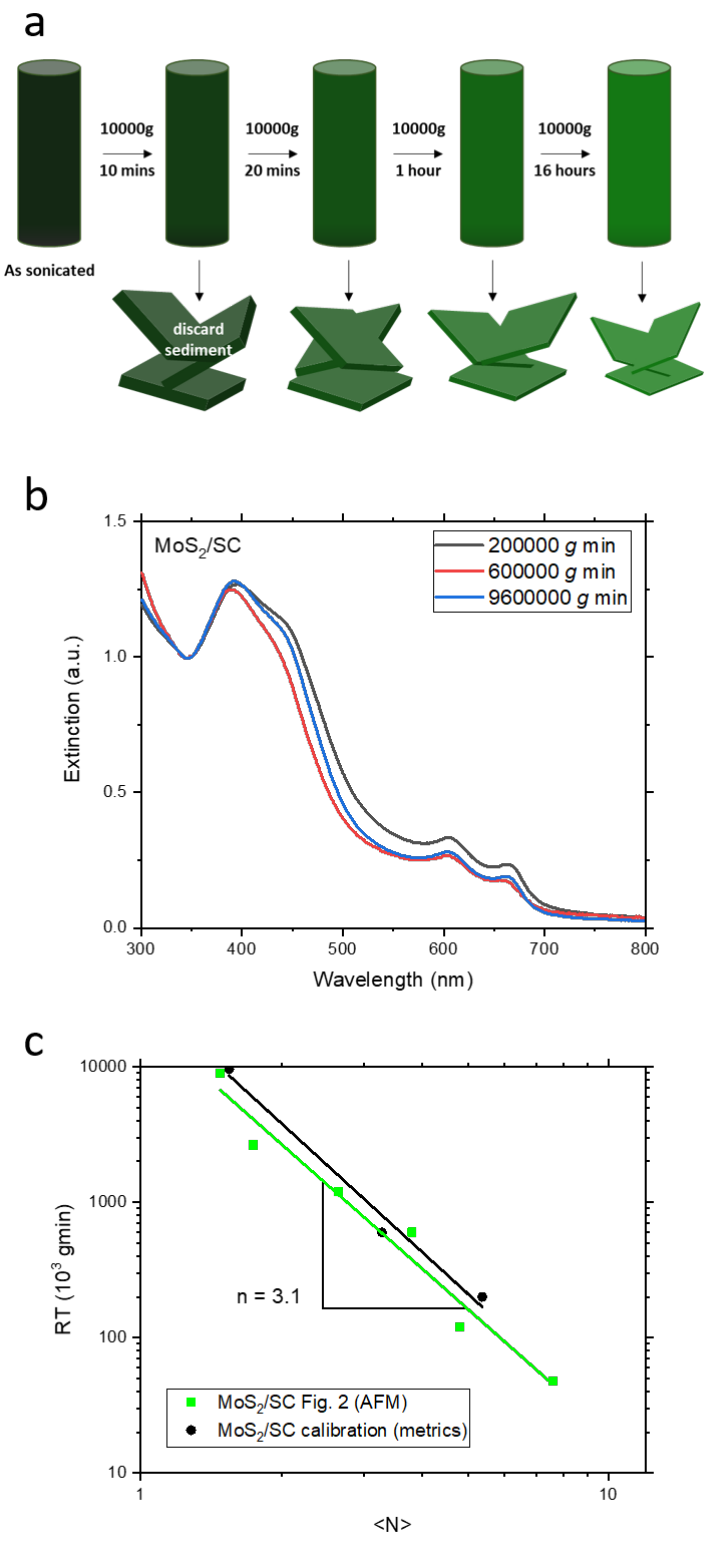

Figure 5.5: (a) Liquid cascade centrifugation calibration experiment, (b) UV-visible extinction spectra and (c) centrifugation g-time product as a function of layer number.

this experiment, the centrifugation speed was kept constant, while the time was varied in order to expedite the low g-time centrifugation steps. While a combination of varying relative g-force and time can be used to preferentially select higher or lower aspect ratio nanosheets, it is noted that using one approach or the other gives broadly similar results. Furthermore, these calibration experiments were performed with a smaller volume ultrasonic probe, smaller volumes and correspondingly shorter sonication time than for the experiments in Figure 5.3 (VCX130, 30 mL and 3 hours cf. VCX750, 80 mL and 5 hours). Nevertheless, when using the same surfactant and similar initial concentrations of MoS_2 and surfactant, there is excellent agreement in the centrifugation-size dependence indicating the robustness of the g-time equivalence and the reproducibility of nanosheet populations under comparable processing with both exponents around 3.1.

This demonstrates both the variability of exfoliated nanosheet populations when subjected to changes as subtle as the surfactant and concentration and the sensitivity of this calibration experiment to the degree of exfoliation. Furthermore, these results indicate that this method can be used not only to calibrate the size selection procedure for a given exfoliation process but also to determine the degree of exfoliation achieved by that process. This information can be used to compare exfoliation process and account for difference in subsequent experiments or to iteratively improve exfoliation processes.

The methodology and analysis presented here facilitate rapid and representative characterisation of a range of liquid exfoliated layered nanomaterials. The use of a simple physically-grounded model describing the size selection process facilitates calibration of the size selection procedure and optimisation of the exfoliation process. It is hoped that this approach will allow other researchers in the field to improve the selectivity and efficiency of their processes, whilst also providing a framework for standardised comparison of results.

5.4 Conclusions

This chapter has developed a size selection model for liquid-exfoliated 2D nanosheets, which facilitates standardisation of centrifugal processing for production of dispersions with controlled size and thickness. It has been demonstrated that the influence of viscosity on ultrasonic exfoliation may have been neglected in previous analyses and that, when viscosity is suitably accounted for, the results are well described by the chemical physics (surface tension and Hansen parameter matching) for both "good" and "bad" solvents. By using a simple force balance model, it is possible to determine centrifugation parameters for different materials and solvents. This model can be calibrated for a given exfoliation process to facilitate controlled size selection of nanosheets or to characterise and compare exfoliation processes.

Chapter 6

Nanosheet-stabilised emulsions

With the understanding developed from Chapters 4 and 5, this chapter (and the next) seeks to explore how interfacial assembly techniques can be used to fabricate novel structures from, and study the properties of, pristine layered nanosheets. Methods for interfacial assembly typically seek to isolate monolayers, whether molecular or particulate, at the surface of another material or materials [186]. Clearly, for layered nanosheets, this presents a route towards assembly of structures where the degree of exfoliation can be maintained, allowing functional properties to be realised at low loading level.

For graphene, for example, exfoliation leads to high number densities of electrically and thermally conductive nanosheets which can be assembled into conducting films or composites with very low mass per unit area or volume respectively [7, 10]. In addition, nanosheets in such networks have high specific surface area which can facilitate interfacial stress transfer for mechanical reinforcement [140] or energy storage for electrochemical devices [32]. As such, the properties of networks of layered materials are often enhanced (at least relative to their loading level) when the nanosheets are isolated in their few layer forms. Networks can be assembled as composites or hybrid systems [10, 120, 132] to broaden their range of applications. This approach often aims to minimise the quantity of graphene included to maintain other properties such as transparency, flexibility or low cost (of polymers/matrix materials). One route towards this is templated assembly where structuring of

the matrix phase, such as in latex composites, minimises the volume available to nanosheets and reduces the percolation threshold, as previously demonstrated for carbon nanotubes [143].

An alternative approach is Pickering emulsification where nanosheets act as both solid stabiliser and functional filler in an all-liquid system [144, 145]. While previous work has demonstrated emulsification by functionalised clays [146, 147], graphene oxide [148], reduced graphene oxide [149] or graphitic multilayers [150, 152, 151], the lack of a framework for understanding and design of nanosheet-stabilised emulsions has limited the applicability and exploitation of the potential of few-layer nanosheet-stabilised emulsions. This chapter develops a comprehensive understanding of emulsions stabilised by pristine few-layer nanosheets which illustrates their potential for a range of applications.

6.1 Emulsification by pristine few-layer nanosheets

The mechanism of Pickering stabilisation is that two immiscible liquids partially wet the solid stabiliser such that the total interfacial energy is less than that of the oil-water interface [144, 145]. This is typically achieved with a high surface tension "water" phase, most often water, and a low surface tension "oil" phase which can be any water-immiscible organic solvent. Given the poor dispersability of graphene and other pristine layered materials in water (without surfactant, which would act to stabilise an emulsion itself), the most obvious route to formation of these emulsions is by preparing dispersions in the oil phase followed by addition of water, as shown in Figure 6.1. Whether an oil-in-water (o/w) or water-in-oil (w/o) emulsion is formed depends on the relative magnitudes of the interfacial energies at the three-phase boundary between liquids shown in Figure 6.1 and this will be discussed in more detail later in this chapter.

It would be desirable to form these nanosheet-stabilised emulsions with oil phases selected for subsequent applications such as low boiling point liquids for inks, monomers for functional composites, etc. In practise, solvent selection is more

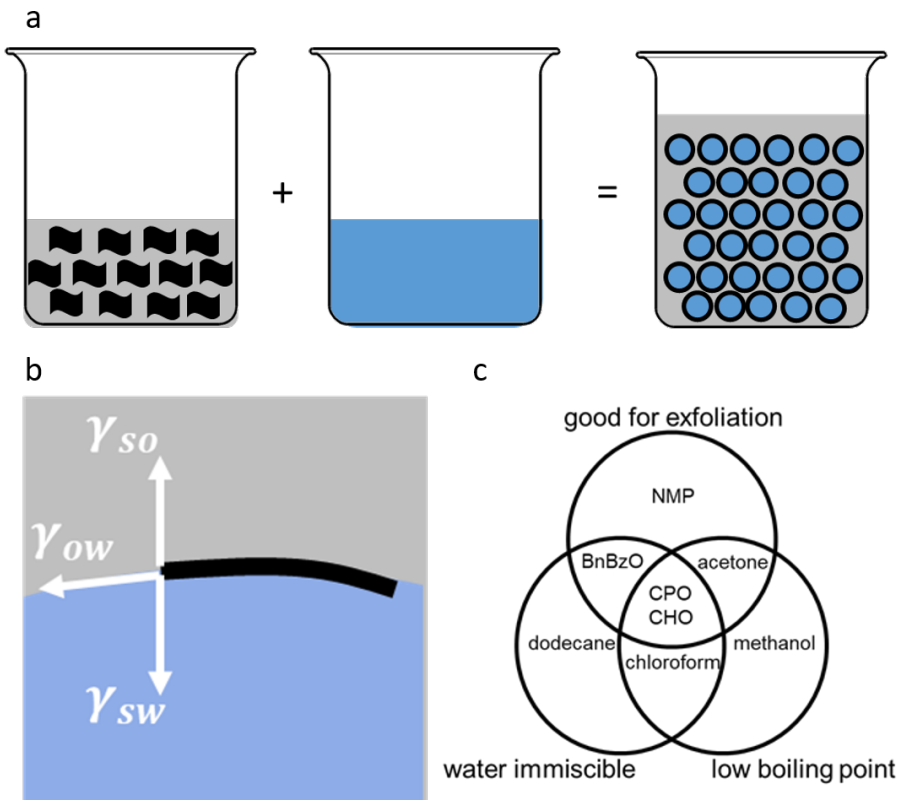

Figure 6.1: (a) Schematic of emulsification process showing exfoliated nanosheets (black) in organic solvent (grey) added to water (blue) to yield water-in-oil emulsion. (b) Stabilisation mechanism in terms of interfacial energies. (c) Solvent selection venn diagram.

challenging as the solvents must be water immiscible, which precludes NMP, DMF, acetone and most alcohols. They must also be sufficiently close in surface energy and Hansen parameters to the stabiliser to allow exfoliation to few-layer nanosheets at reasonable concentration, which precludes chloroform and other non-polar solvents and common monomers such as MMA and styrene, as illustrated in Figure 6.1(b). As such, cyclopentanone (CPO) and cyclohexanone (CHO) are identified as water-immiscible solvents suitable for direct exfoliation, which also have relatively low boiling points (131 and 156 °C) and relatively high vapour pressures. In this study, higher concentrations and better stability were consistently observed for dispersions of graphene in CHO and MoS_2 in CPO (compared with the opposite combination, which cannot be simply explained by any chemical or kinetic arguments but is beyond the scope of this study) and hereafter these are used as the standard exfoliating solvents for these respective materials.

Addition of water to these cycloketone dispersions of few-layer nanosheets (C $\sim$ 0.1 g/L) above the miscibility limit (of $\sim$10:1 cycloketone:water) followed by simply shaking by hand results in the formation of nanosheet-stabilised water droplets in a continuous oil phase. These droplets are typically between 10 and 500 µm in diameter and are optically semi-transparent (as shown in Figure 6.2), indicating that the nanosheets form films of average thickness $<$20 monolayers. It is important to note that films with greater than few-layer thicknesses are typically formed by disordered restacking of the original nanosheets, dictated by the "kinetics" of the film formation during emulsification, rather than "energetics" of restacking with atomic registry as noted in [115]. Therefore, any layer number dependent properties are likely to be retained in the emulsions, as evidenced by the green colour associated with MoS_2 in its few-layer form [56].

Clearly, networks of these droplets have potential for application in functional structures where the templated self-assembly ensures system-scale conductivity with all nanosheets contributing to the network, cf. random composites. Network conductivity increases with reduction of droplet size and corresponding increase

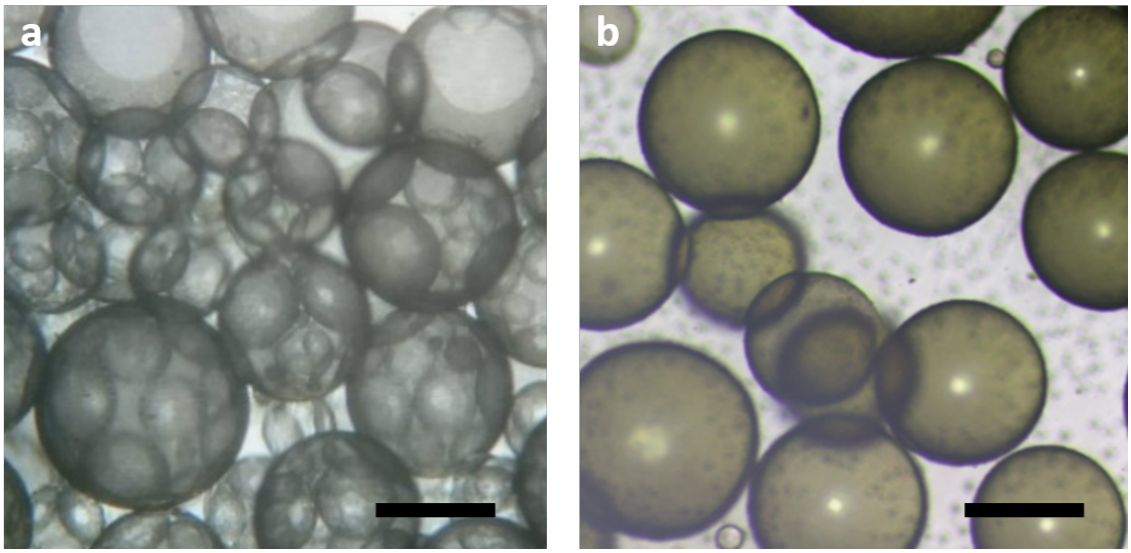

Figure 6.2: Optical micrographs of graphene (a) and MoS_2 (b) emulsions. Scale bars 100 µm.

in number of parallel paths, with the high specific surface area of the nanosheet films ensuring surface coverage and conductivity at a range of loading levels. This was demonstrated in a preliminary study of pristine graphene emulsions, with the encapsulated liquid sysem applied as an electromechanical sensor [151]. For emulsions stabilised by few-layer pristine nanosheets, the relationship between droplet size and loading level will have equally important implications for subsequent applications.

To characterise this, the concentration of the starting dispersions of graphene and MoS_2 was varied before emulsifying the same volume of water. Emulsions with a range of volume fractions and droplet sizes were produced with their average droplet diameter measured by statistical optical microscopy. Figure 6.3 shows the droplet diameter as a function of volume fraction, with droplets between 10 and 300 µm for nanosheet volume fractions across three orders of magnitude below 1 vol.%. Variations between graphene and MoS_2 can be attributed to their differences in specific surface area, any differences in the nanosheets interactions during interfacial film formation and the viscosity of CHO and CPO potentially influencing initial droplet sizes and coalescence dynamics.

In principle, the droplet size in a nanosheet-stabilised emulsion can be geometrically related to the volume fraction and specific surface area to give an expression

for droplet size as a function of nanosheet volume fraction. By assuming that the system consists of droplets of diameter $\langle d \rangle$ with surface area A given by

$$A = \pi \langle d \rangle^2 \tag{6.1}$$

This can be equated to the surface area of the nanosheet stabilised which depends on the mass m of stabiliser, the specific surface area of the monolayer SSA and the thickness of the nanosheet film as a number of monolayers $\langle N \rangle$

$$A = \pi \langle d \rangle^2 = mSSA/\langle N \rangle \tag{6.2}$$

The mass of stabilising nanosheets can be related to the mass of the droplet via the nanosheet volume fraction ϕ

$$m = \phi \rho_{2D} \pi \langle d \rangle^3 / 6 \tag{6.3}$$

By combining the two equations above

$$\pi \langle d \rangle^2 = \phi \pi \langle d \rangle^3 \rho_{2D} SSA/6\langle N \rangle \tag{6.4}$$

Rearranging to give $\langle d \rangle$ in terms of ϕ and noting that for layered materials, SSA is simply the reciprocal of the product of density ρ_{2D} and interlayer spacing c_{2D} gives

$$\langle d \rangle = \frac{6 c_{2D} \langle N \rangle}{\phi} \tag{6.5}$$

where ϕ is the volume fraction of the nanosheets relative to the droplet phase and $\langle N \rangle$ here denotes the film thickness as a number of monolayers, rather than the thickness of the individual nanosheets. It is noted that fitting this model assumes that the thickness of the stabilising film is independent of loading level and in practise often gives an offset in droplet size, whereas power law fitting gives an exponent of around 0.5, rather than 1, as shown in Figure 6.3.

These deviations from the expected scaling are mathematically equivalent to $\langle N \rangle$

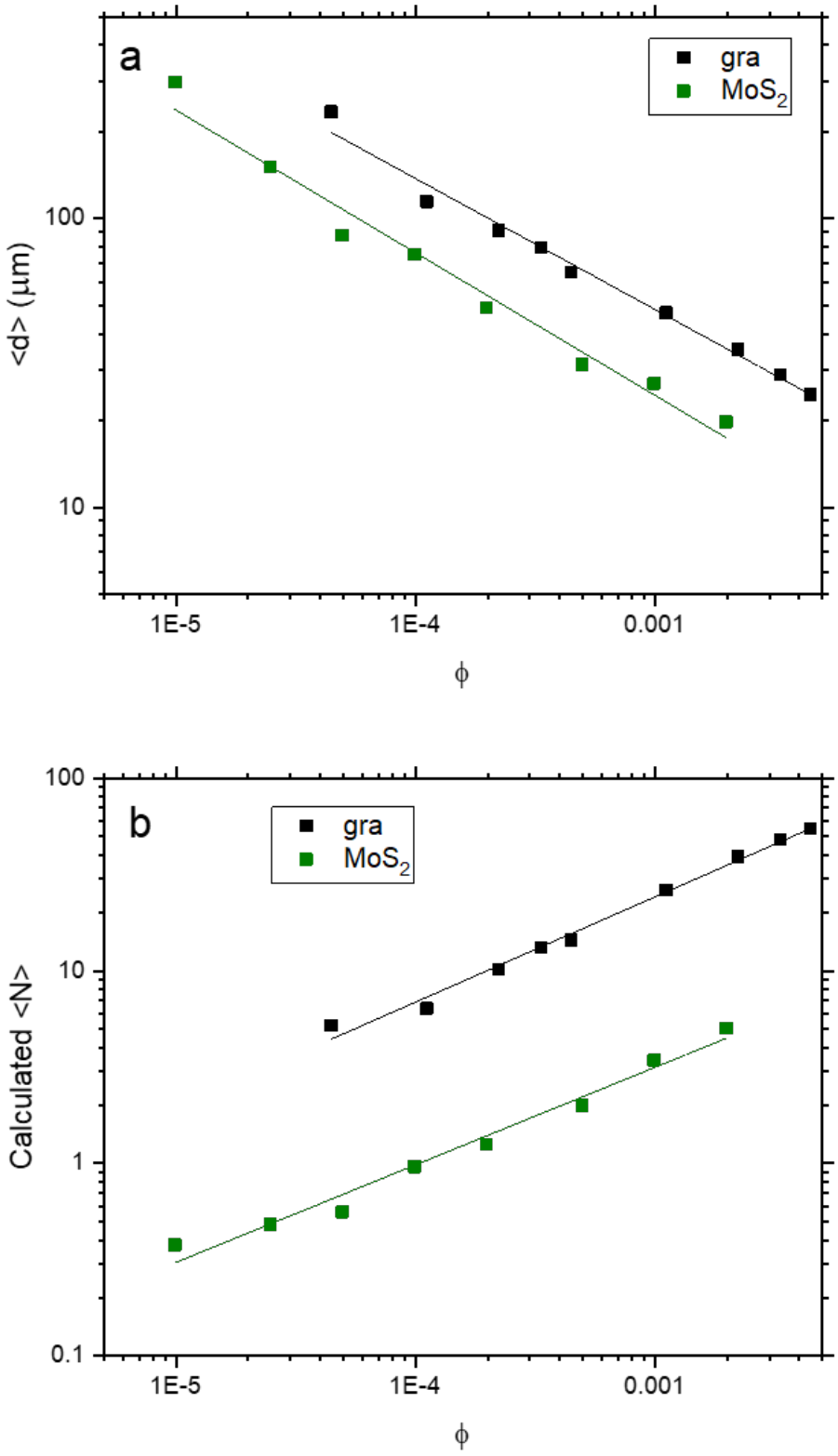

Figure 6.3: (a) Average droplet diameter as a function of nanosheet volume fraction, with power law fitting with exponents of -0.45 and -0.49 for graphene and MoS_2 respectively. (b) Calculated layer number as a function of nanosheet volume fraction with power law fitting with exponents of -0.55 and -0.51 for graphene and MoS_2 respectively.

also varying with volume fraction, where the droplets are being overcoated with more than one layer of nanosheets. There are several reasons for this. Firstly, the theoretical droplet size for nanosheets with average layer number of 5 at volume fraction 0.1 vol.% is around 1 µm. As this is approaching the length of the nanosheets themselves, it is not possible to stabilise droplets of this radius without reducing the nanosheet size to allow them to assemble on the spherical surface.

Secondly, this droplet size is likely lower than the average droplet size produced by homogenisation of the two liquids at this shear rate, so higher shear and smaller nanosheets are required to stabilise sub-10 µm droplets. In addition, the dynamics of droplet formation and availability of stabiliser results in larger than expected droplets and overcoating of their surfaces. When droplets of one liquid are formed in another, they must diffuse under homogenisation to become coated and stabilised. This typically results in coalescence until they are sufficiently larger than the sheets and have become fully coated which may result in the formation of high $\langle N \rangle$ films at the nanosheet-stabilised interfaces, as shown in Figure 6.3.

These calculated film thicknesses, as a number of monolayers, suggest that a scaling of the form $\langle N \rangle \sim \sqrt{\phi}$ with values between 5 and 50 for the graphene samples and 0.3 and 5 for the MoS_2 samples. Given that these calculations account for specific surface area of the materials, this perhaps indicates some difference in the way the nanosheets assemble to stabilise the interface. In particular, the near- and sub-unity values obtained for MoS_2, where the constituent nanosheets have greater average layer number ($\langle N \rangle \sim 5$), might suggest stabilisation with more sparse assembly of nanosheets than is the case for graphene where overcoating results in much thicker interfacial films. This is also convolved with any solvent effects, where the greater viscosity of CHO may result in larger droplets, lower surface area and greater overcoating for graphene compared with MoS_2. Nevertheless, the robustness of the $\langle d \rangle \sim 1/\sqrt{\phi}$ scaling across both materials suggests some well-defined physics governs droplet formation and potentially allows for empirical modelling where a single fitting constant relates droplet size and volume fraction for emulsions stabilised

by few-layer nanosheets.

Interestingly, disordered restacking in these films results in retention of the degree of exfoliation as shown by the Raman mapping of a drop-cast single droplet of MoS_2 emulsion in Figure 6.4, where $\langle N \rangle_{ns} \sim 5$. This opens up potential applications of emulsions as inks where high concentration can be achieved in energetically (rather than solely kinetically) stable inks without the addition of viscosity modifiers, binders or other additives. This would allow deposition of relatively thick films from single droplets where the interfacial film deposited may be tens of nanometres.

Moreover, the above indicates that stable emulsions ($\langle N \rangle_{ns} = 5$ and $\langle d \rangle = 10$ µm) can be formed with volume fractions as low as 10^{-5} (0.001 vol.%). As these droplets sediment to pack together into dense networks, even with an interfacial layer of oil between adjacent water droplets, they exhibit system-scale conductivity which is appreciably higher than that of the water or oil phase and can be attributed to the formation of conductive films on the surface of droplets and tunnelling through the ultra-thin oil layers between droplets. Importantly, the conductivity increases with volume fraction indicating that it is indeed a property of the templated structure, where smaller droplets result in the formation of more parallel paths.

The conductivity in these droplet networks highlights that layered nanosheets with a high degree of exfoliation, despite their high absolute resistance, can facilitate system-scale conductivity at ultra-low loading levels as a consequence of their templated structure. Interestingly, these interfacial films do not exhibit percolative behaviour typically associated with nanocomposites; there is no clear percolation threshold because reducing the volume fraction simply increases the droplet size until there is a single large droplet whose diameter is approaching the size of the container. Even then, system-scale conductivity can be maintained by using a larger container until there is simply not enough stabiliser to coat the droplet. In principle, centimetre-scale droplets could be formed $\langle N \rangle = 5$ and $\phi = 10^{-7}$ (0.00001 vol.%) and would still form a conductive network.

As such, their conductivity-volume fraction relationship can be fitted to power

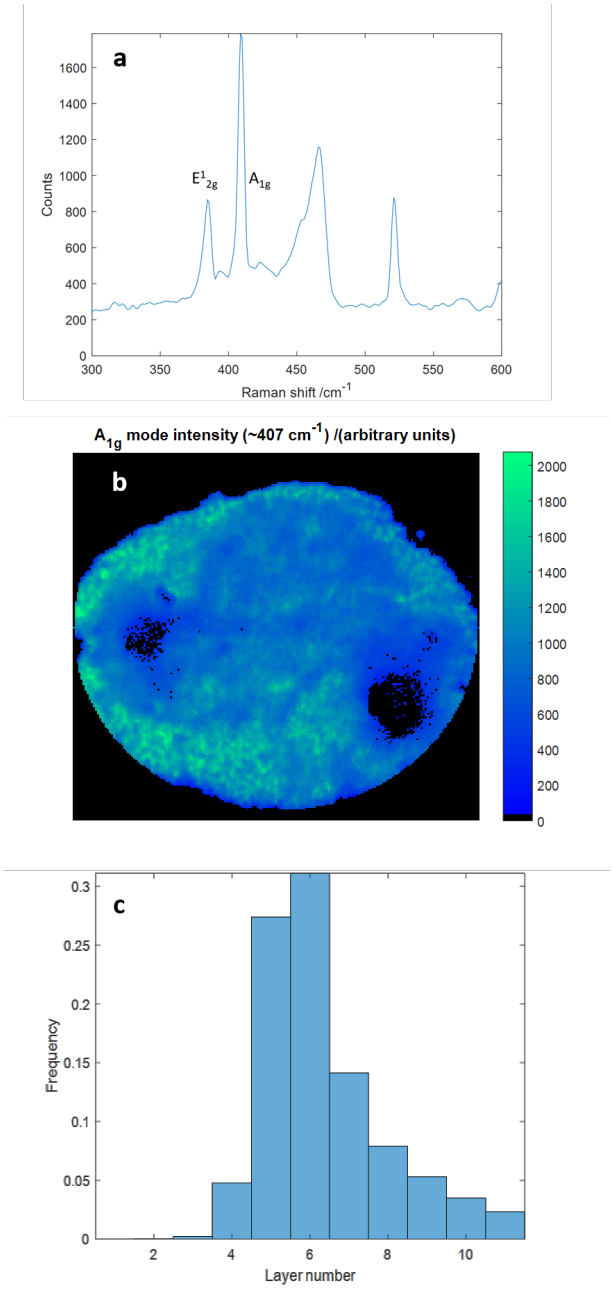

Figure 6.4: (a) Representative Raman spectrum of deposited MoS_2 emulsion droplet showing E^1_{2g} (in-plane) and A_1g (out-of-plane) modes (b) Raman mapping showing A_1g intensity and (c) analysis using E^1_{2g} (in-plane) A_1g (out-of-plane) mode separation and relationship to layer number from previous studies of mechanically-exfoliated MoS_2 [187].

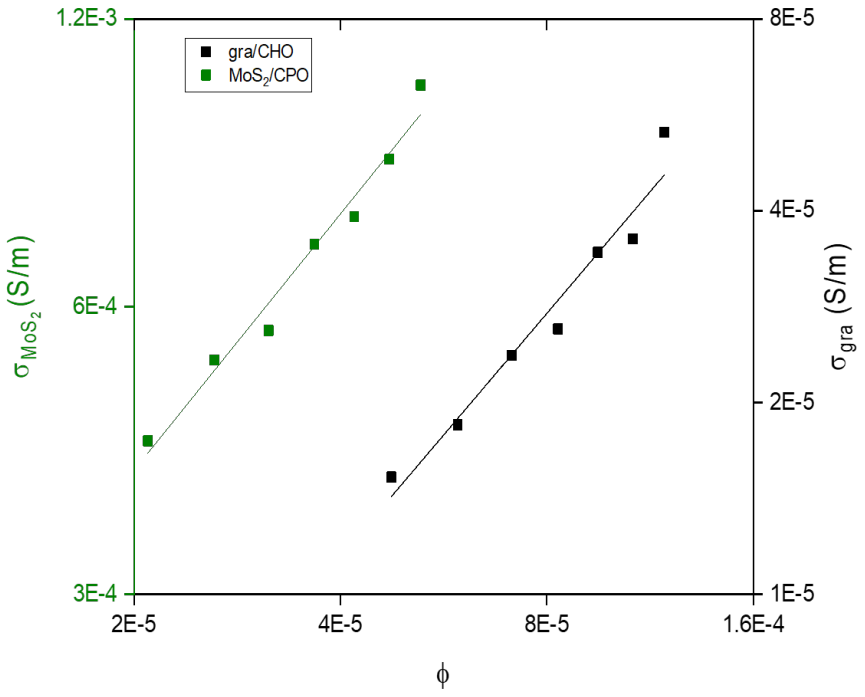

Figure 6.5: Emulsion conductivity as a function of nanosheet volume fraction for graphene and MoS_2 with power law fitting with exponents 1.27 and 0.89 respectively.

law scalings, as shown in Figure 6.5, which are simply percolation curves, accounting for the scaling of paths in the network, but with ultra-low (negligible) threshold. To the best of our knowledge, these are the lowest loading levels ever reported for graphene-based conductive networks and yet still have conductivities approaching those of typical graphene-polymer composites [10]. This approach has enormous potential for the production of ultra-low loading conductive composites, mechanical reinforcement and electrochemical devices.

6.2 Emulsion stability and orientation

In order to realise this potential, it will be necessary to form nanosheet-stabilised emulsions with liquids other than water and cycloketones. However, for the reasons illustrated in Figure 6.1(b), it is quite challenging to use alternative solvents while retaining the high degree of exfoliation required for ultra-low loading applications.

In practice, this can be achieved using a solvent transfer step based on liquid cascade centrifugation [57]. Dispersions are prepared in cycloketones as normal and subjected to further centrifugation to sediment the majority of the nanosheets, the supernatant is discarded and the sediment is redispersed into an alternative solvent of choice before immediate emulsification. This allows for production of well-exfoliated materials in solvents where this would not be possible by direct exfoliation such that few-layer nanosheet-stabilised emulsions can be produced with relatively arbitrary oil and water phases.

This approach allows us to investigate emulsification of liquids with different surface tensions to modify the three-phase boundary shown in Figure 6.1(a). Having established that graphene, MoS_2 and BN are capable of stabilising water-in-cycloketone emulsions, suggesting preferential wetting of the nanosheets by the cycloketone compared with the water, it was noted that less polar oil and/or water phases would be required to produce oil-in-water emulsions. Emulsions of water and dichloromethane (DCM) were found to still form as water-in-oil but with buoyant water droplets that remain stable at the interface with the air. Reducing the polarity of the oil phase as far as pentane results in formation of oil-in-water emulsions albeit with reduced surface area and increased droplet size due to the challenges of redispersing graphene into such a non-polar solvent. In addition, these oil droplets are buoyant in water and rise to the air interface where they burst and spread at the surface. Alternatively, it was found that by reducing the polarity of the water phase – by using ethylene glycol – it is possible to form oil-in-water emulsions with almost any immiscible organic (DCM, pentane, etc.).

Based on the above, nanosheet-stabilised emulsions can be classified as either oil-in-water or water-in-oil and either buoyant or non-buoyant, as illustrated in Figure 6.6. In general, oil droplets are found to be unstable at the air interface, until ruptured droplets form a film of nanosheets against which remaining droplets are stable. Water droplets are stable at the air interface when buoyant but are often non-buoyant and unstable on certain hydrophilic substrates including glass,

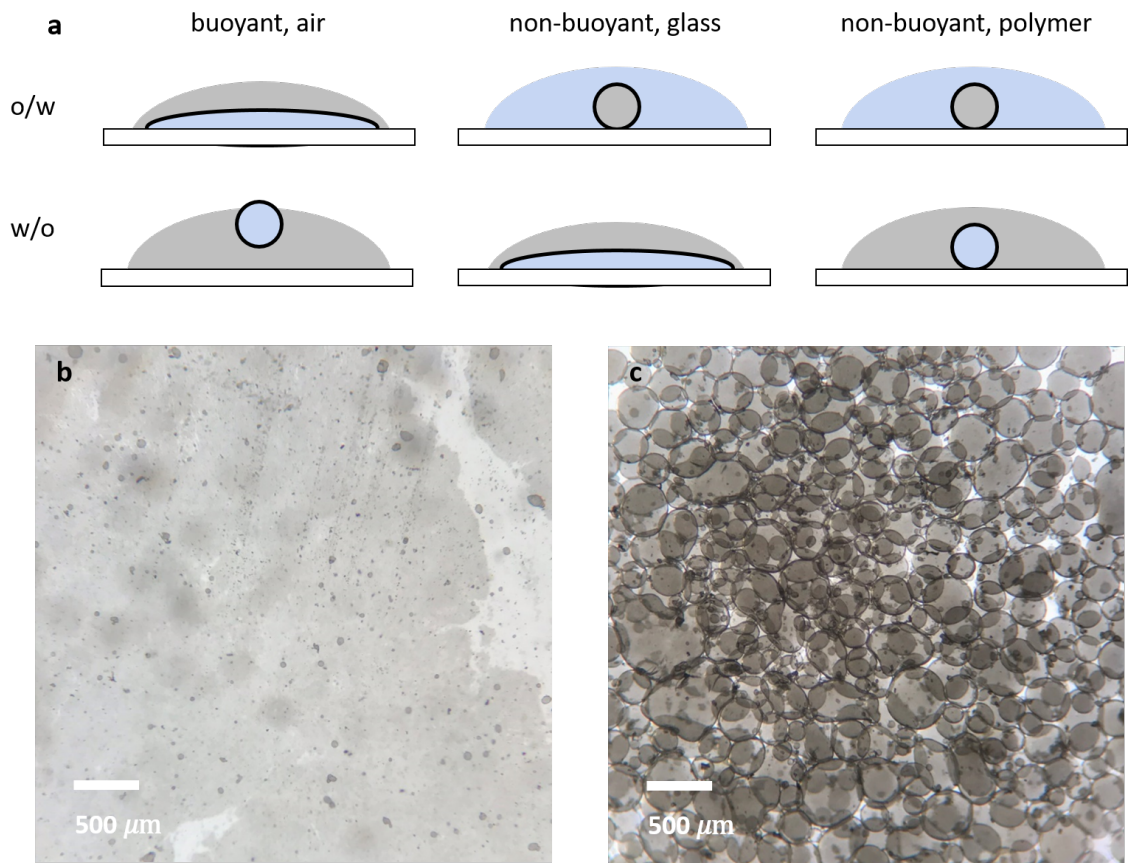

Figure 6.6: (a) Emulsion stability at air and substrate interfaces and optical micrographs of (b) unstable buoyant droplet and (c) stable non-buoyant droplet emulsions.

and therefore must be stored in silanised vials. Water droplets are however stable against polymeric substrates, with (non-buoyant) oil droplets stable against almost all substrates. These observations provide an insight into the stability criteria and inversion threshold of these emulsions, from which it should be possible to develop a design framework for nanosheet-stabilised emulsions.

The stability and orientation (whether oil-in-water or water-in-oil) of these emulsions is determined by the three-phase boundary and associated interfacial energies and spreading coefficients. These are defined as

$$S_{so} = \gamma_{so} - \gamma_{sw} - \gamma_{ow} \tag{6.6}$$

$$S_{sw} = \gamma_{sw} - \gamma_{so} - \gamma_{ow} \tag{6.7}$$

where S_{so} and $_{sw}$ are the spreading coefficients for solid/oil and solid/water inter-

faces respectively and the subscripts of the surface energies γ denote the contributions as shown in Figure 2.10. The criterion is typically that they must both have the same sign (positive or negative) for an emulsion to be stable, where one phase preferentially wets the solid stabiliser and therefore forms the continuous phase while the other forms the droplet phase [144].

While interfacial tensions between liquids can be measured using the Wilhelmy plate method at a submerged interface, it would be preferable to have an understanding of the spreading coefficients as a continuous function of the individual and well-known surface tensions of the liquids. To facilitate this, one of two well-established simple models for interfacial tension as a function of surface tension (one using a geometric mean term and the other using an arithmetic mean term [188, 189, 151]) can be employed;

$$\gamma_{ab} = \gamma_a + \gamma_b - 2\sqrt{\gamma_a \gamma_b} \tag{6.8}$$

$$\gamma_{ab} = \gamma_a + \gamma_b - 4\frac{\gamma_a \gamma_b}{\gamma_a + \gamma_b} \tag{6.9}$$

These allow calculation of the spreading coefficients for a given emulsion composition, as shown for graphene and water (as a function of oil surface tension) in Figure 6.7.

It is important to note that surface tension and surface energy are used interchangeably in the context of graphene and related materials. The surface energy of a liquid is simply the sum of surface tension, which is directly measurable, and the surface entropy which takes a value of 29 mN/m for all liquids at room temperature [111]. For graphene and related materials, as solids, the surface entropy (and therefore surface tension) is poorly-defined and therefore it is more correct to infer the surface *energy* from its interaction with liquids of known surface energy [14] or by inverse gas chromatography [116, 117]. As such, liquid-exfoliated graphene is understood to have a surface energy close to 70 mJ/m^2 based on good exfoliation

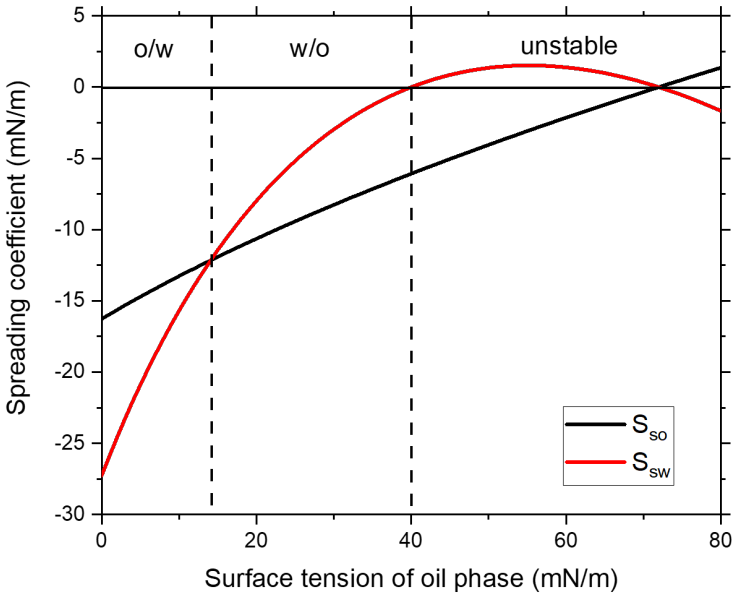

Figure 6.7: Spreading coefficients as a function of surface tension of oil phase for graphene-stabilised emulsion with water.

and dispersion into solvents with surface tensions close to 40 mN/m.

As a starting point, this value of $\gamma = 70$ mJ/m^2 is taken to allow determination of the stability and orientation of emulsions as a function of the surface tension of the oil phase as shown in Figure 6.7. It is noted that these models give a reasonable approximation to the measured interfacial tensions for most liquids but fail to describe some other phenomenology associated with three-phase interfaces. This requires a model which captures more of the chemical physics of those interface and will be discussed in the next chapter [190]. Nevertheless, the chemical model is not well-defined for solids and the simple geometric and harmonic models are found to accurately describe the stability and orientation of these emulsions, likely due to the fact that spreading coefficients are a comparison of the relative magnitude (rather than absolute value) of the interfacial energies.

The stability of a graphene/water interface with a third phase is limited to those with surface energy less than graphene itself, confirming that graphene-stabilised water droplets should not be stable in contact with high surface energy substrates such as glass. Figure 6.7 also indicates that graphene/water interfaces are stable for

oil phases with surface tensions as low as 0 mN/m (air), verifying the observation of stable buoyant water droplets. Furthermore, this spreading coefficient analysis shows an inversion point (where the lines intersect) close to the surface energy of pentane, which was the lowest surface tension solvent tested and the only one to give oil-in-water. These results indicate that this analysis using spreading coefficients, an interfacial tension model and approximate surface energy for graphene capture the underlying physics of emulsion stability and orientation.

In order to further formalise this understanding of emulsion stability and orientation based on surface tensions of the liquids, the relationship between the spreading coefficients and the models for their constituent interfacial tensions must be considered.

From their definitions, the spreading coefficients can be rearranged to give

$$S_{so} + \gamma_{wo} = \gamma_{so} - \gamma_{sw} \tag{6.10}$$

$$S_{sw} + \gamma_{wo} = \gamma_{sw} - \gamma_{so} \tag{6.11}$$

As such, it can be shown that

$$S_{so} + S_{sw} = -2\gamma_{wo} \tag{6.12}$$

Since interfacial tensions/energies are positive, spreading coefficients can only have the same sign (and thereby form a stable emulsion) if that sign is negative. If both spreading coefficients are negative, the stability criteria can be expressed as

$$\gamma_{so} - \gamma_{sw} < \gamma_{wo} \tag{6.13}$$

$$\gamma_{sw} - \gamma_{so} < \gamma_{wo} \tag{6.14}$$

Since $\gamma_{so} - \gamma_{sw} = -(\gamma_{sw} - \gamma_{so})$, one of the above equations will always be satisfied and the criterion reduces to

$$|\gamma_{so} - \gamma_{sw}| < \gamma_{ow} \tag{6.15}$$

Based on the geometric and harmonic mean models, it can be intuitively argued that it is most easily satisfied by $\gamma_o \ll \gamma_w$ (giving large γ_{ow}) and $\gamma_s \sim \gamma_o$ and $\gamma_s \sim \gamma_w$ (giving $\gamma_{so} \sim \gamma_{sw}$ and the difference is small), which requires that $\gamma_o < \gamma_s < \gamma_w$, as illustrated in Figure 6.7, although this is more challenging to demonstrate rigourously.

However, in order to explicitly state this condition, interfacial energy models are required. The orientation of an emulsion (o/w or w/o) is also determined by the spreading coefficients, i.e. whichever is more negative forms the droplet phase; o/w for $S_{so} < S_{sw}$ and w/o for $S_{so} > S_{sw}$. As such, the point at which they are equal can be considered the inversion threshold for an emulsion. This can be simplified (by definition and without any empirical models) as

$$\gamma_{so} = \gamma_{sw} \tag{6.16}$$

where the phase which has the lowest interfacial tension with the solid will form the droplets, independently of the interfacial tension of the two phases.

So this inversion threshold can be further simplified, by substituting Equation 6.8 into Equation 6.16 to be given in terms of surface energies

$$\sqrt{\gamma_o} + \sqrt{\gamma_w} = 2\sqrt{\gamma_s} \tag{6.17}$$

where lower surface energies of the liquid phases give o/w and higher surface energies give w/o, and the threshold itself is determined by the surface energy of the solid stabiliser; in this case, the layered nanosheets.

In practise, this equation describes all experimental observations in terms of stability and orientation for all combinations of liquids, air and substrate interfaces and nanosheet type (graphene, MoS_2 and BN), confirming the nanosheet surface energies to be close to 70 mJ/m^2 as shown in Figure 6.8. Interestingly, and perhaps

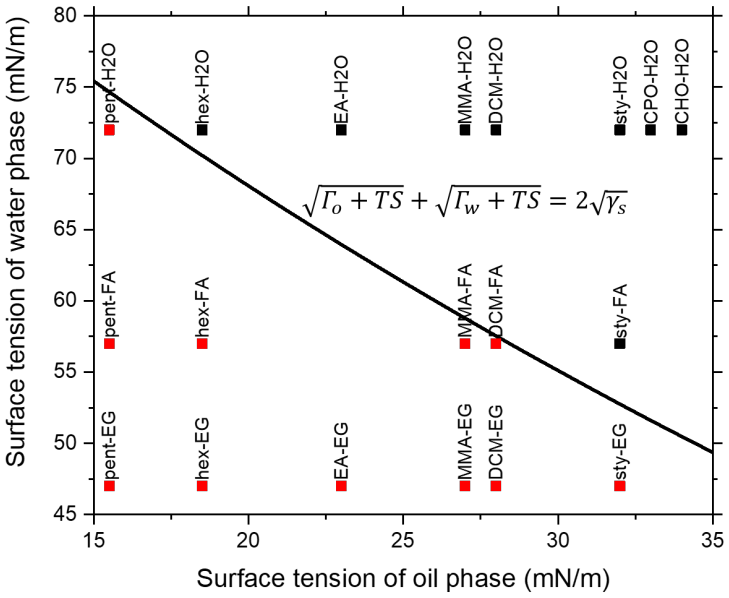

Figure 6.8: Surface tension phase diagram for nanosheet-stabilised emulsions showing inversion threshold for pristine nanosheets where Γ_o and Γ_w are the surface *tension* of the oil and water phases respectively, TS is the product to absolute temperature and surface entropy and γ_s is the surface *energy* of the stabilising nanosheets.

surprisingly, substituting the harmonic mean interfacial tension into Equation 6.16 or at any stage of the analysis, gives numerically identical inversion thresholds, likely due to the robustness of the scalings of interfacial energies with constituent surface energies in terms of relative magnitudes. Importantly, this equation only describes all experimental results when considering surface energies (rather than tensions) as the interfacial properties are non-linearly related to individual surface properties. In addition, the same emulsion orientations are observed for graphene, MoS_2 and BN for both exfoliated dispersions and bulk powders suggesting they have little to no difference in their effective surface energies.

Furthermore, using this equation it is possible to measure the surface energy of layered nanosheets based on inversion of an emulsion by changing its composition. To perform this measurement on well-exfoliated few-layer nanosheets, cycloketone dispersions were diluted with pentane and immediately emulsified with water to determine their orientation as a function of pentane volume fraction. The surface tension of the cycloketone/pentane dispersions was measured and used to calculate

bounds of the surface energy of the nanosheets based on the emulsion orientation. Inversion of these emulsions was observed to occur at a pentane volume fraction between 0.90 and 0.95, with a surface tension of ∼17 mN/m, corresponding to a nanosheet surface energy of 71±0.5 mJ/m^2.

This is consistent with the observations for pristine solvent combinations where DCM/formamide and hexane/water emulsions set bounds of 70.0 and 72.0 mJ/m^2 respectively, in an area-weighted fashion. Furthermore, these results are largely consistent with inverse gas chromatography measurements of surface energies as a function of nanosheet size [116, 117]. This method was used to determine the intrinsic basal plane surface energy of graphene to be 61 mJ/m^2 with basal plane and edge defects contributing 180 and 130 mJ/m^2 respectively. Given the low basal plane defect density in graphene, the effective surface energy is dominated by the size effects associated with the difference between the intrinsic basal plane surface energy and that of edge defects as shown in Figure 6.9. In the size range of liquid-exfoliated nanosheets, where the length distributions will always be weighted towards the surface energy of larger nanosheets by area averaging, surface energies are in the range 65 to 75 mJ/m^2, consistent with all dispersions studied here which typically have ⟨L⟩ between 100 and 400 nm.

This does suggest that smaller nanosheets would have sufficiently high surface energy to invert some w/o emulsions (e.g. MMA/water) and that larger nanosheets would have sufficiently low surface energy to invert some o/w emulsions (e.g. EA/EG). In practise, these extremes of nanosheet size are very difficult to produce and disperse in quantities large enough to emulsify. In addition, as discussed above, bulk powders are found to have effective surface energy closer to the average-sized exfoliated nanosheets than that of larger nanosheets. This could be due to their non-negligible thickness and associated increase in edge sites at their surface, coupled to potential roughness effects on their effective surface energy. Size effects on emulsion orientation remains an area of interest for future work.

This model represents a coherent framework for understanding and design of

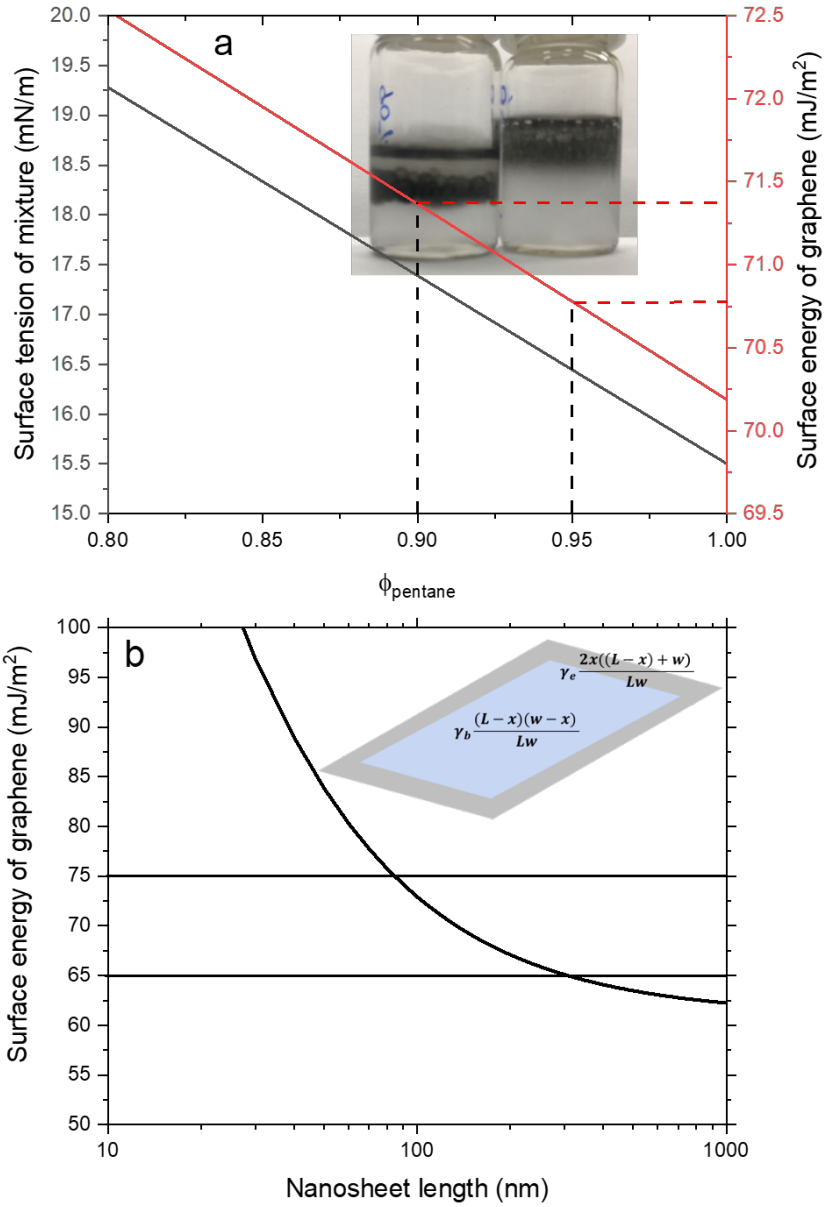

Figure 6.9: Nanosheet surface energy by emulsion inversion; (a) oil phase surface tension and resultant nanosheet surface energy as a function of pentane volume fraction, inset photograph of water-in-oil emulsion with $\phi_{pentane}$=0.9 and oil-in-water emulsion with $\phi_{pentane}$=0.95 and (c) nanosheet surface energy as a function of nanosheet length based on previously reported model [116, 117] where γ_b and γ_e are the surface energies of the basal plane and edge respectively, l is length, w is width and k is the width of the edge-like region.

nanosheet-stabilised emulsions and the apparent robustness of nanosheet surface energy to material, size, etc. enhances the possibilities of using liquid processing to prepare controlled structures with a range of functional properties.

6.3 Emulsion inks

This design framework coupled with the ability to disperse nanosheets (in disordered films) at concentrations greater than 10 mg/mL with energetic, rather than solely kinetic, stability, highlights their suitability for use as inks for deposition of nanosheet networks.

As illustrated by Figure 6.1, the ideal combination of solvent properties for an emulsion ink would be suitability for exfoliation, water immiscibility and low boiling point. In addition, the stability considerations illustrated in Figure 6.7 are particularly important for emulsion ink design, where o/w emulsions, achieved through use of high boiling point EG, are typically buoyant and unstable at the air interface. While w/o are unstable on high surface energy substrates, deposition onto low surface energy (solvent resistant) polymeric substrates such as PET is well-suited for applications of nanosheet networks for flexible electronics. This also allows preparation of suitable inks directly from dispersions in cycloketone solvents.

In addition, the stability of deposited water droplets on polymeric substrates confers a degree of spatial control to deposition of emulsion inks even when depositing drop-wise by hand. As shown in Figure 6.10, water droplets are stable on substrate until spreading and evaporation of the capping layer of solvent. The exposed graphene-coated water droplet then forms an unstable three-phase interface with the air (only stable for air-in-water), resulting in deformation, drying and collapse of the droplet onto the substrate. By contrast with dispersions, where wetting of the substrate by the liquid results in loss of any spatial control and drying results in some degree of coffee-ring effect, the osmotic pressure-driven collapse of these droplets appears to minimise this effect in emulsion inks as shown by the uniform intensity of the Raman mapping in Figure 6.4.

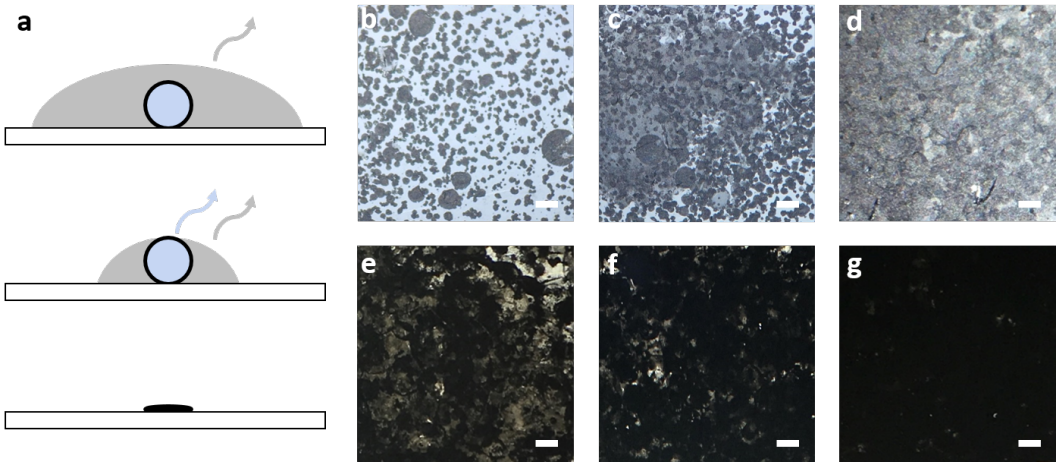

Figure 6.10: (a) Schematic of emulsion deposition showing initial evaporation of solvent capping layer followed by collapse of exposed water droplet. (b)-(g) Optical micrographs of graphene film deposited from emulsion with increasing number of passes. Scale bars 500 µm.

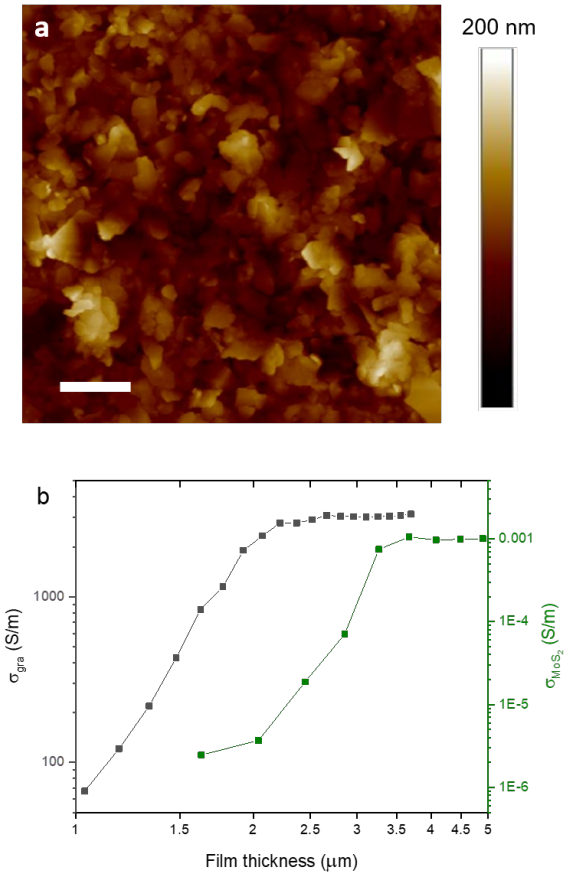

Figure 6.11: (a) Atomic force micrograph of deposited film of graphene emulsion, scale bar 500 nm. (b) conductivity as a function of thickness for deposited films of graphene and MoS_2 emulsions.

This uniform drying and spatial control of emulsions, along with the ability to prepare at higher concentrations than dispersions, facilitates drop-wise deposition of nanosheet networks by hand with greater control than drop casting or spray coating from dispersions, with a view to inkjet printing in future. The deposited nanosheets form dense packed networks as shown in the AFM height image in Figure 6.11 with system-scale electronic conductivity in both graphene and MoS_2 films. Interestingly, the conductivities exhibit thickness-dependent scaling as observed previously but the macroscopic non-uniformity introduced by depositing by hand results in critical thicknesses of ∼1 µm, cf. 50-200 nm in previous studies of vacuum filtration or inkjet printing [7, 11]. Nevertheless, the measured conductivities of graphene and MoS_2 films reach bulk-like thickness-independent values of ∼3000 S/m and ∼0.001 S/m respectively, with the latter discussed in detail in Chapter 7.

In order to be suitable for inkjet deposition, these emulsions also require a viscosity (∼0.01 Pa.s) greater than that of common solvents at the shear rates applied during jetting (∼10^6 s^{-1}). As Newtonian fluids, the viscosities of most solvents is independent of shear rate. By contrast, emulsions can exhibit non-Newtonian behaviour with viscosities which are strongly dependent on shear rate [191]. Figure 6.12 shows preliminary rheological measurements of a representative graphene-stabilised emulsion using a parallel plate viscometer for shear rates between 0.1 and 100 s^{-1}. Most notably, this shows that nanosheet-stabilised emulsions exhibit non-Newtonian shear-thinning behaviour with a well-defined and hysteresis-free dependence on shear rate. This near-power-law scaling for the shear rate regime measured here (∼1 Pa.s at ∼0.1 s^{-1} and ∼0.01 Pa.s at ∼100 s^{-1}) indicates that these emulsions have the potential to be modified to give the desired rheological properties.

While these water-in-cycloketone emulsions reach the viscosity required for inkjet printing at 100 s^{-1}, 10^4 times lower shear rate than during jetting, it it possible that viscosity will rapidly saturate at higher shear rates as shown previously for clay-stabilised water-in-oil emulsions [192]. Alternatively, it may be possible to use

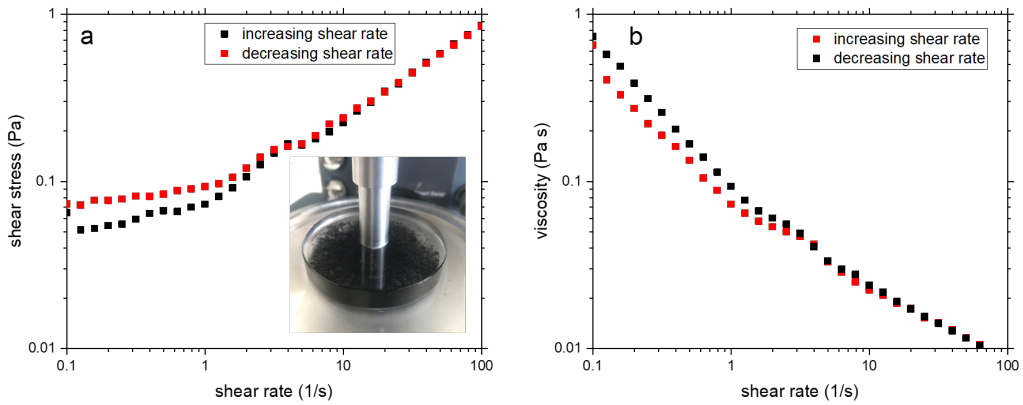

Figure 6.12: Rheological characterisation of graphene-stabilised emulsion with shear stress and viscosity as a function of shear rate.

dilute emulsions (with lower ratio of droplet to continuous phase) which are known to exhibit Newtonian behaviour with viscosity independent of shear rate [191] to ensure the desired viscosity during jetting. However, this does mean reducing the concentration of the emulsion ink and potentially using a high viscosity (likely high boiling point) continuous phase, the selection of which must also satisfy other criteria for surface energy, nanosheet dispersability, etc. A more practical alternative might be to manipulate the shear rate-dependent viscosity by controlling emulsion droplet size. It is well known that smaller droplets in a concentrated emulsion give rise to increased viscosity [191, 193] which presents a route to ensure sufficient viscosity during inkjet. Optimisation of this effect for nanosheet-stabilised emulsions, with phases suited for deposition, requires a systematic study to characterise rheology and correlate with the structure and properties of printed traces to realise the potential of emulsions as inks for printed electronics.

6.4 Conclusions

In this chapter, it has been demonstrated that nanosheet-stabilised emulsions represent a relatively unexplored approach for assembly of layered materials where the combination of high surface area and functional properties have much promise for applications. As acknowledged previously, functionalised layered materials

including clays and graphene oxide have been studied in some depth, likely due to their dispersability in water and formation of polymerisation-suited oil-in-water emulsions [146, 147, 145, 148]. However, their chemical functionalisation typically renders them non-conductive, limiting their application to structural (rather than functional) assemblies. By contrast, pristine layered materials have poor dispersability in water, often resulting in lower degree of exfoliation and accessible surface area, and form water-in-oil emulsions, for which it is more challenging to develop applications [150, 152, 151]. Here, through solvent selection/transfer and modelling of emulsion droplet size, stability and orientation, it has been possible to develop a framework for preparation of emulsions stabilised by pristine few-layer nanosheets. Graphene- or MoS_2-stabilised water-in-cycloketone emulsions have been shown to exhibit system-scale conductivity in their as-produced liquid form. Conductivities of $\sim 10^{-4}$ S/m at nanosheet volume fractions of $\sim 10^{-5}$ have been obtained, which represent the lowest loading level nanosheet-containing conductive composites ever reported. Their potential as emulsion inks is highlighted by the ability to drop-cast by hand into films with conductivities equivalent to other deposition techniques, facilitated by their high concentration and drying dynamics which gives spatial control, which would not be possible with standard dispersions.

Of course, to exploit the full potential of these emulsion structures, other compositions will be required to form polymer composites, optoelectronic devices, phase change materials, etc. For such applications, it will often be necessary to form oil-in-water emulsions where the water phase can be removed to form dry or solid structures. Based on the understanding of surface energy developed here, this can be most easily achieved through use of ethylene glycol as the water phase. However, the high boiling point and increased potential for chemical interactions (compared with water) means ethylene glycol can be difficult to remove and/or can interfere with polymerisation or other *in situ* reactions. Alternatively, oil-in-water emulsions can be realised with water as the water phase by increasing the surface energy of the stabilising nanosheets by some mild functionalisation which retains their the

conductive nature, although emulsions stabilised by rGO reduced to the point of being conductive find that this still gives w/o emulsions [149]. Other approaches to increase the surface energy of pristine nanosheets include controlled size selection of small, high-edge-density nanosheets which may be sufficient to yield o/w emulsions. Future work will seek to understand the size dependence of nanosheet surface energy with a view to controlling emulsion orientation.

Finally, it is important to consider how the dispersability (and subsequently degree of exfoliation, accessible surface area, loading levels, etc.) will affect emulsions of arbitrary compositions. While solvent transfer from cycloketones facilitates preparation of reasonable concentrations without catastrophic reaggregation in most solvents, it would be preferable to prepare nanosheets in a phase which allows direct emulsification with a third phase specific to the application. Clearly this would have to be water and therefore requires the addition of surfactant in order to prepare dispersions of pristine nanosheets. It has been observed that, for surfactant concentrations typically used for exfoliation (∼1:5 surfactant:bulk layered material), the surfactant acts to stabilise o/w interfaces while the nanosheets act to stabilise w/o interfaces, resulting in phase separation of the whole emulsion. This perhaps suggests that surfactant and nanosheets act independently and that removing any free surfactant may allow emulsification of stable structures. By using lower initial surfactant concentration (∼1:100 surfactant:bulk layered material), it has been possible to form such emulsions as shown in Figure 6.13 which exhibit the same orientation as for solvent-exfoliated nanosheets. This approach requires further investigation but highlights the potential of additives to facilitate emulsification.

Inspired by this observation (and the use of acidic conditions to destabilise GO in dispersion to allow emulsification), preliminary experiments have been performed to investigate the influence of pH on pristine nanosheet-stabilised emulsions. The stability of GO in water is attributed (in part) to the de-protonation of functional groups such as hydroxides (R-OH to R-O^-) which increases their polarity and thereby effective surface energy, moving it closer to that of water. By acidifying the water, the

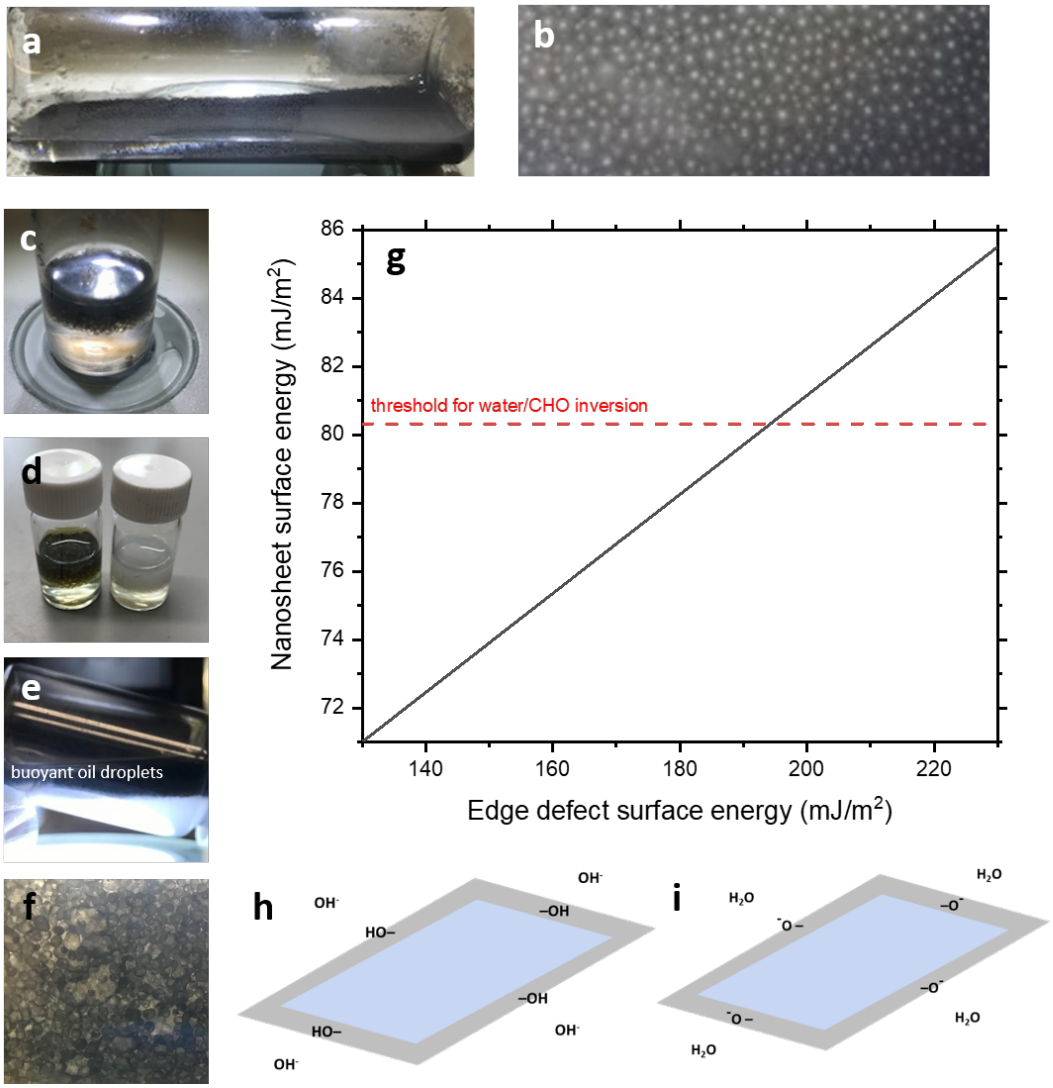

Figure 6.13: (a) Photograph and (b) optical micrograph of surfactant-exfoliated nanosheet-stabilised water-in-CHO emulsion, showing same stability and orientation as for solvent-exfoliated nanosheets. (c) Graphene and (d) MoS_2 and BN emulsions inverted by emulsification under basic conditions (pH 13 KOH). (e) Photograph showing buoyant droplets indicating inversion and (f) optical micrograph of buoyant oil droplets. (g) Calculated nanosheet surface energy as a function of edge defect surface energy based on model from [116, 117] as proposed mechanism for emulsion inversion. (h) Schematic of hydroxyl-terminated nanosheet in basic solution and (i) deprotontation to form water and increase polar contribution to nanosheet surface energy.

concentration of H^+ is increased and the GO acts to reduce this by re-protonation of these functional groups, reducing surface energy and stability in solution to promote emulsification. As such, it was hypothesised that any functional groups present at the edges of pristine nanosheets would not be dissociated in solvent dispersions (to reduce polarity and improve surface energy matching) but could be deprotonated under at elevated pH, such as in emulsification with basic solution. In practise, using standard cycloketone dispersion and pH 13 KOH solution, emulsions are found to form as oil-in-water as shown in Figure 6.13, indicating that deprotonation induced is sufficient to increase the surface energy of the nanosheets above the threshold required to invert these emulsions, around 80 mJ/m^2. As shown this approach can be applied for graphene, MoS_2 and BN, suggesting some similarity in their edge functionalities and can even be used for surfactant-exfoliated nanosheets. This inversion can also be reconciled with the surface energy model in that dissociation of functional groups increases the polar contribution to the edge defect surface energy measured in [117]. A 30% increase in this value, for nanosheets of average size, would be sufficient to increase their surface energy above the threshold required for inversion.

These results emphasise the robustness of the framework developed here to understand and design functional nanosheet-stabilised emulsions. Further studies will be required to fully understand the influence of composition (surface energies, nanosheet size, surfactant, pH) on structure and subsequent influence of structure on functional properties, as these emulsions move towards applications.

Chapter 7

Thin films of MoS_2 nanosheets

The original objective of this thesis was to extend the Langmuir deposition technique, previously used for graphene [160], to other pristine nanosheets, specifically MoS_2. Alongside the "detours" of identifying NMP degradation and photoluminescence, modelling size selection and developing a framework for nanosheet-stabilised emulsification, the observation of the anomalously-high conductivity in MoS_2 nanosheet networks maintained interest in the potential of Langmuir films.

Pristine layered materials, even in the now-archetypcal subset of graphene, BN and MoS_2, span the full gamut of electronic properties; namely, conductor, insulator and semiconductor. Their potential for combination and application in thin film electronics is an area of significant research interest [124, 79, 45]. While solution-processed devices have recently been demonstrated with impressive functionality, their performance remains far behind single-flake devices fabricated from mechanically-cleaved or CVD materials [49]. Electronic transport in nanosheet networks is typically limited by inter-sheet junctions, resulting in low conductivities and mobilities compared with single-flake devices [79].

These effects are compounded by the difficulty in assembling densely-packed networks from liquid-exfoliated nanosheets at low film thickness. This is because traditional thin film deposition techniques (spray deposition, inkjet printing) are random overcoating processes where area coverage and thickness are inherently coupled. As such, it is not possible to increase area coverage without also increasing

film thickness. One consequence of this is that there are minimum thicknesses for connectivity and formation of a percolation network (associated with area coverage for percolation) and a further thickness threshold for the network conductivity to reach the maximum bulk-like, thickness-independent value [7, 11]. This effect is perhaps most evident for BN in printed capacitors where pinhole-free full-coverage films are only achieved at a thickness >1.5 µm [44]. Clearly, such disorder and porosity is likely to influence both critical thicknesses and functional properties in device structures and must be reduced to improve performance.

For (semi)conductors, the thickness required for bulk-like conductivity is typically in the range 50-200 nm for relatively uniform deposition (vacuum filtration [7], inkjet [11]) but can be greater than 1 µm for less uniform deposition (as in Chapter 6). This increases the film thickness required for a given conductance to thicknesses where it is not possible to electrostatically gate devices, hence recent studies of electrolytically-gated devices [79, 129]. Indeed, even if the semiconductor films could be assembled with sufficiently high conductivity and low thickness, devices would also require ultra-thin pinhole-free dielectric films for electrostatic gating.

An alternative to random overcoating techniques (inkjet, spray, filtration) is the interfacial assembly approach of Langmuir deposition. This is the technique of assembling thin films at the air/water interface, followed by "compression" into a dense-packed network and transfer onto substrate. This technique has previously been applied to a range of 2D materials [156, 157, 158, 159, 160, 161] but its potential for thin films of semiconducting nanosheets remains relatively unexplored. As such, this chapter develops a methodology for exfoliation and deposition of MoS_2, the prototypical 2D semiconductor with a view to preparation of thin and highly-conductive films for application as the active layers in solution-processed electronic devices.

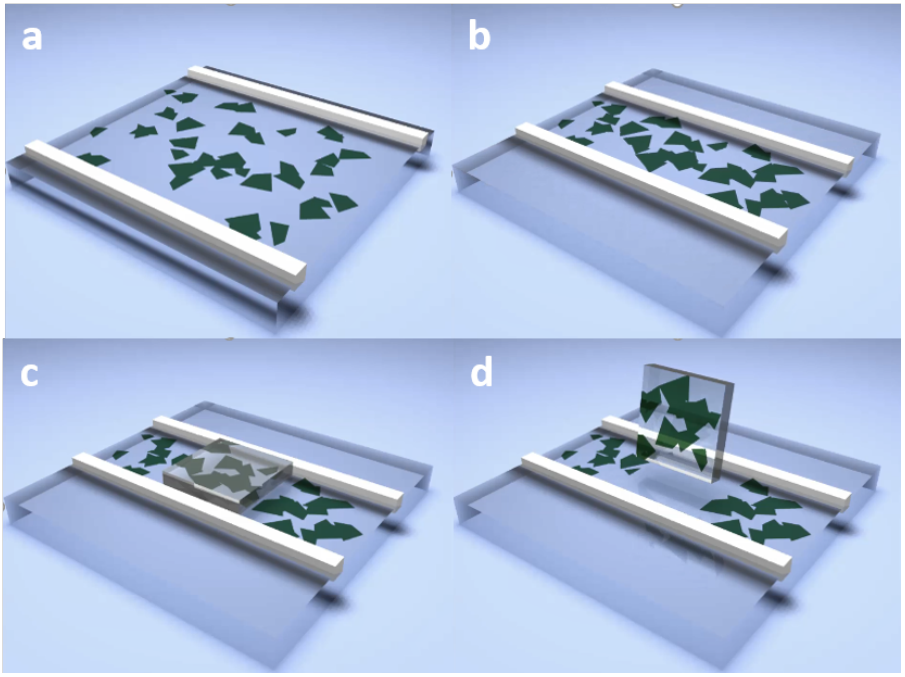

Figure 7.1: Schematic of Langmuir deposition of nanosheets; (a) spreading, (b) compression, (c) Langmuir-Schaefer horizonatal deposition and (d) deposited film.

7.1 Understanding solvent spreading

As for nanosheet-stabilised emulsions, solvent selection is an important aspect of Langmuir deposition where the carrier liquid is required to be a spreading solvent at the air/water interface, good for exfoliation and low boiling point. Spreading at the air/water interface, as with the dynamics of emulsion interfaces, is determined by the force balance at the three-phase boundary [190]. This air/water/solvent interface can be illustrated as a hemispherical droplet on the water surface with air/water and solvent/water interfacial tension opposing each other horizontally and the solvent/air interfacial tension at an angle inclined to the centre of the solvent droplet. The relative magnitudes of the interfacial tensions determine this contact angle and for solvents which this is less than 90°, the interfacial point will move outward, resulting in spreading of the solvent. This is described by Young's equation, which is usually used to characterise the contact angle of a liquid on a solid substrate, with the water acting as the planar subphase in this case.

$$\gamma_{aw} = \gamma_{sw} + \gamma_{sa} \cos \theta_c \tag{7.1}$$

Given the criterion that spreading solvents are those for which $\theta_c < 90°$ and therefore $\cos\theta_c > 0$, this can be rearranged to give an inequality on the interfacial tensions

$$\gamma_{aw} > \gamma_{sw} \tag{7.2}$$

However, this appears to be a trivial condition as the interfacial tension between air and water is, almost by definition, greater than that between air and the solvent in that all common solvents are intermediate in surface tension between air (∼0 mN/m) and water (∼72 mN/m). This is numerically consistent with both experimental measurements of interfacial tension and simple models of interfacial tension as a function of surface tension but incorrectly implies that all solvents will spread at the air/water interface. There are a number of low surface tension, low boiling point solvents (e.g. pentane, hexane, toluene) which do not spread at the air/water interface and instead pool at the surface. Some higher surface tension organics (e.g. toluene) do not spread and some lower surface tension organics do (e.g. acetone). These observations suggest that spreading is not solely determined by surface or interfacial tensions and that there is some chemical selectivity, with non-polar solvents comprising most of the non-spreading solvents. While these non-spreading solvents are not conventionally considered good solvents for the exfoliation and dispersion of 2D materials, a simple observation of spreading or non-spreading on a pristine water subphase does not account for solvents which may be borderline; which spread initially but cease to do under certain conditions, for example in the presence of a film or other species.

It is possible to formalise this understanding of the influence of solvent chemistry on spreading by using an interfacial tension model based on Hansen parameters. By taking an established model [194] correlating surface tension with Hansen parameters via molar volume, and noting that solubility in the Hansen formalism is determined by the component-wise differences between parameters, effective interfacial tensions γ_{sw} can be calculated which are related to the difference in chemical properties,

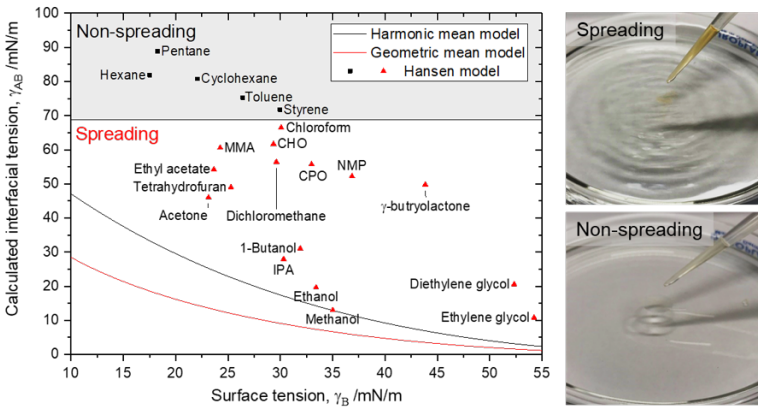

Figure 7.2: Solvent spreading based on Hansen parameter analysis, presented in [190].

allowing them to be greater than γ_{aw} and therefore non-spreading according to Equation 7.2. Interestingly, while the original surface tension-Hansen parameter model is not perfectly accurate ($\sim 3\%$ error) and the calculated interfacial tensions are not consistent with either experimental measurements or simple geometric or harmonic mean models, the calculated values of γ_{sw} correctly predict the spreading behaviour of all 21 solvents tested, as shown in Figure 7.2.

In addition, the difference $\gamma_{sw} - \gamma_{aw}$ gives a value for surface pressure (the reduction in surface tension of the water subphase, such as in the presence of an amphiphilic film) at which that solvent would cease to spread. By assembling a film of arachidic acid, with surface pressure-area "isotherm" shown in Figure 7.3, these maximum surface pressures can even be verified by compressing to increasing surface pressure and testing spreading at each, showing excellent agreement with the values predicted by the model. This result illustrates the robustness of this Hansen parameter model for spreading solvent identification and identifies a range of candidate solvents for Langmuir deposition of 2D materials. Importantly, however, the maximum spreading pressures are found to only apply for surface active films where the amphiphile acts to reduce the overall surface tension of the subphase (rather than contributing its own surface tension) and thereby reducing the threshold for spreading. While nanosheet films contribute to the surface pressure measured during Langmuir deposition, their particulate nature means that even in relatively

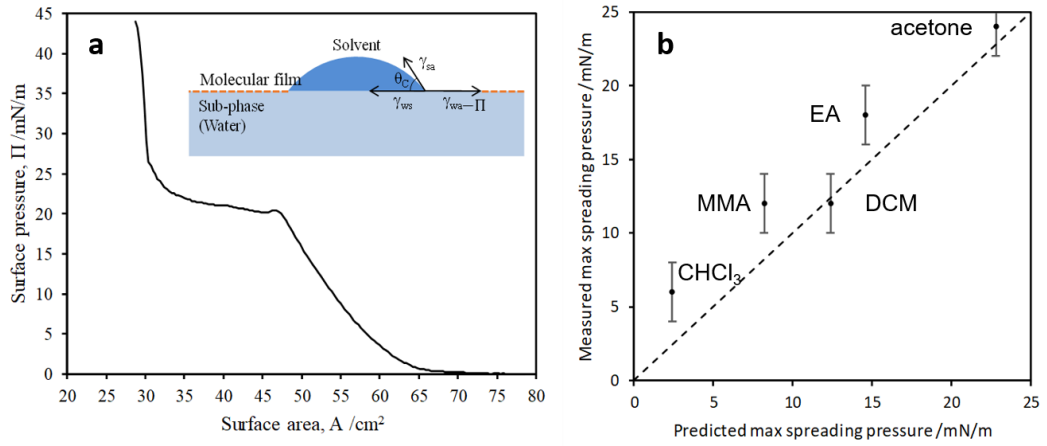

Figure 7.3: Spreading threshold analysis in presence of amphiphilic film. (a) Pressure-area isotherm for arachidic acid monolayer and (b) Maximum spreading pressure for a selection of solvents as a function of predicted maximum spreading pressure based on Figure 7.2.

dense films, a spreading droplet can part the film and effectively spread on the pristine water surface below. This facilitates the formation of dense films from a range of spreading solvents despite their susceptibility to non-spreading in the presence of traditional amphiphilic Langmuir films. As such, this model can be considered to capture the chemical physics of solvent spreading, where other models and even experimental values do not, and therefore be used a screening mechanism to ascertain whether previously unexplored solvents, which may have other properties desirable for Langmuir deposition, are likely to spread.

7.2 Langmuir deposition of MoS_2 films

The approach presented in the previous section for solvent selection was used here to identify a number of spreading solvents, in conjunction with Hansen parameter analysis to determine their suitability for exfoliation of layered materials, before experimental verification. Conventionally good exfoliating solvents are those which are well matched in surface energy and Hansen parameters to the layered materials. NMP has been well established as the solvent which gives the highest concentrations and degrees of exfoliation for liquid phase exfoliation of layered materials and has

been used for Langmuir deposition of graphene despite its high boiling point and other drawbacks detailed in Chapter 4. NMP has been used as a solvent for Langmuir deposition on both its own [159], relying on dissolution into the subphase, and following dilution with other lower boiling point spreading solvents [160] but this will still leave residue in the deposited films. Since Langmuir deposition (unlike other techniques) can be performed with relatively low concentration dispersions, it is possible to use solvents considered poorer for liquid exfoliation, which may also be lower boiling point and less susceptible to degradation, such as acetone [195]. In practise, it would be desirable to balance concentration (and degree of exfoliation) with boiling point to allow rapid deposition of well-exfoliated nanosheets into residue-free films. There are a number of solvents with low Hansen interaction radius ($<$6 $MPa^{1/2}$) and low boiling point, such as dichloromethane and acetone, but these are often coupled with poor surface tension matching, as illustrated in Figure 7.4, resulting in low concentrations with relatively poorly-exfoliated nanosheets. In fact, the only solvent in the bottom left quadrant of both Figure 7.4(b) and (c) with low surface tension mismatch, Hansen interaction distance and boiling point is cyclopentanone (CPO). The relatively low viscosity and high vapour pressure results in rapid spreading and evaporation and, coupled with its low toxicity, make CPO an ideal solvent for Langmuir deposition of MoS_2.

Langmuir deposition has been demonstrated with a range of 2D materials [156, 157, 158, 159, 160, 161, 162] but it has yet to be applied to deposit thin films of semiconducting nanosheets. In particular, in order to exploit their potential for thin films with bulk-like conductivity, it is necessary to achieve with high area coverage. Langmuir deposition troughs are typically capable of compression ratios of around 5, from a few hundred to tens of cm^2 samples, which means that the floating film must have area fraction of around 0.2 before compression.

This is typically monitored during deposition using surface pressure as a proxy for area coverage [160]. However, it is important to note that these dense films of nanosheets do not behave like amphiphilic films in terms of their self-interaction or

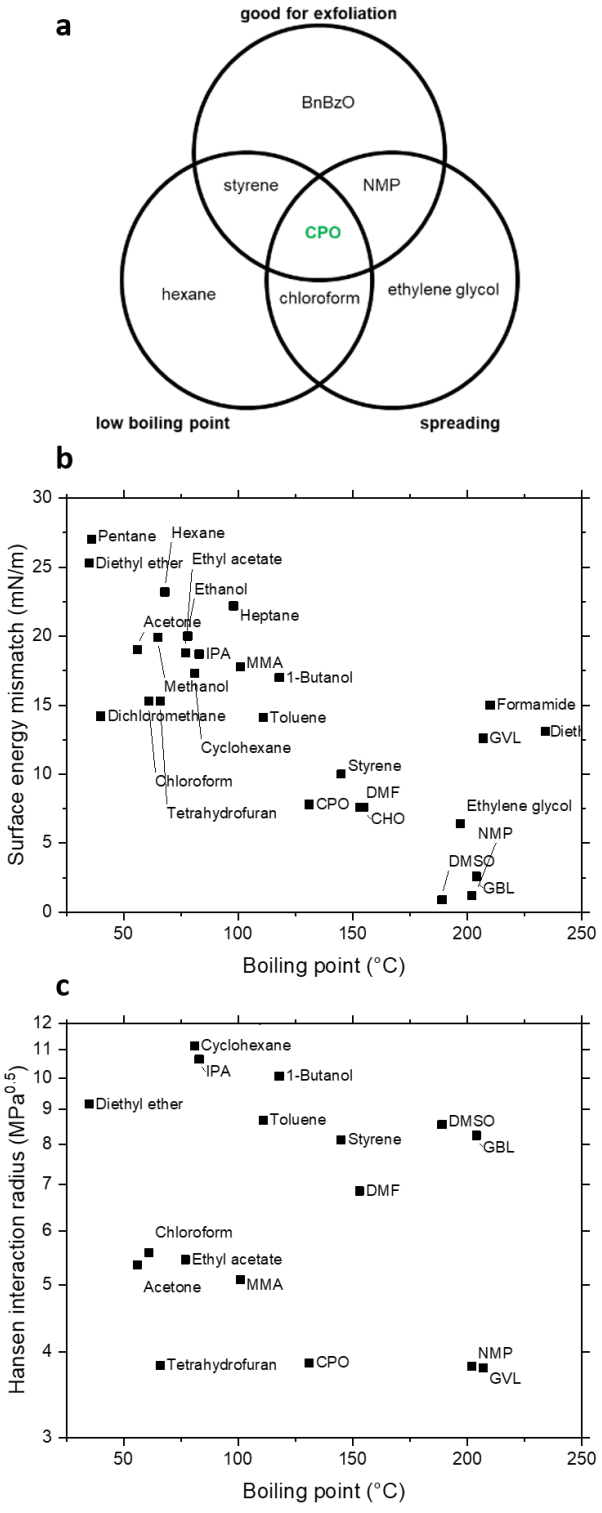

Figure 7.4: (a) Solvent selection Venn diagram for Langmuir deposition. (b) Surface energy mismatch and (c) Hansen interaction radius as a function of boiling point for a range of solvents.

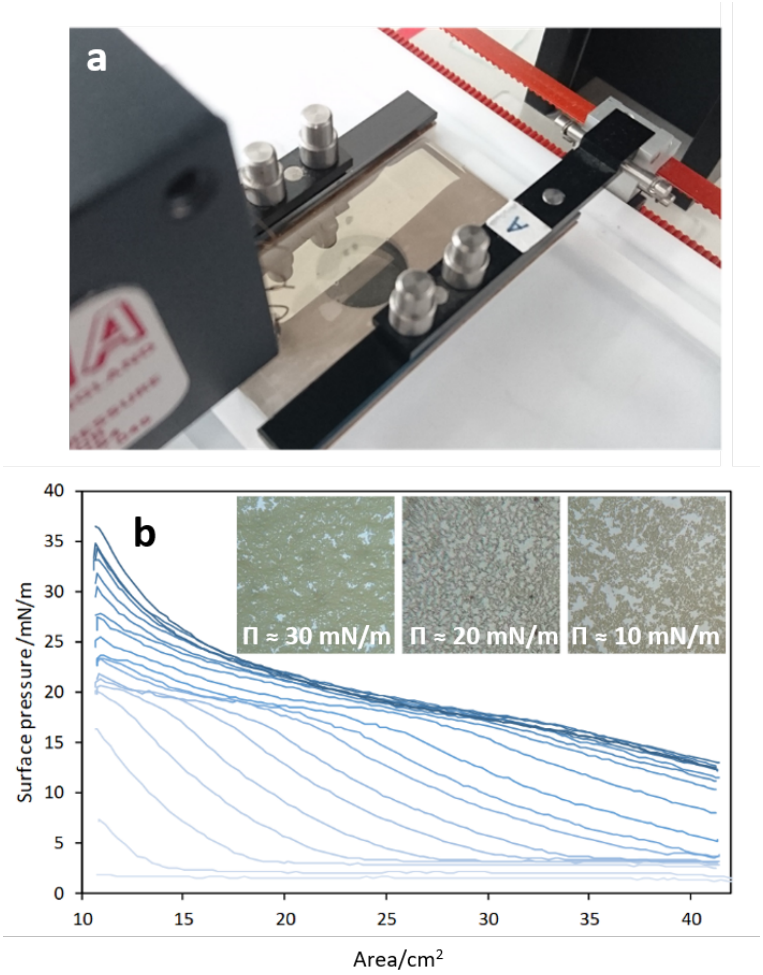

Figure 7.5: (a) Photograph and (b) pressure-area isotherm of MoS_2 film during repeated cycling and deposition. Inset: optical micrographs of film at different stages of compression.

surface pressure. Firstly, as mentioned above, amphiphiles are essentially surfactants, which reduce the surface tension of the water subphase rather than covering a fraction of the surface with a lower surface energy species. As such, amphiphiles in floating monolayers only interact when the area per molecule is decreased below their characteristic value, leading to well-defined gas-to-liquid and liquid-to-solid transitions in the pressure-area isotherm, as in Figure 7.3. By contrast, films of nanosheets are self-interacting even before compression; their particulate nature means that edges constitute an additional energetic contribution, a lower dimensional "linear tension", which is minimised when neighbouring nanosheets aggregate. It is also likely that there is a chemical contribution to this edge effect due to high-energy defect and functional groups present at nanosheet edges.

This results in the formation of "islands" of nanosheets during deposition, which can be several millimetres across and appear continuous under low magnification optical microscopy. The effect of these islands on the pressure-area isotherm during deposition and compression is to smooth the transitions between solid, liquid and gas phases of the films. It appears that the transitions are associated with the islands of nanosheets coming into contact and reaching full compression, as shown in Figure 7.5.

In addition, the rapid spreading and evaporation of the solvent is likely to cause these islands to form as turbostratically-restacked, rather than perfectly coplanar, nanosheets. This would result in a minimum film thickness correlated with the typical thickness of islands and their proportion in relation to individual nanosheets. In practise, if lower concentrations and volumes and slower deposition are used to attempt to form films of individual nanosheets, there is no measurable film conductivity even at high area coverage. This perhaps suggests that, even though very thin but dense films can be formed, there remains a critical thickness for bulk-like conductivity due to the need for charge transport perpendicular (and large nanosheet overlap area) to the basal plane to circumvent the issue of edge-edge hopping.

The formation of a monolayer of islands, as opposed to a monolayer of nanosheets, is evidenced by the structure of the deposited films. Atomic force microscopy (Figure 7.6 shows that they are densely-packed networks of nanosheets with area coverage >80 % and peak heights of around 150 nm, with the average height (film thickness) typically 20-50 nm. Further, scanning electron microscopy confirms this uniformity over length scales of hundreds of microns. This illustrates the potential of Langmuir deposition, above other techniques, to form films without significant area coverage-thickness correlation. The prospect of preparing such films at thicknesses up to an order of magnitude thinner than by inkjet but with comparable sheet resistance may facilitate their integration within thin film electronics.

Given the layer number dependence of the optoelectronic properties of MoS_2, it is important to consider how the degree of the exfoliation of the nanosheets in

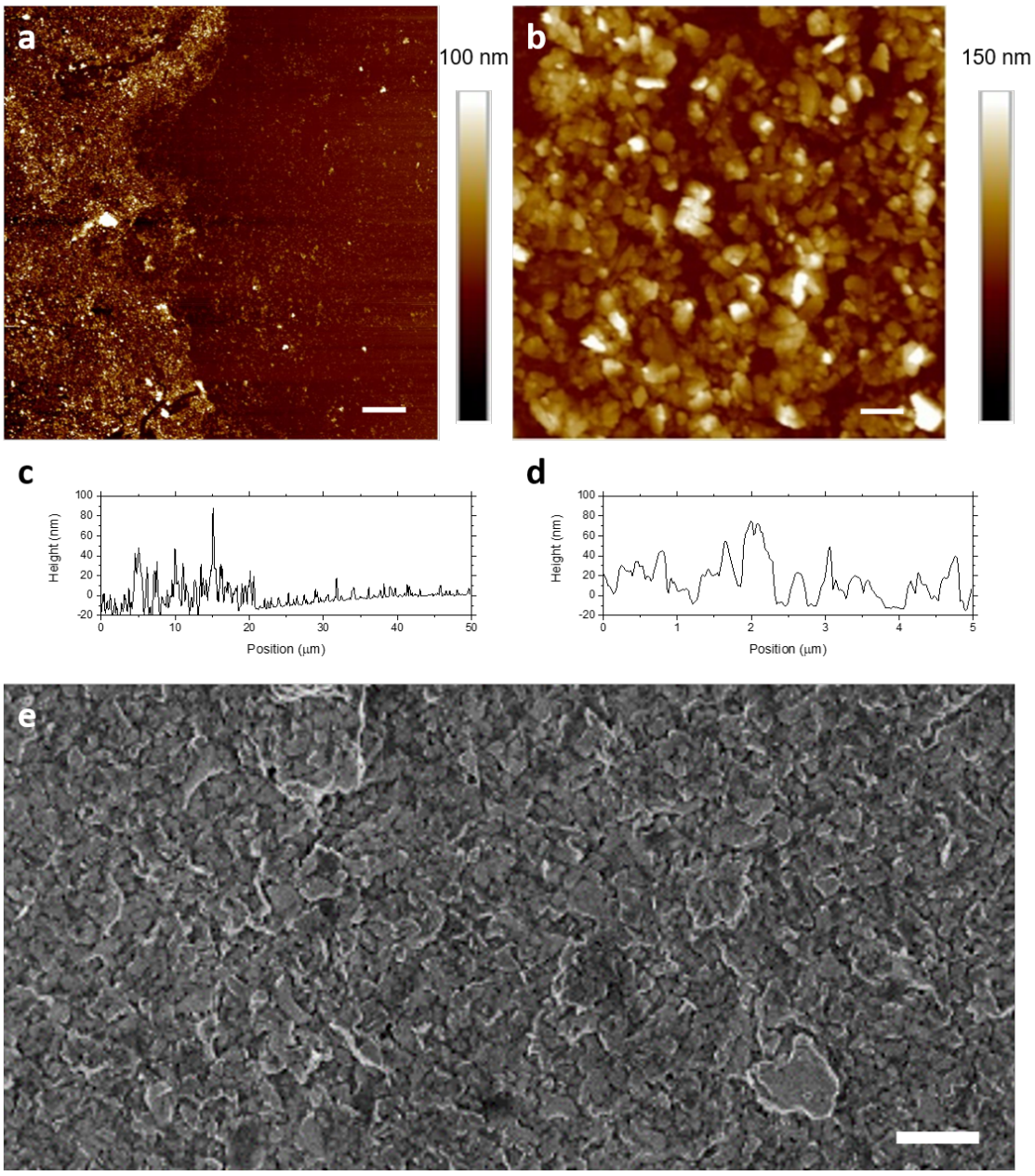

Figure 7.6: Atomic force micrographs of (a) film edge with scale bar 5 µm and (b) densely-packed region with scale bar 500 nm, with corresponding line sections (c) and (d) of middle row from each micrograph. (e) Scanning electron micrograph with scale bar 1 µm.

the films may influence subsequent device performance. The effect of the average layer number of a dispersion of nanosheets and of a deposited film thereof is not fully understood but it is generally acknowledged that greater degree of exfoliation allows for greater alignment in the film and that greater polydispersity due to smaller thinner nanosheets allows for improved packing. This results in charge transport predominantly parallel to the basal plane of the nanosheets, however smaller nanosheets result in a high density of inter-sheet junctions with smaller contact area (increased junction resistance), so nanosheet size and thickness distributions are likely to have an optimum for maximum film conductivity.

In addition to the network morphology and conductivity, MoS_2 nanosheets themselves are modified by the degree of exfoliation. Confinement effects in few-layer MoS_2 lead to the indirect band gap widening and becoming direct in the monolayer limit [53, 48]. This thickness dependence can be problematic for films with a broad distribution of few-layer nanosheets, where mismatched band gaps can act as charge traps and reduce device performance [79]. As such, an optimal degree of exfoliation for such devices might be to retain an *in situ* layer number that maximises transport properties but with no variation in band gap (perhaps around $\langle N \rangle$=6 layers). By contrast, other applications may require different optical properties and therefore layer number (perhaps even all-monolayer) and, as such, it is of interest to test the extent to which exfoliation can be retained in situ.

Langmuir films are a model system for such measurements because their semi-transparency (T $\sim$ 20–50%) allows the use of optical spectroscopy in transmission to determine layer number from well-established spectroscopic metrics [56]. Given that the monolayer transmittance of MoS_2 is around 85% [196], even the lowest transmittance Langmuir films have an area-averaged thickness of $<$10 monolayers. This does not account for reflectance or the influence of nanosheets at an angle to the incident beam but nevertheless gives an order-of-magnitude estimate in good agreement with the microscopy above. This also highlights that it would not be possible to make such measurements in films with thicknesses $>$1 µm, meaning that

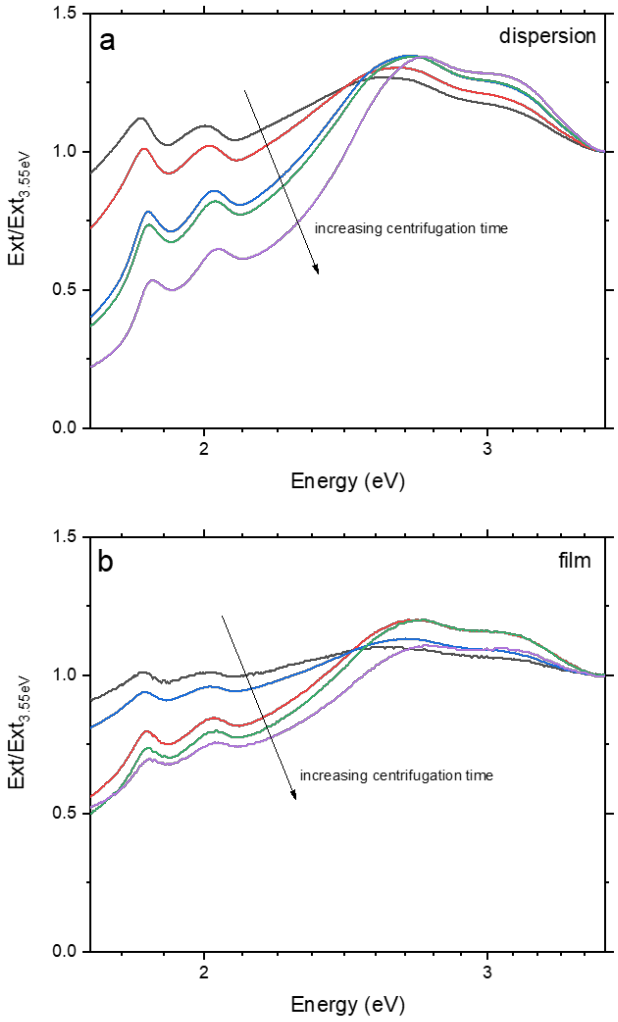

Figure 7.7: UV-visible extinction spectra (a) dispersions and (b) deposited Langmuir films of MoS_2, showing systematic shifts in excitonic features with centrifugation time.

Langmuir films are the only system where these optical and electrical measurements can be made on the same samples.

As such, the average layer number in the deposited film can be compared to that in dispersion to characterise the degree of exfoliation retained. Importantly this requires the nanosheets in dispersion to be below the ∼10-layer threshold for which spectroscopic metrics are sensitive to layer number. For these metrics, calibrated for surfactant-exfoliated nanosheets and those transferred into aqueous surfactant during liquid cascade centrifugation, this corresponds to A-exciton energies between 1.84 and 1.89 eV (675 and 660 nm respectively) for both dispersions and films.

However, when performing liquid cascade centrifugation on CPO-exfoliated samples, even allowing for viscosity and size effects as discussed in Chapter 5, the A-exciton features show meaningful shifts to energies as low as 1.82 eV (up to ∼680 nm, as shown in Figure 7.7), which would correspond to >20-layer nanosheets. In addition, A-exciton peaks are not observed at energies above 1.86 eV (below 668 nm), suggesting $\langle N \rangle > 5$, even for samples prepared under substantial centrifugation conditions (>10^5 $g$min). While this could be attributed to decreased few-layer population compared with surfactant-exfoliated dispersions, this does not account for the apparently increased sensitivity of A-exciton wavelength to >10-layer nanosheets [56].

By characterising the Langmuir films deposited from these narrow size distribution dispersions, any influence of the solvent will be reduced. As shown in Figure 7.7, the A-exciton wavelength range of the corresponding films does indeed blueshift, to energies greater than 1.83 eV, closer to the expected range for few-layer nanosheets. This shift suggests that the nanosheets in these Langmuir films exhibit a higher degree of exfoliation than those in the dispersion from which they were deposited, which is clearly physically unreasonable.

Instead, the net blueshift could be attributed to the removal of solvatochromic effects present in dispersion dominating over reaggregation of the nanosheets during deposition. This is consistent with the net redshift for the thinnest nanosheet dispersions after deposition with their high surface area providing a greater driving force for reaggregation. As such, a plot such as Figure 7.8(c), specifically whether points are above or below the line y=x, can be used to determine the net effects of solvatochromism (removal thereof) and reaggregation of during deposition.

In addition, these metrics are unlikely to remain calibrated to the point of being quantitative after deposition and solvatochromic effects are unlikely to be removed entirely. Nevertheless, the sensitivity of these spectroscopic features to size selection parameters suggests they are at least indicative of the nanosheet conditions in dispersion and film. In an attempt to quantify the influence of solvatochromic effects,

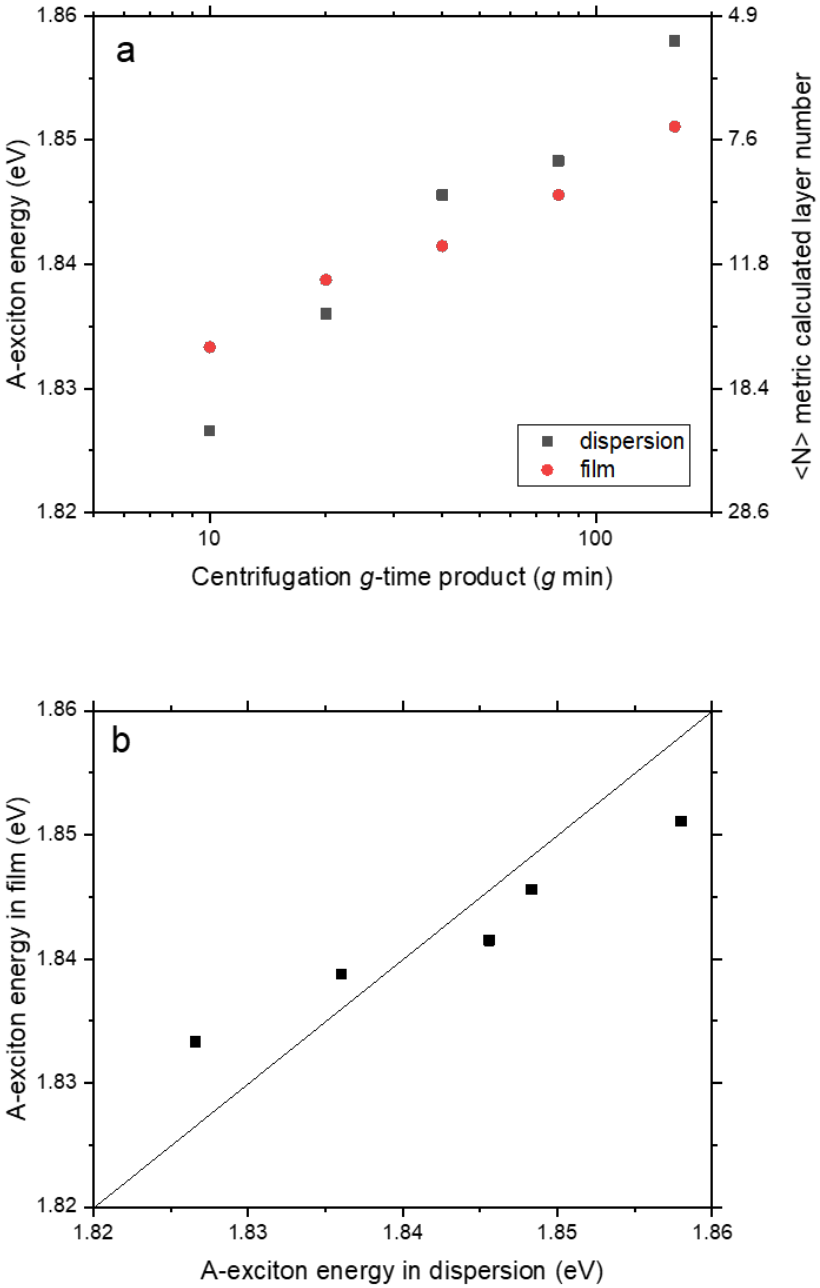

Figure 7.8: (a) MoS_2 A-exciton position as a function of centrifugation g-time product and (b) comparison between dispersion and film, showing some redshift for higher centrifugation time and blueshift for lower centrifugation time samples.

the $\langle N \rangle$ metric from [56] can be expressed in terms of energy;

$$\langle N \rangle = 2.3 \times 10^{36} e^{-44.16 E_A} \tag{7.3}$$

From this equation, it is clear that few-nm shifts which correspond to few-meV offsets can be expressed as an exponential prefactor to the original calculated layer number. Assuming that the metric is valid for the deposited films and that these therefore give a lower bound on the layer number for the dispersions, this approach could be used to "correct" the solvatochromic effect and determine the actual degree of exfoliation retained.

In studies of solvatochromism on mechanically-cleaved MoS_2, acetone (a ketone, like CPO) is found to redshift the PL emission either in terms of peak energy [197] or increasing the trion contribution [198]. Assuming a corresponding shift applies to the absorption peak and taking the ∼16 meV redshift observed in [197] as an estimate for that expected for CPO, the prefactor in the $\langle N \rangle$ metric would be 0.49. This would mean the values measured for the CPO dispersion are around double their true (solvatochromism-free) value and therefore all lower than the corresponding values of for the deposited films. In fact, this shift could be as low as 7 meV and still satify the requirement than $\langle N \rangle_{disp} < \langle N \rangle_{film}$, with all values in between suggesting varying degrees of aggregation are responsible for the shifts between dispersion and film, as shown in Figure 7.9.

It is also worth noting that the influence of restacking on spectroscopy of liquid-exfoliated nanosheets is poorly understood in general. It has been suggested that nanosheets films exhibit turbostratic restacking and this results in little influence on the spectroscopic properties (both optical and vibrational) relative to isolated the same nanosheets in dispersion [115]. If this is the case, it might be a more accurate interpretation that there is little to no reaggregation and all effects are solvatochromic with a balance between removal by depositing from dispersion (blue-shift) and retention by the presence of residual solvent (redshift). As such, it may be necessary to apply offsets to both the dispersion and film values. Doing so as a fitting

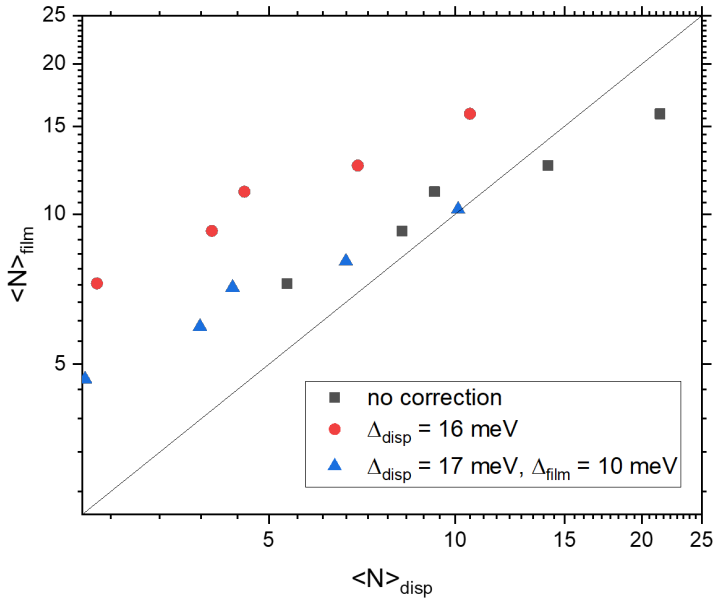

Figure 7.9: MoS_2 $\langle N \rangle$ metric calculated for film and dispersion with suggested solvatochromic corrections based on shifts observed in [197] and fitting to maximise agreement neglecting reaggregation effects.

exercise finds that shifts of 17 and 10 meV for the dispersions and films respectively give the best agreement between the two series, as shown in Figure 7.9. In reality however, the influence of the solvatochromism is likely to be more complicated and perhaps even sensitive to layer number given the potential for screening effects by the outermost layers. Nevertheless, this illustrates the potential of Langmuir films to study film formation through their optical properties, which will be an important area for future work.

7.3 Conductivity of films

Having characterised microstructural and optical properties of these MoS_2 films, it is important to consider how these correlate with the functional properties, namely electrical conductivity. The initial motivation for this study was the prospect of preparing films, which are both thin and highly conductive, i.e. without a thickness-dependent conductivity regime. It has been shown that the films have thicknesses of 20-50 nm at which thickness the conductivity of randomly-deposited MoS_2 films

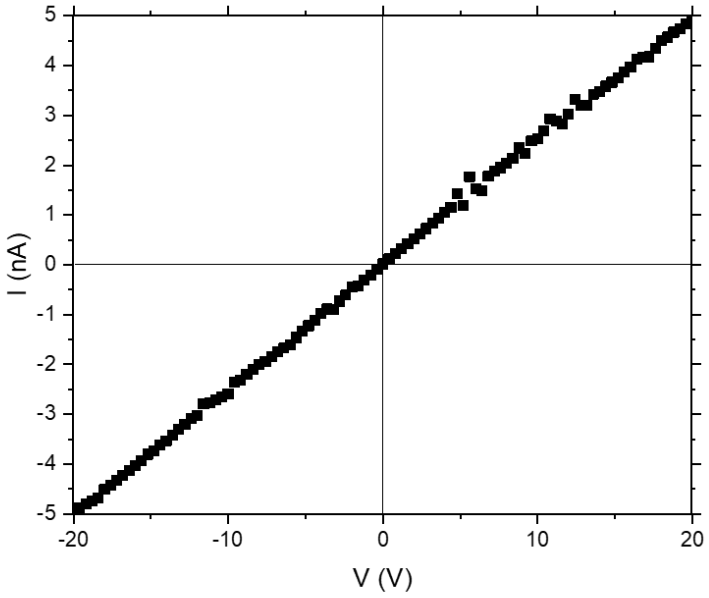

Figure 7.10: Representative I-V characteristic of MoS_2 Langmuir films.

would be $<10^{-6}$ S/m, with sheet resistances >1 TΩ/sq, which is impractical for any device operation. Indeed, even if it were possible to prepare films with bulk-like conductivity of $\sim 10^{-5}$ S/m, the sheet resistance would still be ∼100 GΩ/sq. Nevertheless, given that devices such as photodetectors and transistors have been demonstrated with films at comparable sheet resistance (conductivity $\sim 10^{-6}$ S/m and thickness ∼1 µm), ultra-thin Langmuir films have potential for application in ultra-thin devices where it may be possible to electrostatically gate the entire active layer.

In order to measure conductivity, Langmuir films, approaching full area coverage, were prepared as centimetre scale samples. Films were then deposited onto sputtered gold electrodes on PET, where the electrode adhesion is much better than on glass allowing part of the electrode area to be masked with Scotch tape, to allow direct contact after deposition. As shown in Figure 7.10, the I-V characteristics measured for these films are surprisingly ohmic, arguably even more so than previously-reported solution-processed films with good ohmic contacts [82, 83]. This indicates a reduction of the Schottky barrier that would be expected at the MoS_2-gold interface based

on conventional band bending arguments. This lack of a Schottky barrier has been observed previously in monolayer MoS_2 devices [49, 70, 71] with a reduced but non-zero barrier in multilayer MoS_2 [118, 80]. These effects have been attributed to Fermi level pinning close to the conduction band [76, 75, 77].

Most significantly, the sheet resistance of these samples is measured to be $\sim$1 GΩ/sq, as shown by the representative I-V characteristic in Figure 7.10. Given the film thicknesses of 20-50 nm (see Figure 7.6), this gives the conductivity as $\sim 10^{-3}$ S/m, two to three orders of magnitude higher than previously reported for MoS_2 nanosheet networks.

Given these results, it is interesting to compare these results with the conductivities previously reported for MoS_2 nanosheets. This is illustrated in Figure 7.11 as a plot of sheet resistance against film thickness for a range of samples deposited from different solvents and techniques. Parallel lines of constant conductivity show a group of results around 2×10^{-6} S/m for MoS_2 nanosheets deposited by a Langmuir-Blodgett-type assembly [120], vacuum filtration [83], inkjet printing [11, 130]. While all of these samples are prepared by exfoliation in NMP, the influence of the NMP in these films is likely to be minimised by the use of washing (during filtration) or solvent transfer (into fresh NMP or IPA). This "in-plane" conductivity is consistent with the three orders of magnitude anisotropy with respect to "out-of-plane" conductivity measured for IPA-exfoliated (NMP-free) MoS_2 [82].

In order to ascertain the origin of the high conductivity in the CPO-exfoliated MoS_2 Langmuir films described here, dispersions in NMP and aqueous surfactant solution were prepared using the same processing conditions. These were used to deposit films by solvent-compatible techniques; vacuum filtration for NMP and spray deposition for surfactant. Remarkably, these films also exhibit the same high conductivity as the Langmuir films ($\sim 2 \times 10^{-3}$ S/m), indicating that this anomalous performance is relatively independent of solvent choice, deposition technique and subsequent film structure. Instead, this suggests that the conductivity is the result of a modification of the inherent properties of the MoS_2 nanosheets themselves.

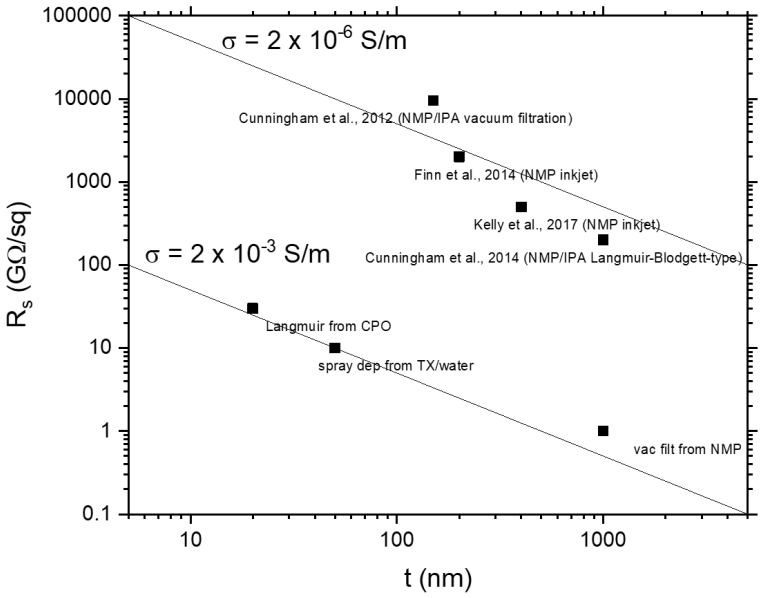

Figure 7.11: Sheet resistance as a function of thickness for a range of MoS_2 from literature and experiment.

As such, it is important to consider differences in processing between these nanosheet networks with conductivities of $\sim 10^{-3}$ S/m and those reported with conductivities of $\sim 10^{-6}$ S/m. Most significant is the choice of size selection procedures; where this work prioritised the selection of few-layer spectroscopically-interesting but correspondingly-smaller nanosheets, previous studies have either not size selected or preferentially removed these smaller thinner nanosheets. The reasons for this have been to prevent pinholes in vertical devices [82], negative photoconductivity [11, 83] and band gap mismatch [130].

If the the high conductivity of these films is also associated the size of the nanosheets, one might expect that they should also exhibit negative photoconductivity and/or charge trapping due to band gap mismatch. To investigate this, conductivity was measured under simulated solar illumination at a range of intensities. These films were indeed found to decrease in conductivity as a function of intensity to around half of their initial value at 1200 W/m^2. Interestingly, this dependence is not described by the power law relationship expected for a trap-limited system [82]. Instead, the functional form is better described by a quadratic form, which is not

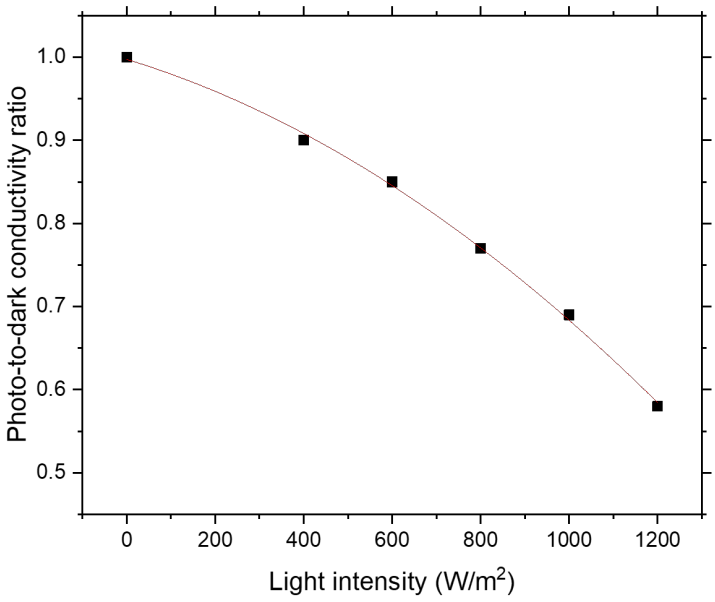

Figure 7.12: Negative photoconductivity of MoS_2 films as a function of light intensity, as previously acknowledged for networks of small nanosheets, attributed to Fermi level pinning, with quadratic fitting as a guide to the eye.

typical of photoconductivity or even negative photoconductivity and indicative of an alternative mechanism which requires further investigation.

These measurements confirm the films studied here have multiple characteristics which were acknowledged but not studied in detail previously; small nanosheets and negative photoconductivity [11, 83]. These can be correlated through other observations about networks formed from small nanosheets. These, by definition, have a high defect density due to number of edge sites relative to the number of basal plane sites. Edge sites are created by ultrasonic scission during exfoliation and can comprise functional groups, dangling bonds or vacancies. In MoS_2 in particular, sulfur vacancies are formed very readily [76, 75] and contribute a state very close to the conduction band. The effect of this is to pin the Fermi level close the conduction band edge, making MoS_2 an n-type semiconductor [77]. The extent to which this affects the conductivity is determined by the proximity and density of states of this dopant level. For states sufficiently close in energy to the conduction band, electrons can be thermally excited to result in higher carrier density and thereby conductivity.

The density of states is determined by dopant density, i.e. the number density of sulfur vacancies, and therefore has the potential to vary significantly with nanosheet size. Based on the edge-to-basal plane model presented in [56] and used in Chapter 6, the area fraction of edge sites (<2 nm from edge) can vary from 2% for 500 nm nanosheets to 20% for 50 nm nanosheets. A corresponding increase in the density of dopant states could explain the anomolously high conductivity observed in the films of small nanosheets studied here.

While this high conductivity was observed for relatively polydisperse single-centrifugation-step-selected samples, dispersion with systematically decreasing size and narrower distributions can be produced by liquid cascade centrifugation. A cascade was therefore performed to produce nanosheets with sizes ranging from much greater than those typically prepared for spectroscopic studies ($\langle N \rangle > 10$ and $\langle L \rangle \sim 500$ nm) to much smaller few-layer nanosheets ($\langle N \rangle < 5$ and $\langle L \rangle \sim 100$ nm). These nanosheets were spray deposited to >500 nm thickness to ensure bulk-like, thickness-independent conductivity and allow measurement by focus-encoded optical microscopy. The average nanosheet length was also measured by extinction spectroscopy using the metric developed in [56]. This allows correlation of the nanosheet size with film conductivity as shown in Figure 7.13.

This experiment illustrates that film conductivity does indeed exhibit a dependence on nanosheet length with larger nanosheets (>300 nm) exhibiting conductivities close to those previously reported for MoS_2 where smaller nanosheets are removed [82, 11, 83, 79, 130]. As nanosheet length is reduced below 300 nm, there appears to be a transition to the higher conductivity regime observed in this study. This is consistent with the increased effective dopant density due to the likely increase in prevalence of sulfur vacancies. The conductivity saturates for smaller nanosheets which may be due to the density of sulfur vacancies reaching an upper limit where further formation with decreasing nanosheet size is not possible. Alternatively, this saturation could be attributed to the increasing density of inter-sheet junction resistance in networks of smaller nanosheets. However, elucidation of the exact mechanisms

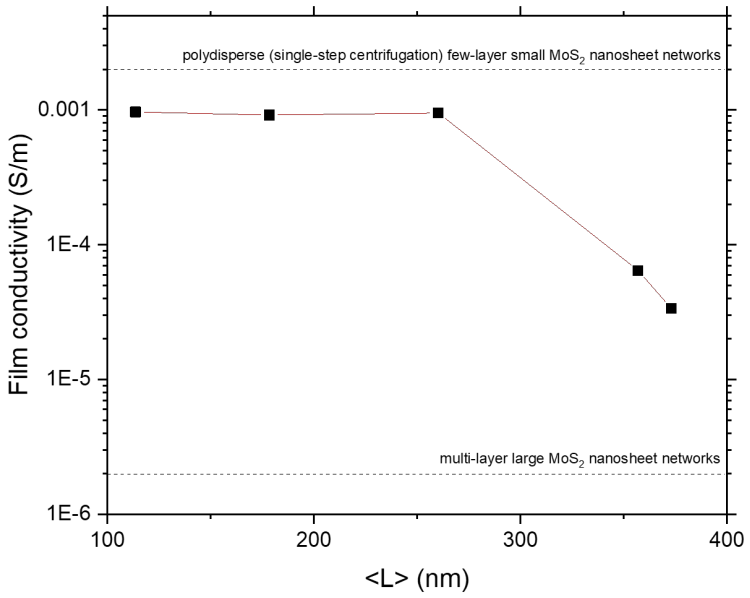

Figure 7.13: Conductivity of MoS_2 films as a function of average nanosheet length, indicating significant influence of doping due to nanosheet edges.

of both conductivity in nanosheet networks and doping by edge sulfur vacancies will require further work. In addition, it is unlikely that this high conductivity is solely due to increased carrier density, since this is unlikely to account for the three order of magnitude increase, and suggests that inter-nanosheet junctions may also be modified by the vacancies, potentially decreasing junction resistance and network mobility.

7.4 Conclusions

Langmuir deposition has been demonstrated to be a promising technique for preparation of ultra-thin and densely-packed nanosheet networks. Applications-driven solvent selection identifies that cycloketones provide a good balance of suitability for direct exfoliation, water immiscibility and low boiling point. Efforts to formalise the understanding of spreading and film formation have led to the development of a model which facilitates screening of potential solvents and reconciles inconsistencies in the existing models for this phenomenon.

Application of Langmuir deposition to MoS_2 illustrates that thin films of semiconducting nanosheets can be prepared at thicknesses below the thresholds for bulk-like conductivity associated with random overcoating techniques. The ultra-thin nature of these films allows them to be studied in transmission by optical extinction spectroscopy. The fundamental sensitivity of the A-exciton energy to degree of exfoliation enables analysis of the nanosheets in dispersion and on substrate, with deviations from established spectroscopic metrics attributed to solvatochromic effects. Further studies of such effects would investigate the effects of a range of solvents on films of deposited nanosheets where layer number could be correlated with statistical microscopy to calibrate metrics for solvatochromism.

In addition, despite the sub-100 nm thickness of these films, their conductivity is found to be thickness-independent, likely due to the high area coverage compared to spray- or inkjet-deposited films at similar thickness. Furthermore, the conductivity of these films is found to be around 10^{-3} S/m, which is two to three orders of magnitude higher than previously reported for similar networks. Perhaps more surprisingly, this high conductivity is independent of the exfoliating solvent or deposition process and instead a property of the relatively small few-layer nanosheets used here, which have been deliberately removed in previous studies [11, 83, 79]. This is consistent with the well-established influence of doping by sulfur vacancies in MoS_2 which results in Fermi level pinning close to the conduction band edge and n-type semiconduction. The combination of these ultra-thin films and high conductivity (and potentially mobility) opens up applications in optoelectronic devices such as electrostatically-gated transistors, which will be the focus of future work.

Chapter 8

Conclusions and future work

Liquid phase exfoliation is versatile technique to facilitate assembly of films, hybrids and composites of pristine few-layer 2D nanosheets and can be understood in terms of the surface energy and Hansen parameter matching of solvent to the layered material. However, the high concentrations typically required for applications means that *N*-methyl-2-pyrrolidone or aqueous surfactant solutions are often the dispersants of choice for film or composite formation.

The former has high boiling point and toxicity and, as shown in Chapter 4, is susceptible to degradation which results in polymeric residue adsorbed on nanosheet surfaces and photoluminescence which influences the optical properties of dispersions and potentially devices. Nevertheless, NMP has been demonstrated to be the most effective solvent for exfoliation of a range of 2D materials with impressive materials performance and functionality despite the potential for this to be influenced by degradation. While this can be minimised by solvent transfer or self-washing during vacuum filtration, it may be of interest for future work to consider how this degradation influences exfoliation and material performance to investigate whether liquid-exfoliated nanosheet networks can compete with conductivities etc. reported for other exfoliation processes in the absence of NMP residues [199].

Similar considerations must be made for surfactant-exfoliated nanosheets. Surfactants are typically used at concentrations of around 1:5 to that of the bulk layered material but, with exfoliation yields of order 1%, post-centrifugation supernatants

typically have surfactant:nanosheet ratios around 20:1 by mass. Such dispersions deposited in this study are, unsurprisingly, found to be non-conductive and this is likely the reason for the relative lack of studies of conductive networks based on surfactant-exfoliated nanosheets. While some of this surfactant is likely to be bound to nanosheets, a significant proportion will be free in solution and therefore superfluous. As with NMP, this can be remedied by solvent transfer, such as liquid cascade centrifugation, or filtration-type deposition techniques. In Chapters 6 and 7, proof-of-concept experiments are performed with surfactant exfoliation at low concentration (1:100 to bulk layered material) in an effort to minimise the amount in the final dispersion without the need for washing. Although this ratio is still likely to be around 1:1, films deposited from such dispersions exhibit conductivities similar to those for solvent-exfoliated nanosheets or washed films. Given that it would be desirable to develop water-based dispersions for applications, further work is needed to develop a protocol for applications-driven surfactant exfoliation. This would include comparison of exfoliation yield and bound vs free surfactant content as a function of initial surfactant concentration and Maron's titration experiments, previously performed for carbon nanotubes [200] to determine the surface coverage (and thereby mass ratio to the surfactant) of exfoliated nanosheets. Furthermore, the interfacial assembly techniques studied here represent a robust test for suitably-low surfactant content, which will be quantified in future studies.

With the above considerations for NMP- or surfactant-exfoliated nanosheet dispersions, it was decided that initial studies of interfacial assembly in this thesis would require alternative dispersants. In addition, the need for water immiscible solvents ideally with low boiling point resulted in the applications-driven solvent selection approach presented in Chapters 6 and 7. While the use of NMP and surfactant for exfoliation is typically justified based on surface energy matching and electrostatic stabilisation respectively, there is little quantitative understanding of how good or bad alternative solvents can be and how to standardise processing to optimise their suitability. Chapter 5 illustrates the influence of viscosity on

both exfoliation and centrifugation for a range of solvents, highlighting the need for adjusted processing parameters to allow fair comparison or optimisation of unconventional solvents. This understanding is used to develop a size selection model which also accounts for aspect ratio effects on the centrifugation. This simple model facilitates estimation of appropriate centrifugation parameters for any given material, solvent and desired nanosheet size and thickness. Calibration of the model is required in order for it be fully quantitative but it is hoped that further understanding of nanosheet aspect ratios and distributions can be developed to make the model fully predictive. In addition, future work will seek to verify both aspect ratio and viscosity effects by applying the model to a range of solvents to quantify how good or bad these "poor" exfoliating solvent actually are.

In practise, it is found that cyclopentanone (CPO) and cyclohexanone (CHO) are two unconventional solvents which enable exfoliation of MoS_2 and graphene, respectively, for the interfacial assembly approaches studied in this thesis. Specifically, the ability to prepare few-layer nanosheets at reasonable concentration in water-immiscible solvents allows the preparation of nanosheet-stabilised emulsions. These emulsions represent previously-unexplored assemblies of pristine nanosheets with the potential for applications such as high-loading inks, conductive composites, electromechanical sensors, energy storage materials and optoelectronic devices. By stabilising microscale liquid droplets with nanoscale thin films, these emulsions can be assembled into macroscopic structures at nanosheet volume fractions as low as 10^{-5} with conductivities as high as 10^{-4} S/m, comparable to randomly-assembled nanosheet polymer composites at much higher loadings [10]. In fact, such emulsions represent the lowest loading nanosheet-based conducting networks ever reported. Alternatively, the disordered restacking of thicker interfacial films allows formation of high-loading energetically-stable emulsions for applications as inks, which facilitate coffee-ring-free manual deposition of films with conductivities comparable to those for the deposited by other techniques. Optimisation of concentrations and compatibility for inkjet printing will require further studies of the influence of droplet

size, specifically on the rheology of emulsion inks.

Future work will focus on expanding the applications of these nanosheet-stabilised emulsions by seeking to maintain highly-exfoliated ultra-thin films in systems with compositions which facilitate formation of composites or hybrid systems for the aforementioned applications. In addition, emulsification of systems with a range of oil and water phases has enabled development of a model for emulsion orientation based on surface energies of the liquids and nanosheets. By combining simplified spreading coefficient criteria and mathematical approximations for interfacial energies, an emulsion equation has been derived which describes the threshold for inversion between water-in-oil and oil-in-water emulsions as a function of the nanosheet surface energy. This correctly describes all observed phenomenology with a nanosheet surface energy consistent with that inferred from exfoliating solvent studies or measured by inverse gas chromatography. As such, this emulsion equation is a powerful tool for design of nanosheet-stabilised emulsions and understanding of the properties of the nanosheets themselves. Nanosheet size is a parameter of interest for future studies with the potential to control surface energy and thereby emulsion orientation in suitably small or large populations. The influence of nanosheet edges is further illustrated by the demonstration of emulsion inversion in the presence of hydroxide ions in basic conditions. This is attributed to deprotonation of hydroxyl groups at graphene edges, increasing the polar contribution to the nanosheet surface energy and therefore inverting the emulsion. Perhaps surprisingly, this approach also inverts the orientation of MoS_2- and BN-stabilised emulsions, suggesting the presence of similar edge groups which can be deprotonated to raise surface energy. These could be S-H (thiol) and N-H (amine) groups respectively; verification and manipulation of this previously-unacknowledged edge functionality of liquid-exfoliated nanosheets is a potential area for future work.

Finally, Chapter 7 presents a study of Langmuir films of liquid-exfoliated nanosheets assembled at the air/water interface with a view to preparing ultra-thin densely-packed films of MoS_2 for optoelectronic device applications. Langmuir deposition,

as an interfacial assembly technique, facilitates formation of a films with nanoscale thickness which can be compressed into densely-packed networks, negating the thickness-dependent conductivity regime which places a lower bound on the thickness of films deposited by other techniques, resulting in the need for electrolytic-gating in nanosheet network devices [79, 129]. Chapter 7 demonstrates that it is possible to prepare conductive Langmuir films with thicknesses below 100 nm owing to their high area coverage. In addition, it is possible to study the optical properties of these ultra-thin nanosheet networks with UV-visible extinction spectroscopy in transmission. Measurements of the CPO dispersions find that the A-exciton is shifted to a lower energy range than would be expected for these nanosheets, with meaningful shifts at energies well beyond the bulk-like threshold [56]. Langmuir deposition from these dispersions results in films with a range of A-exciton energies blueshifted from the dispersions, which would conventionally indicate a higher degree of exfoliation. Instead, this is attributed to solvatochromic effects in the CPO dispersions which are to some extent removed after deposition. These solvent effects, specifically their influence on spectroscopic metrics for liquid-exfoliated nanosheets, will be studied in future work, to allow their use for the wide range of solvents required for interfacial assembly and other techniques.

Most significantly, while these films are around 100 times thinner than MoS_2 nanosheet networks reported in the literature, their sheet resistances are comparable, if not lower, indicating their conductivity is at least 100 times higher. In addition, these high conductivities are observed for nansoheets prepared under the same processing conditions in NMP and surfactant and deposited by vacuum filtration and spray deposition, respectively, suggesting the effect to be independent of dispersant or deposition technique. Instead, it is attributed to the use of small few-layer nanosheets deposited here, which are removed in previous studies to prevent pinholes, charge trapping due to band gap mismatch, and negative photoconductivity. Interestingly, negative photoconductivity is observed in the films studied here and is consistent with the two-level system expected for MoS_2 with edge sulfur vacancies. These

prevalent defects result in pinning of the Fermi level close the conduction band edge and it is suggested that these small nanosheets are highly doped due to the increased dopant density. Liquid cascade centrifugation is used to prepare size-selected samples for which the film conductivity shows a sharp transition between 10^{-5} S/m and 10^{-3} S/m as nanosheet size is reduced below 400 nm. While doping due to edge sulfur vacancies increases the carrier density, it is unlikely that it is solely responsible for the three order of magnitude increase in conductivity. As such, it it possible that the nature of the inter-nanosheet junctions is also modified by these vacancies, acting to increase network mobility and thereby conductivity. If so, this further enhances the potential of small MoS_2 nanosheet networks prepared as ultra-thin Langmuir films for electrostatically-gated transistors. In order to explore this application, future work will focus on thorough photoconductivity and field-effect measurements of these networks to characterise and understand device performance. On a more fundamental level, these networks are a novel system where smaller nanosheets, which typically results in reduced junction area and increased inter-nanosheet resistance, have higher network conductivity. Understanding the relative influence of modifying nanosheet size and inter-nanosheet junctions in this and other systems will require a model for transport in these networks. It is hoped that by studying graphene a model system without nanosheet size effects, this understanding can be developed and applied to improve the applications potential of nanosheet networks whether in films, composites or emulsions.

Bibliography

[1] G. Binnig and H. Rohrer. Scanning tunneling microscopy. *Surface Science*, 126(1):236–244, March 1983. 1

[2] G. Binnig, C. F. Quate, and Ch. Gerber. Atomic Force Microscope. *Physical Review Letters*, 56(9):930–933, March 1986. 1

[3] D. M. Eigler and E. K. Schweizer. Positioning single atoms with a scanning tunnelling microscope. *Nature*, 344(6266):524, April 1990. 1

[4] H. W. Kroto, J. R. Heath, S. C. O'Brien, R. F. Curl, and R. E. Smalley. C 60 : Buckminsterfullerene. *Nature*, 318(6042):162, November 1985. 1

[5] Sumio Iijima. Helical microtubules of graphitic carbon. *Nature*, 354(6348):56, November 1991. 1

[6] K. S. Novoselov, A. K. Geim, S. V. Morozov, D. Jiang, Y. Zhang, S. V. Dubonos, I. V. Grigorieva, and A. A. Firsov. Electric Field Effect in Atomically Thin Carbon Films. *Science*, 306(5696):666–669, October 2004. 2, 3, 7, 9

[7] S. De, P.J. King, P.E. Lyons, U. Khan, and J.N. Coleman. Size effects and the problem with percolation in nanostructured transparent conductors. *ACS Nano*, 4(12):7064–7072, 2010. 2, 23, 26, 71, 93, 100

[8] Sukanta De and Jonathan N. Coleman. Are There Fundamental Limitations on the Sheet Resistance and Transmittance of Thin Graphene Films? *ACS Nano*, 4(5):2713–2720, May 2010. 3, 10, 11, 23

[9] A. Celzard, J. F. Marêché, G. Furdin, and S. Puricelli. Electrical conductivity of anisotropic expanded graphite-based monoliths. *Journal of Physics D: Applied Physics*, 33(23):3094–3101, November 2000. 3, 8, 10

[10] A. J. Marsden, D. G. Papageorgiou, C. Vallés, A. Liscio, V. Palermo, M. A. Bissett, R. J. Young, and I. A. Kinloch. Electrical percolation in graphene–polymer composites. *2D Materials*, 5(3):032003, 2018. 3, 10, 11, 24, 71, 81, 125

[11] David J. Finn, Mustafa Lotya, Graeme Cunningham, Ronan J. Smith, David McCloskey, John F. Donegan, and Jonathan N. Coleman. Inkjet deposition of liquid-exfoliated graphene and MoS2 nanosheets for printed device applications. *Journal of Materials Chemistry C*, 2(5):925–932, January 2014. 3, 11, 23, 24, 26, 54, 93, 100, 117, 118, 119, 120, 122

[12] Alexander A. Balandin, Suchismita Ghosh, Wenzhong Bao, Irene Calizo, Desalegne Teweldebrhan, Feng Miao, and Chun Ning Lau. Superior Thermal Conductivity of Single-Layer Graphene. *Nano Letters*, 8(3):902–907, March 2008. 3

[13] Changgu Lee, Xiaoding Wei, Jeffrey W. Kysar, and James Hone. Measurement of the Elastic Properties and Intrinsic Strength of Monolayer Graphene. *Science*, 321(5887):385–388, July 2008. 3, 8

[14] Yenny Hernandez, Valeria Nicolosi, Mustafa Lotya, Fiona M. Blighe, Zhenyu Sun, Sukanta De, I. T. McGovern, Brendan Holland, Michele Byrne, Yurii K. Gun'Ko, John J. Boland, Peter Niraj, Georg Duesberg, Satheesh Krishnamurthy, Robbie Goodhue, John Hutchison, Vittorio Scardaci, Andrea C. Ferrari, and Jonathan N. Coleman. High-yield production of graphene by liquid-phase exfoliation of graphite. *Nature Nanotechnology*, 3(9):563–568, September 2008. 4, 10, 19, 20, 21, 22, 23, 37, 38, 48, 54, 56, 84

[15] Jonathan N. Coleman, Mustafa Lotya, Arlene O'Neill, Shane D. Bergin, Paul J. King, Umar Khan, Karen Young, Alexandre Gaucher, Sukanta De, Ronan J.

Smith, Igor V. Shvets, Sunil K. Arora, George Stanton, Hye-Young Kim, Kangho Lee, Gyu Tae Kim, Georg S. Duesberg, Toby Hallam, John J. Boland, Jing Jing Wang, John F. Donegan, Jaime C. Grunlan, Gregory Moriarty, Aleksey Shmeliov, Rebecca J. Nicholls, James M. Perkins, Eleanor M. Grieveson, Koenraad Theuwissen, David W. McComb, Peter D. Nellist, and Valeria Nicolosi. Two-Dimensional Nanosheets Produced by Liquid Exfoliation of Layered Materials. *Science*, 331(6017):568–571, February 2011. 4, 19, 20, 21, 22, 23, 38, 53, 54, 56

[16] Jaemyung Kim, Laura J. Cote, Franklin Kim, Wa Yuan, Kenneth R. Shull, and Jiaxing Huang. Graphene Oxide Sheets at Interfaces. *Journal of the American Chemical Society*, 132(23):8180–8186, June 2010. 4

[17] A. K. Geim. Graphene: Status and Prospects. *Science*, 324(5934):1530–1534, June 2009. 6

[18] K. S. Novoselov, D. Jiang, F. Schedin, T. J. Booth, V. V. Khotkevich, S. V. Morozov, and A. K. Geim. Two-dimensional atomic crystals. *Proceedings of the National Academy of Sciences of the United States of America*, 102(30):10451–10453, July 2005. 6

[19] Andrea C. Ferrari, Francesco Bonaccorso, Vladimir Fal'ko, Konstantin S. Novoselov, Stephan Roche, Peter Bøggild, Stefano Borini, Frank H. L. Koppens, Vincenzo Palermo, Nicola Pugno, José A. Garrido, Roman Sordan, Alberto Bianco, Laura Ballerini, Maurizio Prato, Elefterios Lidorikis, Jani Kivioja, Claudio Marinelli, Tapani Ryhänen, Alberto Morpurgo, Jonathan N. Coleman, Valeria Nicolosi, Luigi Colombo, Albert Fert, Mar Garcia-Hernandez, Adrian Bachtold, Grégory F. Schneider, Francisco Guinea, Cees Dekker, Matteo Barbone, Zhipei Sun, Costas Galiotis, Alexander N. Grigorenko, Gerasimos Konstantatos, Andras Kis, Mikhail Katsnelson, Lieven Vandersypen, Annick Loiseau, Vittorio Morandi, Daniel Neumaier, Emanuele Treossi, Vittorio Pellegrini, Marco Polini, Alessandro Tredicucci, Gareth M. Williams, Byung Hee

Hong, Jong-Hyun Ahn, Jong Min Kim, Herbert Zirath, Bart J. van Wees, Herre van der Zant, Luigi Occhipinti, Andrea Di Matteo, Ian A. Kinloch, Thomas Seyller, Etienne Quesnel, Xinliang Feng, Ken Teo, Nalin Rupesinghe, Pertti Hakonen, Simon R. T. Neil, Quentin Tannock, Tomas Löfwander, and Jari Kinaret. Science and technology roadmap for graphene, related two-dimensional crystals, and hybrid systems. *Nanoscale*, 7(11):4598–4810, March 2015. 6, 10, 17

[20] A. H. Castro Neto, F. Guinea, N. M. R. Peres, K. S. Novoselov, and A. K. Geim. The electronic properties of graphene. *Reviews of Modern Physics*, 81(1):109–162, January 2009. 7, 8, 9, 10

[21] A. K. Geim and K. S. Novoselov. The rise of graphene. *Nature Materials*, 6(3):183–191, March 2007. 7, 9

[22] Jamie H. Warner, Franziska Schaffel, Mark Rummeli, and Alicja Bachmatiuk. *Graphene: Fundamentals and emergent applications*. Elsevier, Amsterdam, January 2013. 8

[23] K. S. Novoselov, D. Jiang, F. Schedin, T. J. Booth, V. V. Khotkevich, S. V. Morozov, and A. K. Geim. Two-dimensional atomic crystals. *Proceedings of the National Academy of Sciences*, 102(30):10451–10453, July 2005. 8, 13

[24] Jian-Hao Chen, Chaun Jang, Shudong Xiao, Masa Ishigami, and Michael S. Fuhrer. Intrinsic and extrinsic performance limits of graphene devices on SiO_2. *Nature Nanotechnology*, 3(4):206–209, April 2008. 8

[25] Frank Schwierz. Graphene transistors. *Nature Nanotechnology*, 5(7):487–496, July 2010. 8

[26] K. I. Bolotin, K. J. Sikes, Z. Jiang, M. Klima, G. Fudenberg, J. Hone, P. Kim, and H. L. Stormer. Ultrahigh electron mobility in suspended graphene. *Solid State Communications*, 146(9):351–355, June 2008. 9

[27] Yuanbo Zhang, Tsung-Ta Tang, Caglar Girit, Zhao Hao, Michael C. Martin, Alex Zettl, Michael F. Crommie, Y. Ron Shen, and Feng Wang. Direct observation of a widely tunable bandgap in bilayer graphene. *Nature*, 459(7248):820–823, June 2009. 9

[28] Wenjuan Zhu, Vasili Perebeinos, Marcus Freitag, and Phaedon Avouris. Carrier scattering, mobilities, and electrostatic potential in monolayer, bilayer, and trilayer graphene. *Physical Review B*, 80(23):235402, December 2009. 10

[29] Kosuke Nagashio, Tomonori Nishimura, Koji Kita, and Akira Toriumi. Mobility Variations in Mono- and Multi-Layer Graphene Films. *Applied Physics Express*, 2(2):025003, January 2009. 10

[30] H. M. Wang, Y. H. Wu, Z. H. Ni, and Z. X. Shen. Electronic transport and layer engineering in multilayer graphene structures. *Applied Physics Letters*, 92(5):053504, February 2008. 10

[31] R. R. Nair, P. Blake, A. N. Grigorenko, K. S. Novoselov, T. J. Booth, T. Stauber, N. M. R. Peres, and A. K. Geim. Fine Structure Constant Defines Visual Transparency of Graphene. *Science*, 320(5881):1308–1308, June 2008. 10

[32] Aiping Yu, Isaac Roes, Aaron Davies, and Zhongwei Chen. Ultrathin, transparent, and flexible graphene films for supercapacitor application. *Applied Physics Letters*, 96(25):253105, June 2010. 10, 71

[33] Suchismita Ghosh, Wenzhong Bao, Denis L. Nika, Samia Subrina, Evghenii P. Pokatilov, Chun Ning Lau, and Alexander A. Balandin. Dimensional crossover of thermal transport in few-layer graphene. *Nature Materials*, 9(7):555–558, July 2010. 10

[34] M. Poot and H. S. J. van der Zant. Nanomechanical properties of few-layer graphene membranes. *Applied Physics Letters*, 92(6):063111, February 2008. 10

[35] Sasha Stankovich, Dmitriy A. Dikin, Geoffrey H. B. Dommett, Kevin M. Kohlhaas, Eric J. Zimney, Eric A. Stach, Richard D. Piner, SonBinh T. Nguyen, and Rodney S. Ruoff. Graphene-based composite materials. *Nature*, 442(7100):282, July 2006. 10

[36] Felice Torrisi and Jonathan N. Coleman. Electrifying inks with 2d materials. *Nature Nanotechnology*, 9(10):738–739, October 2014. 11

[37] D. Pacilé, J. C. Meyer, Ç. Ö. Girit, and A. Zettl. The two-dimensional phase of boron nitride: Few-atomic-layer sheets and suspended membranes. *Applied Physics Letters*, 92(13):133107, March 2008. 11

[38] Dmitri Golberg, Yoshio Bando, Yang Huang, Takeshi Terao, Masanori Mitome, Chengchun Tang, and Chunyi Zhi. Boron Nitride Nanotubes and Nanosheets. *ACS Nano*, 4(6):2979–2993, June 2010. 11

[39] Haiqing Zhou, Jixin Zhu, Zheng Liu, Zheng Yan, Xiujun Fan, Jian Lin, Gunuk Wang, Qingyu Yan, Ting Yu, Pulickel M. Ajayan, and James M. Tour. High thermal conductivity of suspended few-layer hexagonal boron nitride sheets. *Nano Research*, 7(8):1232–1240, August 2014. 11

[40] Aleksey Falin, Qiran Cai, Elton J. G. Santos, Declan Scullion, Dong Qian, Rui Zhang, Zhi Yang, Shaoming Huang, Kenji Watanabe, Takashi Taniguchi, Matthew R. Barnett, Ying Chen, Rodney S. Ruoff, and Lu Hua Li. Mechanical properties of atomically thin boron nitride and the role of interlayer interactions. *Nature Communications*, 8:15815, June 2017. 11

[41] Li Song, Lijie Ci, Hao Lu, Pavel B. Sorokin, Chuanhong Jin, Jie Ni, Alexander G. Kvashnin, Dmitry G. Kvashnin, Jun Lou, Boris I. Yakobson, and Pulickel M. Ajayan. Large Scale Growth and Characterization of Atomic Hexagonal Boron Nitride Layers. *Nano Letters*, 10(8):3209–3215, August 2010. 11

[42] C. R. Dean, A. F. Young, I. Meric, C. Lee, L. Wang, S. Sorgenfrei, K. Watanabe, T. Taniguchi, P. Kim, K. L. Shepard, and J. Hone. Boron nitride substrates

for high-quality graphene electronics. *Nature Nanotechnology*, 5(10):722–726, October 2010. 12

[43] Gang Shi, Yuranan Hanlumyuang, Zheng Liu, Yongji Gong, Weilu Gao, Bo Li, Junichiro Kono, Jun Lou, Robert Vajtai, Pradeep Sharma, and Pulickel M. Ajayan. Boron Nitride–Graphene Nanocapacitor and the Origins of Anomalous Size-Dependent Increase of Capacitance. *Nano Letters*, 14(4):1739–1744, April 2014. 12

[44] Adam G. Kelly, David Finn, Andrew Harvey, Toby Hallam, and Jonathan N. Coleman. All-printed capacitors from graphene-BN-graphene nanosheet heterostructures. *Applied Physics Letters*, 109(2):023107, July 2016. 12, 23, 24, 100

[45] Robyn Worsley, Lorenzo Pimpolari, Daryl McManus, Ning Ge, Robert Ionescu, Jarrid A. Wittkopf, Adriana Alieva, Giovanni Basso, Massimo Macucci, Giuseppe Iannaccone, Kostya S. Novoselov, Helen Holder, Gianluca Fiori, and Cinzia Casiraghi. All-2d Material Inkjet-Printed Capacitors: Toward Fully Printed Integrated Circuits. *ACS Nano*, 13(1):54–60, January 2019. 12, 23, 24, 99

[46] Jaime Taha-Tijerina, Tharangattu N. Narayanan, Guanhui Gao, Matthew Rohde, Dmitri A. Tsentalovich, Matteo Pasquali, and Pulickel M. Ajayan. Electrically Insulating Thermal Nano-Oils Using 2d Fillers. *ACS Nano*, 6(2):1214–1220, February 2012. 12

[47] Per Joensen, R. F. Frindt, and S. Roy Morrison. Single-layer MoS2. *Materials Research Bulletin*, 21(4):457–461, April 1986. 12

[48] Qing Hua Wang, Kourosh Kalantar-Zadeh, Andras Kis, Jonathan N. Coleman, and Michael S. Strano. Electronics and optoelectronics of two-dimensional transition metal dichalcogenides. *Nature Nanotechnology*, 7(11):699–712, November 2012. 12, 13, 14, 110

[49] B. Radisavljevic, A. Radenovic, J. Brivio, V. Giacometti, and A. Kis. Single-layer MoS2 transistors. *Nature Nanotechnology*, 6(3):147–150, March 2011. 13, 15, 16, 99, 117

[50] Manish Chhowalla, Hyeon Suk Shin, Goki Eda, Lain-Jong Li, Kian Ping Loh, and Hua Zhang. The chemistry of two-dimensional layered transition metal dichalcogenide nanosheets. *Nature Chemistry*, 5(4):263–275, April 2013. 13

[51] Goki Eda, Hisato Yamaguchi, Damien Voiry, Takeshi Fujita, Mingwei Chen, and Manish Chhowalla. Photoluminescence from Chemically Exfoliated MoS2. *Nano Letters*, 11(12):5111–5116, December 2011. 13, 14, 18

[52] Zhaoyang Lin, Yuan Liu, Udayabagya Halim, Mengning Ding, Yuanyue Liu, Yiliu Wang, Chuancheng Jia, Peng Chen, Xidong Duan, Chen Wang, Frank Song, Mufan Li, Chengzhang Wan, Yu Huang, and Xiangfeng Duan. Solution-processable 2d semiconductors for high-performance large-area electronics. *Nature*, 562(7726):254, October 2018. 13, 24

[53] Kin Fai Mak, Changgu Lee, James Hone, Jie Shan, and Tony F. Heinz. Atomically Thin ${\mathrm{MoS}}_{2}$: A New Direct-Gap Semiconductor. *Physical Review Letters*, 105(13):136805, September 2010. 13, 14, 15, 110

[54] A. Kuc, N. Zibouche, and T. Heine. Influence of quantum confinement on the electronic structure of the transition metal sulfide TS${}_{2}$. *Physical Review B*, 83(24):245213, June 2011. 13, 14

[55] Weijie Zhao, Zohreh Ghorannevis, Leiqiang Chu, Minglin Toh, Christian Kloc, Ping-Heng Tan, and Goki Eda. Evolution of Electronic Structure in Atomically Thin Sheets of WS2 and WSe2. *ACS Nano*, 7(1):791–797, January 2013. 14

[56] Claudia Backes, Ronan J. Smith, Niall McEvoy, Nina C. Berner, David McCloskey, Hannah C. Nerl, Arlene O'Neill, Paul J. King, Tom Higgins, Damien Hanlon, Nils Scheuschner, Janina Maultzsch, Lothar Houben, Georg S. Duesberg, John F. Donegan, Valeria Nicolosi, and Jonathan N. Coleman. Edge

and confinement effects allow in situ measurement of size and thickness of liquid-exfoliated nanosheets. *Nature Communications*, 5:4576, August 2014. 14, 15, 23, 34, 60, 62, 67, 74, 110, 112, 114, 120, 127, 162

[57] Claudia Backes, Beata M Szydlowska, Andrew Harvey, Shengjun Yuan, Victor Vega-Mayoral, Ben R. Davies, Pei-liang Zhao, Damien Hanlon, Elton Santos, Mikhail I Katsnelson, Werner Josef Blau, Christoph Gadermaier, and Jonathan N. Coleman. Production of Highly Monolayer Enriched Dispersions of Liquid-Exfoliated Nanosheets by Liquid Cascade Centrifugation. *ACS Nano*, 10(1):1589–1601, January 2016. 14, 15, 23, 29, 36, 50, 62, 66, 67, 82

[58] Andrea Splendiani, Liang Sun, Yuanbo Zhang, Tianshu Li, Jonghwan Kim, Chi-Yung Chim, Giulia Galli, and Feng Wang. Emerging Photoluminescence in Monolayer MoS2. *Nano Letters*, 10(4):1271–1275, April 2010. 14

[59] L. Britnell, R.M. Ribeiro, A. Eckmann, R. Jalil, B.D. Belle, A. Mishchenko, Y.-J. Kim, R.V. Gorbachev, T. Georgiou, S.V. Morozov, A.N. Grigorenko, A.K. Geim, C. Casiraghi, A.H. Castro Neto, and K.S. Novoselov. Strong light-matter interactions in heterostructures of atomically thin films. *Science*, 340(6138):1311–1314, 2013. 14, 15

[60] Marco Bernardi, Maurizia Palummo, and Jeffrey C. Grossman. Extraordinary Sunlight Absorption and One Nanometer Thick Photovoltaics Using Two-Dimensional Monolayer Materials. *Nano Letters*, 13(8):3664–3670, August 2013. 15

[61] Meng-Lin Tsai, Sheng-Han Su, Jan-Kai Chang, Dung-Sheng Tsai, Chang-Hsiao Chen, Chih-I Wu, Lain-Jong Li, Lih-Juann Chen, and Jr-Hau He. Monolayer MoS2 Heterojunction Solar Cells. *ACS Nano*, 8(8):8317–8322, August 2014. 15

[62] Wenjing Zhang, Jing-Kai Huang, Chang-Hsiao Chen, Yung-Huang Chang, Yuh-Jen Cheng, and Lain-Jong Li. High-Gain Phototransistors Based on a CVD MoS2 Monolayer. *Advanced Materials*, 25(25):3456–3461, 2013. 15

[63] Yexin Deng, Zhe Luo, Nathan J. Conrad, Han Liu, Yongji Gong, Sina Najmaei, Pulickel M. Ajayan, Jun Lou, Xianfan Xu, and Peide D. Ye. Black Phosphorus–Monolayer MoS2 van der Waals Heterojunction p–n Diode. *ACS Nano*, 8(8):8292–8299, August 2014. 15

[64] H. Zhang, S. B. Lu, J. Zheng, J. Du, S. C. Wen, D. Y. Tang, and K. P. Loh. Molybdenum disulfide (MoS_2) as a broadband saturable absorber for ultra-fast photonics. *Optics Express*, 22(6):7249–7260, March 2014. 15

[65] R. S. Sundaram, M. Engel, A. Lombardo, R. Krupke, A. C. Ferrari, Ph. Avouris, and M. Steiner. Electroluminescence in Single Layer MoS2. *Nano Letters*, 13(4):1416–1421, April 2013. 15

[66] Oriol Lopez-Sanchez, Esther Alarcon Llado, Volodymyr Koman, Anna Fontcuberta i Morral, Aleksandra Radenovic, and Andras Kis. Light Generation and Harvesting in a van der Waals Heterostructure. *ACS Nano*, 8(3):3042–3048, March 2014. 15

[67] Victor Vega-Mayoral, Claudia Backes, Damien Hanlon, Umar Khan, Zahra Gholamvand, Maria O'Brien, Georg S. Duesberg, Christoph Gadermaier, and Jonathan N. Coleman. Photoluminescence from Liquid-Exfoliated WS2 Monomers in Poly(Vinyl Alcohol) Polymer Composites. *Advanced Functional Materials*, pages n/a–n/a, December 2015. 15, 20, 24

[68] Branimir Radisavljevic, Michael Brian Whitwick, and Andras Kis. Integrated Circuits and Logic Operations Based on Single-Layer MoS2. *ACS Nano*, 5(12):9934–9938, December 2011. 15, 16

[69] Dominik Lembke and Andras Kis. Breakdown of High-Performance Monolayer MoS2 Transistors. *ACS Nano*, 6(11):10070–10075, November 2012. 15

[70] Saptarshi Das, Hong-Yan Chen, Ashish Verma Penumatcha, and Joerg Appenzeller. High Performance Multilayer MoS2 Transistors with Scandium Contacts. *Nano Letters*, 13(1):100–105, January 2013. 15, 16, 117

[71] Stephen McDonnell, Rafik Addou, Creighton Buie, Robert M. Wallace, and Christopher L. Hinkle. Defect-Dominated Doping and Contact Resistance in MoS2. *ACS Nano*, 8(3):2880–2888, March 2014. 15, 16, 117

[72] Youngki Yoon, Kartik Ganapathi, and Sayeef Salahuddin. How Good Can Monolayer MoS2 Transistors Be? *Nano Letters*, 11(9):3768–3773, September 2011. 16

[73] Vinod K. Sangwan and Mark C. Hersam. Electronic Transport in Two-Dimensional Materials. *Annual Review of Physical Chemistry*, 69(1):299–325, 2018. 16

[74] Jinhua Hong, Zhixin Hu, Matt Probert, Kun Li, Danhui Lv, Xinan Yang, Lin Gu, Nannan Mao, Qingliang Feng, Liming Xie, Jin Zhang, Dianzhong Wu, Zhiyong Zhang, Chuanhong Jin, Wei Ji, Xixiang Zhang, Jun Yuan, and Ze Zhang. Exploring atomic defects in molybdenum disulphide monolayers. *Nature Communications*, 6:6293, February 2015. 16

[75] Hannu-Pekka Komsa, Jani Kotakoski, Simon Kurasch, Ossi Lehtinen, Ute Kaiser, and Arkady V. Krasheninnikov. Two-Dimensional Transition Metal Dichalcogenides under Electron Irradiation: Defect Production and Doping. *Physical Review Letters*, 109(3):035503, July 2012. 16, 117, 119

[76] Wu Zhou, Xiaolong Zou, Sina Najmaei, Zheng Liu, Yumeng Shi, Jing Kong, Jun Lou, Pulickel M. Ajayan, Boris I. Yakobson, and Juan-Carlos Idrobo. Intrinsic Structural Defects in Monolayer Molybdenum Disulfide. *Nano Letters*, 13(6):2615–2622, June 2013. 16, 117, 119

[77] D. Liu, Y. Guo, L. Fang, and J. Robertson. Sulfur vacancies in monolayer MoS2 and its electrical contacts. *Applied Physics Letters*, 103(18):183113, October 2013. 16, 117, 119

[78] Dmitry Ovchinnikov, Adrien Allain, Ying-Sheng Huang, Dumitru Dumcenco,

and Andras Kis. Electrical Transport Properties of Single-Layer WS2. *ACS Nano*, 8(8):8174–8181, August 2014. 16

[79] Adam G. Kelly, Toby Hallam, Claudia Backes, Andrew Harvey, Amir Sajad Esmaeily, Ian Godwin, João Coelho, Valeria Nicolosi, Jannika Lauth, Aditya Kulkarni, Sachin Kinge, Laurens D. A. Siebbeles, Georg S. Duesberg, and Jonathan N. Coleman. All-printed thin-film transistors from networks of liquid-exfoliated nanosheets. *Science*, 356(6333):69–73, April 2017. 16, 22, 23, 24, 26, 99, 100, 110, 120, 122, 127

[80] Woong Choi, Mi Yeon Cho, Aniruddha Konar, Jong Hak Lee, Gi-Beom Cha, Soon Cheol Hong, Sangsig Kim, Jeongyong Kim, Debdeep Jena, Jinsoo Joo, and Sunkook Kim. High-Detectivity Multilayer MoS2 Phototransistors with Spectral Response from Ultraviolet to Infrared. *Advanced Materials*, 24(43):5832–5836, 2012. 16, 117

[81] Dung-Sheng Tsai, Keng-Ku Liu, Der-Hsien Lien, Meng-Lin Tsai, Chen-Fang Kang, Chin-An Lin, Lain-Jong Li, and Jr-Hau He. Few-Layer MoS2 with High Broadband Photogain and Fast Optical Switching for Use in Harsh Environments. *ACS Nano*, 7(5):3905–3911, May 2013. 16

[82] Graeme Cunningham, Umar Khan, Claudia Backes, Damien Hanlon, David McCloskey, John F. Donegan, and Jonathan N. Coleman. Photoconductivity of solution-processed MoS2 films. *Journal of Materials Chemistry C*, 1(41):6899–6904, October 2013. 16, 25, 116, 117, 118, 120

[83] Graeme Cunningham, Damien Hanlon, Niall McEvoy, Georg S. Duesberg, and Jonathan N. Coleman. Large variations in both dark- and photoconductivity in nanosheet networks as nanomaterial is varied from MoS2 to WTe2. *Nanoscale*, 7(1):198–208, December 2014. 16, 24, 25, 116, 117, 118, 119, 120, 122

[84] Zongping Chen, Wencai Ren, Libo Gao, Bilu Liu, Songfeng Pei, and Hui-Ming Cheng. Three-dimensional flexible and conductive interconnected graphene

networks grown by chemical vapour deposition. *Nature Materials*, 10(6):424–428, June 2011. 17

[85] Sukang Bae, Hyeongkeun Kim, Youngbin Lee, Xiangfan Xu, Jae-Sung Park, Yi Zheng, Jayakumar Balakrishnan, Tian Lei, Hye Ri Kim, Young Il Song, Young-Jin Kim, Kwang S. Kim, Barbaros Özyilmaz, Jong-Hyun Ahn, Byung Hee Hong, and Sumio Iijima. Roll-to-roll production of 30-inch graphene films for transparent electrodes. *Nature Nanotechnology*, 5(8):574–578, August 2010. 17

[86] Sasha Stankovich, Dmitriy A. Dikin, Richard D. Piner, Kevin A. Kohlhaas, Alfred Kleinhammes, Yuanyuan Jia, Yue Wu, SonBinh T. Nguyen, and Rodney S. Ruoff. Synthesis of graphene-based nanosheets via chemical reduction of exfoliated graphite oxide. *Carbon*, 45(7):1558–1565, June 2007. 18

[87] Daniel R. Dreyer, Sungjin Park, Christopher W. Bielawski, and Rodney S. Ruoff. The chemistry of graphene oxide. *Chemical Society Reviews*, 39(1):228–240, December 2009. 18

[88] Cristina Gómez-Navarro, R. Thomas Weitz, Alexander M. Bittner, Matteo Scolari, Alf Mews, Marko Burghard, and Klaus Kern. Electronic Transport Properties of Individual Chemically Reduced Graphene Oxide Sheets. *Nano Letters*, 7(11):3499–3503, November 2007. 18

[89] Cecilia Mattevi, Goki Eda, Stefano Agnoli, Steve Miller, K. Andre Mkhoyan, Ozgur Celik, Daniel Mastrogiovanni, Gaetano Granozzi, Eric Garfunkel, and Manish Chhowalla. Evolution of Electrical, Chemical, and Structural Properties of Transparent and Conducting Chemically Derived Graphene Thin Films. *Advanced Functional Materials*, 19(16):2577–2583, 2009. 18

[90] Héctor A. Becerril, Jie Mao, Zunfeng Liu, Randall M. Stoltenberg, Zhenan Bao, and Yongsheng Chen. Evaluation of Solution-Processed Reduced Graphene

Oxide Films as Transparent Conductors. *ACS Nano*, 2(3):463–470, March 2008. 18

[91] Xuan Wang, Linjie Zhi, and Klaus Müllen. Transparent, Conductive Graphene Electrodes for Dye-Sensitized Solar Cells. *Nano Letters*, 8(1):323–327, January 2008. 18

[92] M. J. Fernández-Merino, L. Guardia, J. I. Paredes, S. Villar-Rodil, P. Solís-Fernández, A. Martínez-Alonso, and J. M. D. Tascón. Vitamin C Is an Ideal Substitute for Hydrazine in the Reduction of Graphene Oxide Suspensions. *The Journal of Physical Chemistry C*, 114(14):6426–6432, April 2010. 18

[93] Damien Voiry, Jieun Yang, Jacob Kupferberg, Raymond Fullon, Calvin Lee, Hu Young Jeong, Hyeon Suk Shin, and Manish Chhowalla. High-quality graphene via microwave reduction of solution-exfoliated graphene oxide. *Science*, 353(6306):1413–1416, September 2016. 18

[94] Ronan J. Smith, Paul J. King, Mustafa Lotya, Christian Wirtz, Umar Khan, Sukanta De, Arlene O'Neill, Georg S. Duesberg, Jaime C. Grunlan, Gregory Moriarty, Jun Chen, Jiazhao Wang, Andrew I. Minett, Valeria Nicolosi, and Jonathan N. Coleman. Large-Scale Exfoliation of Inorganic Layered Compounds in Aqueous Surfactant Solutions. *Advanced Materials*, 23(34):3944–3948, September 2011. 19, 20

[95] Graeme Cunningham, Mustafa Lotya, Clotilde S. Cucinotta, Stefano Sanvito, Shane D. Bergin, Robert Menzel, Milo S. P. Shaffer, and Jonathan N. Coleman. Solvent Exfoliation of Transition Metal Dichalcogenides: Dispersibility of Exfoliated Nanosheets Varies Only Weakly between Compounds. *ACS Nano*, 6(4):3468–3480, April 2012. 19, 20

[96] Joohoon Kang, Joshua D. Wood, Spencer A. Wells, Jae-Hyeok Lee, Xiaolong Liu, Kan-Sheng Chen, and Mark C. Hersam. Solvent Exfoliation of Electronic-

Grade, Two-Dimensional Black Phosphorus. *ACS Nano*, 9(4):3596–3604, April 2015. 19, 49, 53

[97] Damien Hanlon, Claudia Backes, Evie Doherty, Clotilde S. Cucinotta, Nina C. Berner, Conor Boland, Kangho Lee, Andrew Harvey, Peter Lynch, Zahra Gholamvand, Saifeng Zhang, Kangpeng Wang, Glenn Moynihan, Anuj Pokle, Quentin M. Ramasse, Niall McEvoy, Werner J. Blau, Jun Wang, Gonzalo Abellan, Frank Hauke, Andreas Hirsch, Stefano Sanvito, David D. O'Regan, Georg S. Duesberg, Valeria Nicolosi, and Jonathan N. Coleman. Liquid exfoliation of solvent-stabilized few-layer black phosphorus for applications beyond electronics. *Nature Communications*, 6:8563, October 2015. 19, 20

[98] Andrew Harvey, Xiaoyun He, Ian J. Godwin, Claudia Backes, David McAteer, Nina C. Berner, Niall McEvoy, Auren Ferguson, Aleksey Shmeliov, Michael E. G. Lyons, Valeria Nicolosi, Georg S. Duesberg, John F. Donegan, and Jonathan N. Coleman. Production of Ni(OH)2 nanosheets by liquid phase exfoliation: from optical properties to electrochemical applications. *Journal of Materials Chemistry A*, 4(28):11046–11059, July 2016. 20

[99] David McAteer, Ian J. Godwin, Zheng Ling, Andrew Harvey, Lily He, Conor S. Boland, Victor Vega[U+2010]Mayoral, Beata Szydłowska, Aurélie A. Rovetta, Claudia Backes, John B. Boland, Xin Chen, Michael E. G. Lyons, and Jonathan N. Coleman. Liquid Exfoliated Co(OH)2 Nanosheets as Low-Cost, Yet High-Performance, Catalysts for the Oxygen Evolution Reaction. *Advanced Energy Materials*, 8(15):1702965, 2018. 20

[100] Umar Khan, Arlene O'Neill, Mustafa Lotya, Sukanta De, and Jonathan N. Coleman. High-Concentration Solvent Exfoliation of Graphene. *Small*, 6(7):864–871, April 2010. 20, 54

[101] Arlene O'Neill, Umar Khan, Peter N. Nirmalraj, John Boland, and Jonathan N Coleman. Graphene Dispersion and Exfoliation in Low Boiling Point Solvents.

The Journal of Physical Chemistry C, 115(13):5422–5428, April 2011. 20, 21, 56, 57, 58

[102] Sukanta De, Paul J. King, Mustafa Lotya, Arlene O'Neill, Evelyn M. Doherty, Yenny Hernandez, Georg S. Duesberg, and Jonathan N. Coleman. Flexible, Transparent, Conducting Films of Randomly Stacked Graphene from Surfactant-Stabilized, Oxide-Free Graphene Dispersions. *Small*, 6(3):458–464, 2010. 20, 23

[103] Mustafa Lotya, Paul J King, Umar Khan, Sukanta De, and Jonathan N Coleman. High-Concentration, Surfactant-Stabilized Graphene Dispersions. *ACS Nano*, 4(6):3155–3162, June 2010. 20, 54

[104] Peter May, Umar Khan, J. Marguerite Hughes, and Jonathan N. Coleman. Role of Solubility Parameters in Understanding the Steric Stabilization of Exfoliated Two-Dimensional Nanosheets by Adsorbed Polymers. *The Journal of Physical Chemistry C*, 116(20):11393–11400, May 2012. 20

[105] Panagiotis G. Karagiannidis, Stephen A. Hodge, Lucia Lombardi, Flavia Tomarchio, Nicolas Decorde, Silvia Milana, Ilya Goykhman, Yang Su, Steven V. Mesite, Duncan N. Johnstone, Rowan K. Leary, Paul A. Midgley, Nicola M. Pugno, Felice Torrisi, and Andrea C. Ferrari. Microfluidization of Graphite and Formulation of Graphene-Based Conductive Inks. *ACS Nano*, 11(3):2742–2755, March 2017. 20, 23

[106] Keith R. Paton, Eswaraiah Varrla, Claudia Backes, Ronan J. Smith, Umar Khan, Arlene O'Neill, Conor Boland, Mustafa Lotya, Oana M. Istrate, Paul King, Tom Higgins, Sebastian Barwich, Peter May, Pawel Puczkarski, Iftikhar Ahmed, Matthias Moebius, Henrik Pettersson, Edmund Long, João Coelho, Sean E. O'Brien, Eva K. McGuire, Beatriz Mendoza Sanchez, Georg S. Duesberg, Niall McEvoy, Timothy J. Pennycook, Clive Downing, Alison Crossley, Valeria Nicolosi, and Jonathan N. Coleman. Scalable production of large quant-

ities of defect-free few-layer graphene by shear exfoliation in liquids. *Nature Materials*, 13(6):624–630, June 2014. 20, 22, 54, 59, 62, 162

[107] Eswaraiah Varrla, Claudia Backes, Keith R. Paton, Andrew Harvey, Zahra Gholamvand, Joe McCauley, and Jonathan N. Coleman. Large-Scale Production of Size-Controlled MoS2 Nanosheets by Shear Exfoliation. *Chemistry of Materials*, 27(3):1129–1139, February 2015. 20

[108] Sonia Biccai, Sebastian Barwich, Daniel Boland, Andrew Harvey, Damien Hanlon, Niall McEvoy, and Jonathan N. Coleman. Exfoliation of 2d materials by high shear mixing. *2D Materials*, 2018. 20, 64

[109] T. J. Nacken, C. Damm, J. Walter, A. Rüger, and W. Peukert. Delamination of graphite in a high pressure homogenizer. *RSC Advances*, 5(71):57328–57338, June 2015. 20, 64

[110] A. E. Del Rio Castillo, V. Pellegrini, A. Ansaldo, F. Ricciardella, H. Sun, L. Marasco, J. Buha, Z. Dang, L. Gagliani, E. Lago, N. Curreli, S. Gentiluomo, F. Palazon, M. Prato, R. Oropesa-Nuñez, P. S. Toth, E. Mantero, M. Crugliano, A. Gamucci, A. Tomadin, M. Polini, and F. Bonaccorso. High-yield production of 2d crystals by wet-jet milling. *Materials Horizons*, 5(5):890–904, August 2018. 20

[111] Jonathan N. Coleman. Liquid-Phase Exfoliation of Nanotubes and Graphene. *Advanced Functional Materials*, 19(23):3680–3695, December 2009. 20, 84

[112] Charles M. Hansen. *Hansen Solubility Parameters: A User's Handbook, Second Edition*. CRC Press, June 2007. 21, 60

[113] Yenny Hernandez, Mustafa Lotya, David Rickard, Shane D. Bergin, and Jonathan N. Coleman. Measurement of Multicomponent Solubility Parameters for Graphene Facilitates Solvent Discovery. *Langmuir*, 26(5):3208–3213, March 2010. 22, 38, 54

[114] J.N. Coleman. Liquid exfoliation of defect-free graphene. *Accounts of Chemical Research*, 46(1):14–22, 2013. 22

[115] Claudia Backes, Keith Paton, Damien Hanlon, Shengjun Yuan, Mikhail Katsnelson, James Houston, Ronan Smith, David McCloskey, John Donegan, and Jonathan N. Coleman. Spectroscopic metrics allow in-situ measurement of mean size and thickness of liquid-exfoliated graphene nanosheets. *Nanoscale*, 8:4311–4323, January 2016. 22, 23, 34, 36, 49, 67, 74, 114

[116] Auren Ferguson, Andrew Harvey, Ian J. Godwin, Shane D. Bergin, and Jonathan N. Coleman. The dependence of the measured surface energy of graphene on nanosheet size. *2D Materials*, 4(1):015040, December 2016. 22, 84, 89, 90, 97

[117] Auren Ferguson, Ivan T. Caffrey, Claudia Backes, Jonathan N. Coleman, and Shane D. Bergin. Differentiating Defect and Basal Plane Contributions to the Surface Energy of Graphite Using Inverse Gas Chromatography. *Chemistry of Materials*, 28(17):6355–6366, September 2016. 22, 84, 89, 90, 97, 98

[118] Kangho Lee, Hye-Young Kim, Mustafa Lotya, Jonathan N. Coleman, Gyu-Tae Kim, and Georg S. Duesberg. Electrical Characteristics of Molybdenum Disulfide Flakes Produced by Liquid Exfoliation. *Advanced Materials*, 23(36):4178–4182, 2011. 22, 117

[119] Aideen Griffin, Andrew Harvey, Brian Cunningham, Declan Scullion, Tian Tian, Chih-Jen Shih, Myrta Grüning, John F Donegan, Elton J. G. Santos, Claudia Backes, and Jonathan N. Coleman. Spectroscopic size and thickness metrics for liquid-exfoliated h-BN. *Chemistry of Materials*, March 2018. 23, 34, 62, 66, 67, 162

[120] Graeme Cunningham, Mustafa Lotya, Niall McEvoy, Georg S. Duesberg, Paul van der Schoot, and Jonathan N. Coleman. Percolation scaling in composites

of exfoliated MoS2 filled with nanotubes and graphene. *Nanoscale*, 4(20):6260–6264, September 2012. 23, 24, 71, 117

[121] Felice Torrisi, Tawfique Hasan, Weiping Wu, Zhipei Sun, Antonio Lombardo, Tero S. Kulmala, Gen-Wen Hsieh, Sungjune Jung, Francesco Bonaccorso, Philip J. Paul, Daping Chu, and Andrea C. Ferrari. Inkjet-Printed Graphene Electronics. *ACS Nano*, 6(4):2992–3006, April 2012. 23

[122] Jiantong Li, Maziar M. Naiini, Sam Vaziri, Max C. Lemme, and Mikael Östling. Inkjet Printing of MoS2. *Advanced Functional Materials*, 24(41):6524–6531, 2014. 23, 24

[123] Daryl McManus, Sandra Vranic, Freddie Withers, Veronica Sanchez-Romaguera, Massimo Macucci, Huafeng Yang, Roberto Sorrentino, Khaled Parvez, Seok-Kyun Son, Giuseppe Iannaccone, Kostas Kostarelos, Gianluca Fiori, and Cinzia Casiraghi. Water-based and biocompatible 2d crystal inks for all-inkjet-printed heterostructures. *Nature Nanotechnology*, 12(4):343–350, April 2017. 23

[124] Tian Carey, Stefania Cacovich, Giorgio Divitini, Jiesheng Ren, Aida Mansouri, Jong M. Kim, Chaoxia Wang, Caterina Ducati, Roman Sordan, and Felice Torrisi. Fully inkjet-printed two-dimensional material field-effect heterojunctions for wearable and textile electronics. *Nature Communications*, 8(1):1202, October 2017. 23, 24, 99

[125] C. Casiraghi, M. Macucci, K. Parvez, R. Worsley, Y. Shin, F. Bronte, C. Borri, M. Paggi, and G. Fiori. Inkjet printed 2d-crystal based strain gauges on paper. *Carbon*, 129:462–467, April 2018. 23

[126] Xianjun Huang, Ting Leng, Mengjian Zhu, Xiao Zhang, JiaCing Chen, KuoHsin Chang, Mohammed Aqeeli, Andre K. Geim, Kostya S. Novoselov, and Zhirun Hu. Highly Flexible and Conductive Printed Graphene for Wireless Wearable Communications Applications. *Scientific Reports*, 5:18298, December 2015. 23

[127] Kewen Pan, Yangyang Fan, Ting Leng, Jiashen Li, Zhiying Xin, Jiawei Zhang, Ling Hao, John Gallop, Kostya S. Novoselov, and Zhirun Hu. Sustainable production of highly conductive multilayer graphene ink for wireless connectivity and IoT applications. *Nature Communications*, 9(1):5197, December 2018. 23

[128] Jung-Woo Ted Seo, Jian Zhu, Vinod K. Sangwan, Ethan B. Secor, Shay G. Wallace, and Mark C. Hersam. Fully Inkjet-Printed, Mechanically Flexible MoS2 Nanosheet Photodetectors. *ACS Applied Materials & Interfaces*, 11(6):5675–5681, February 2019. 24

[129] Thomas M. Higgins, Sean Finn, Maik Matthiesen, Sebastian Grieger, Kevin Synnatschke, Maximilian Brohmann, Marcel Rother, Claudia Backes, and Jana Zaumseil. Electrolyte-Gated n-Type Transistors Produced from Aqueous Inks of WS2 Nanosheets. *Advanced Functional Materials*, 0(0):1804387, 2018. 24, 26, 53, 100, 127

[130] Adam G. Kelly, Conor Murphy, Victor Vega-Mayoral, Andrew Harvey, Amir Sajad Esmaeily, Toby Hallam, David McCloskey, and Jonathan N. Coleman. Tuneable photoconductivity and mobility enhancement in printed MoS 2 /graphene composites. *2D Materials*, 4(4):041006, 2017. 24, 117, 118, 120

[131] Domhnall O'Suilleabhain, Victor Vega-Mayoral, Adam Kelly, Andrew Harvey, and Jonathan N Coleman. Percolation Effects in Electrolytically-Gated WS2/Graphene Nano:Nano Composites. *ACS Applied Materials & Interfaces*, January 2019. 24

[132] Peter Lynch, Umar Khan, Andrew Harvey, Iftikhar Ahmed, and Jonathan N. Coleman. Graphene-MoS 2 nanosheet composites as electrodes for dye sensitised solar cells. *Materials Research Express*, 3(3):035007, 2016. 24, 71

[133] Sukanta De, Philip E. Lyons, Sophie Sorel, Evelyn M. Doherty, Paul J. King, Werner J. Blau, Peter N. Nirmalraj, John J. Boland, Vittorio Scardaci, Jerome Joimel, and Jonathan N. Coleman. Transparent, Flexible, and Highly Con-

ductive Thin Films Based on Polymer−Nanotube Composites. *ACS Nano*, 3(3):714–720, March 2009. 24

[134] Umar Khan, Peter May, Arlene O'Neill, and Jonathan N. Coleman. Development of stiff, strong, yet tough composites by the addition of solvent exfoliated graphene to polyurethane. *Carbon*, 48(14):4035–4041, November 2010. 24

[135] Peter May, Umar Khan, Arlene O'Neill, and Jonathan N. Coleman. Approaching the theoretical limit for reinforcing polymers with graphene. *Journal of Materials Chemistry*, 22(4):1278–1282, December 2011. 24

[136] Lei Gong, Robert J. Young, Ian A. Kinloch, Ibtsam Riaz, Rashid Jalil, and Kostya S. Novoselov. Optimizing the Reinforcement of Polymer-Based Nanocomposites by Graphene. *ACS Nano*, 6(3):2086–2095, March 2012. 24

[137] Dimitrios G. Papageorgiou, Ian A. Kinloch, and Robert J. Young. Mechanical properties of graphene and graphene-based nanocomposites. *Progress in Materials Science*, 90:75–127, October 2017. 24

[138] C.S. Boland, U. Khan, C. Backes, A. O'Neill, J. McCauley, S. Duane, R. Shanker, Y. Liu, I. Jurewicz, A.B. Dalton, and J.N. Coleman. Sensitive, high-strain, high-rate bodily motion sensors based on graphene-rubber composites. *ACS Nano*, 8(9):8819–8830, 2014. 24

[139] Conor S. Boland, Umar Khan, Gavin Ryan, Sebastian Barwich, Romina Charifou, Andrew Harvey, Claudia Backes, Zheling Li, Mauro S. Ferreira, Matthias E. Möbius, Robert J. Young, and Jonathan N. Coleman. Sensitive electromechanical sensors using viscoelastic graphene-polymer nanocomposites. *Science*, 354(6317):1257–1260, December 2016. 24

[140] Oana M. Istrate, Keith R. Paton, Umar Khan, Arlene O'Neill, Alan P. Bell, and Jonathan N. Coleman. Reinforcement in melt-processed polymer–graphene composites at extremely low graphene loading level. *Carbon*, 78:243–249, November 2014. 24, 71

[141] Shaobo Xie, Oana M. Istrate, Peter May, Sebastian Barwich, Alan P. Bell, Umar Khan, and Jonathan N. Coleman. Boron nitride nanosheets as barrier enhancing fillers in melt processed composites. *Nanoscale*, 7(10):4443–4450, February 2015. 24

[142] Meng Zhang, Richard C. T. Howe, Robert I. Woodward, Edmund J. R. Kelleher, Felice Torrisi, Guohua Hu, Sergei V. Popov, J. Roy Taylor, and Tawfique Hasan. Solution processed MoS2-PVA composite for sub-bandgap mode-locking of a wideband tunable ultrafast Er:fiber laser. *Nano Research*, 8(5):1522–1534, May 2015. 24

[143] I. Jurewicz, P. Worajittiphon, A.A.K. King, P.J. Sellin, J.L. Keddie, and A.B. Dalton. Locking carbon nanotubes in confined lattice geometries - A route to low percolation in conducting composites. *Journal of Physical Chemistry B*, 115(20):6395–6400, 2011. 25, 72

[144] Yves Chevalier and Marie-Alexandrine Bolzinger. Emulsions stabilized with solid nanoparticles: Pickering emulsions. *Colloids and Surfaces A: Physicochemical and Engineering Aspects*, 439:23–34, December 2013. 25, 72, 84

[145] Stefan Bon. *Particle-Stabilized Emulsions and Colloids*. November 2014. 25, 72, 95

[146] N. P. Ashby and B. P. Binks. Pickering emulsions stabilised by Laponite clay particles. *Physical Chemistry Chemical Physics*, 2(24):5640–5646, January 2000. 25, 72, 95

[147] Séverine Cauvin, Patrick J. Colver, and Stefan A. F. Bon. Pickering Stabilized Miniemulsion Polymerization: Preparation of Clay Armored Latexes. *Macromolecules*, 38(19):7887–7889, September 2005. 25, 72, 95

[148] Yongqiang He, Fei Wu, Xiying Sun, Ruqiang Li, Yongqin Guo, Chuanbao Li, Lu Zhang, Fubao Xing, Wei Wang, and Jianping Gao. Factors that Affect

Pickering Emulsions Stabilized by Graphene Oxide. *ACS Applied Materials & Interfaces*, 5(11):4843–4855, June 2013. 25, 72, 95

[149] Robert T. Woodward, Foivos Markoulidis, François De Luca, David B. Anthony, Daniel Malko, Tom O. McDonald, Milo S. P. Shaffer, and Alexander Bismarck. Carbon foams from emulsion-templated reduced graphene oxide polymer composites: electrodes for supercapacitor devices. *Journal of Materials Chemistry A*, 6(4):1840–1849, January 2018. 25, 72, 96

[150] Steven J. Woltornist, Jan-Michael Y. Carrillo, Thomas O. Xu, Andrey V. Dobrynin, and Douglas H. Adamson. Polymer/Pristine Graphene Based Composites: From Emulsions to Strong, Electrically Conducting Foams. *Macromolecules*, 48(3):687–693, February 2015. 25, 72, 95

[151] Matthew J. Large, Sean P. Ogilvie, Manuela Meloni, Aline Amorim Graf, Giuseppe Fratta, Jonathan Salvage, Alice A. K. King, and Alan B. Dalton. Functional liquid structures by emulsification of graphene and other two-dimensional nanomaterials. *Nanoscale*, January 2018. 25, 54, 72, 75, 84, 95

[152] Steven J. Woltornist, Deepthi Varghese, Daniel Massucci, Zhen Cao, Andrey V. Dobrynin, and Douglas H. Adamson. Controlled 3d Assembly of Graphene Sheets to Build Conductive, Chemically Selective and Shape-Responsive Materials. *Advanced Materials*, 29(18):1604947, 2017. 25, 72, 95

[153] Steven J. Woltornist, Andrew J. Oyer, Jan-Michael Y. Carrillo, Andrey V. Dobrynin, and Douglas H. Adamson. Conductive Thin Films of Pristine Graphene by Solvent Interface Trapping. *ACS Nano*, 7(8):7062–7066, August 2013. 25

[154] Xiaoyun Yu, Mathieu S. Prévot, Néstor Guijarro, and Kevin Sivula. Self-assembled 2d WSe_2 thin films for photoelectrochemical hydrogen production. *Nature Communications*, 6:7596, July 2015. 25

[155] Renhao Dong, Tao Zhang, and Xinliang Feng. Interface-Assisted Synthesis of 2d Materials: Trend and Challenges. *Chemical Reviews*, 118(13):6189–6235, July 2018. 25

[156] Laura J. Cote, Franklin Kim, and Jiaxing Huang. Langmuir−Blodgett Assembly of Graphite Oxide Single Layers. *Journal of the American Chemical Society*, 131(3):1043–1049, January 2009. 25, 100, 105

[157] Régis Y. N. Gengler, Alina Veligura, Apostolos Enotiadis, Evmorfia K. Diamanti, Dimitrios Gournis, Csaba Józsa, Bart J. van Wees, and Petra Rudolf. Large-Yield Preparation of High-Electronic-Quality Graphene by a Langmuir–Schaefer Approach. *Small*, 6(1):35–39, January 2010. 25, 100, 105

[158] Qingbin Zheng, Wai Hing Ip, Xiuyi Lin, Nariman Yousefi, Kan Kan Yeung, Zhigang Li, and Jang-Kyo Kim. Transparent Conductive Films Consisting of Ultralarge Graphene Sheets Produced by Langmuir–Blodgett Assembly. *ACS Nano*, 5(7):6039–6051, July 2011. 25, 100, 105

[159] HoKwon Kim, Cecilia Mattevi, Hyun Jun Kim, Anudha Mittal, K. Andre Mkhoyan, Richard E. Riman, and Manish Chhowalla. Optoelectronic properties of graphene thin films deposited by a Langmuir–Blodgett assembly. *Nanoscale*, 5(24):12365–12374, November 2013. 25, 100, 105

[160] A. Fahimi, I. Jurewicz, R.J. Smith, C.S. Sharrock, D.A. Bradley, S.J. Henley, J.N. Coleman, and A.B. Dalton. Density controlled conductivity of pristine graphene films. *Carbon*, 64:435–443, 2013. 25, 99, 100, 105

[161] Yefeng Zhang, Luzhu Xu, Wesley R. Walker, Collin M. Tittle, Christopher J. Backhouse, and Michael A. Pope. Langmuir films and uniform, large area, transparent coatings of chemically exfoliated MoS2 single layers. *Journal of Materials Chemistry C*, 5(43):11275–11287, November 2017. 25, 100, 105

[162] Taeyeong Yun, Jong-Seon Kim, Jongwon Shim, Dong Sung Choi, Kyung Eun Lee, Sung Hwan Koo, InHo Kim, Hong Ju Jung, Hae-Wook Yoo, Hee-Tae

Jung, and Sang Ouk Kim. Ultrafast Interfacial Self-Assembly of 2d Transition Metal Dichalcogenides Monolayer Films and Their Vertical and In-Plane Heterostructures. *ACS Applied Materials & Interfaces*, 9(1):1021–1028, January 2017. 25, 105

[163] A. Sesis, M. Hodnett, G. Memoli, A.J. Wain, I. Jurewicz, A.B. Dalton, J.D. Carey, and G. Hinds. Influence of acoustic cavitation on the controlled ultrasonic dispersion of carbon nanotubes. *Journal of Physical Chemistry B*, 117(48):15141–15150, 2013. 28, 55

[164] A. C. Ferrari, J. C. Meyer, V. Scardaci, C. Casiraghi, M. Lazzeri, F. Mauri, S. Piscanec, D. Jiang, K. S. Novoselov, S. Roth, and A. K. Geim. Raman Spectrum of Graphene and Graphene Layers. *Physical Review Letters*, 97(18):187401, October 2006. 36

[165] Rossitza G. Alargova, Shigeru Deguchi, and Kaoru Tsujii. Stable Colloidal Dispersions of Fullerenes in Polar Organic Solvents. *Journal of the American Chemical Society*, 123(43):10460–10467, October 2001. 37

[166] J. G. Masters, Y. Sun, A. G. MacDiarmid, and A. J. Epstein. Polyaniline: Allowed oxidation states. *Synthetic Metals*, 41(1):715–718, April 1991. 37

[167] Kevin D. Ausman, Richard Piner, Oleg Lourie, Rodney S. Ruoff, and Mikhail Korobov. Organic Solvent Dispersions of Single-Walled Carbon Nanotubes: Toward Solutions of Pristine Nanotubes. *The Journal of Physical Chemistry B*, 104(38):8911–8915, September 2000. 37

[168] Charles M Hansen and Allan L Smith. Using Hansen solubility parameters to correlate solubility of C60 fullerene in organic solvents and in polymers. *Carbon*, 42(8–9):1591–1597, 2004. 38

[169] Shane D. Bergin, Zhenyu Sun, David Rickard, Philip V. Streich, James P. Hamilton, and Jonathan N. Coleman. Multicomponent Solubility Parameters

for Single-Walled Carbon Nanotube−Solvent Mixtures. *ACS Nano*, 3(8):2340–2350, August 2009. 38

[170] Jack R. Brent, Nicky Savjani, Edward A. Lewis, Sarah J. Haigh, David J. Lewis, and Paul O'Brien. Production of few-layer phosphorene by liquid exfoliation of black phosphorus. *Chemical Communications*, 50(87):13338–13341, October 2014. 38, 49

[171] Hin Chun Yau, Mustafa K. Bayazit, Joachim H. G. Steinke, and Milo S. P. Shaffer. Sonochemical degradation of N-methylpyrrolidone and its influence on single walled carbon nanotube dispersion. *Chemical Communications*, 51(93):16621–16624, November 2015. 38, 41, 47, 48, 49

[172] Ali Jawaid, Dhriti Nepal, Kyoungweon Park, Michael Jespersen, Anthony Qualley, Peter Mirau, Lawrence F. Drummy, and Richard A. Vaia. Mechanism for Liquid Phase Exfoliation of MoS2. *Chemistry of Materials*, 28(1):337–348, January 2016. 38, 39, 47, 49, 57

[173] Amit Gupta, Vaishali Arunachalam, and Sukumaran Vasudevan. Liquid-Phase Exfoliation of MoS2 Nanosheets: The Critical Role of Trace Water. *The Journal of Physical Chemistry Letters*, 7(23):4884–4890, December 2016. 38

[174] Kausik Manna, Cheng-Yu Hsieh, Shen-Chuan Lo, Yan-Sheng Li, Huin-Ning Huang, and Wei-Hung Chiang. Graphene and graphene-analogue nanosheets produced by efficient water-assisted liquid exfoliation of layered materials. *Carbon*, 105:551–555, August 2016. 38

[175] Guoshan Song, Yannan Lin, Zhongcheng Zhu, Heying Zheng, Jinping Qiao, Changcheng He, and Huiliang Wang. Strong Fluorescence of Poly(N-vinylpyrrolidone) and Its Oxidized Hydrolyzate. *Macromolecular Rapid Communications*, 36(3):278–285, February 2015. 39

[176] A. Naumenko, M. Biliy, V. Gubanov, and A. Navozenko. Spectroscopic studies

of fullerene clusters in N-methyl-2-pyrrolidone. *Journal of Molecular Liquids*, 235:115–118, 2017. 39

[177] Sean P. Ogilvie, Matthew J. Large, Giuseppe Fratta, Manuela Meloni, Ruben Canton-Vitoria, Nikos Tagmatarchis, Florian Massuyeau, Christopher P. Ewels, Alice A. K. King, and Alan B. Dalton. Considerations for spectroscopy of liquid-exfoliated 2d materials: emerging photoluminescence of N -methyl-2-pyrrolidone. *Scientific Reports*, 7(1):16706, December 2017. 41, 57

[178] R. Sainz, A.M. Benito, M.T. Martínez, J.F. Galindo, J. Sotres, A.M. Baró, B. Corraze, O. Chauvet, A.B. Dalton, R.H. Baughman, and W.K. Maser. A soluble and highly functional polyaniline-carbon nanotube composite. *Nanotechnology*, 16(5):S150–S154, 2005. 49

[179] Silvia Giordani, Shane D. Bergin, Valeria Nicolosi, Sergei Lebedkin, Manfred M. Kappes, Werner J. Blau, and Jonathan N. Coleman. Debundling of Single-Walled Nanotubes by Dilution: Observation of Large Populations of Individual Nanotubes in Amide Solvent Dispersions. *The Journal of Physical Chemistry B*, 110(32):15708–15718, August 2006. 49

[180] M. Mar Bernal, Lidia Álvarez, Emerson Giovanelli, Adriana Arnáiz, Luisa Ruiz-González, Santiago Casado, Daniel Granados, Ana M. Pizarro, Andres Castellanos-Gomez, and Emilio M. Pérez. Luminescent transition metal dichalcogenide nanosheets through one-step liquid phase exfoliation. *2D Materials*, 3(3):035014, 2016. 49

[181] Georgia Pagona, Carla Bittencourt, Raul Arenal, and Nikos Tagmatarchis. Exfoliated semiconducting pure 2h-MoS2 and 2h-WS2 assisted by chlorosulfonic acid. *Chemical Communications*, 51(65):12950–12953, July 2015. 49, 50

[182] Ziyin Lin, Andrew Mcnamara, Yan Liu, Kyoung-sik Moon, and Ching-Ping Wong. Exfoliated hexagonal boron nitride-based polymer nanocomposite with

enhanced thermal conductivity for electronic encapsulation. *Composites Science and Technology*, 90:123–128, January 2014. 53

[183] Gyeong Sook Bang, Kwan Woo Nam, Jong Yun Kim, Jongwoo Shin, Jang Wook Choi, and Sung-Yool Choi. Effective Liquid-Phase Exfoliation and Sodium Ion Battery Application of MoS2 Nanosheets. *ACS Applied Materials & Interfaces*, 6(10):7084–7089, May 2014. 53

[184] Fang Song and Xile Hu. Exfoliation of layered double hydroxides for enhanced oxygen evolution catalysis. *Nature Communications*, 5:4477, July 2014. 53

[185] David R. Lide. *CRC Handbook of Chemistry and Physics, 85th Edition*. CRC Press, June 2004. Google-Books-ID: WDll8hA006AC. 57, 60

[186] Ryan McGorty, Jerome Fung, David Kaz, and Vinothan N. Manoharan. Colloidal self-assembly at an interface. *Materials Today*, 13(6):34–42, June 2010. 71

[187] Jae-Ung Lee, Jaesung Park, Young-Woo Son, and Hyeonsik Cheong. Anomalous excitonic resonance Raman effects in few-layered MoS2. *Nanoscale*, 7(7):3229–3236, February 2015. 80, 164

[188] F. M. Fowkes. DETERMINATION OF INTERFACIAL TENSIONS, CONTACT ANGLES, AND DISPERSION FORCES IN SURFACES BY ASSUMING ADDITIVITY OF INTERMOLECULAR INTERACTIONS IN SURFACES. *The Journal of Physical Chemistry*, 66(2):382–382, February 1962. 84

[189] Souheng Wu. Calculation of interfacial tension in polymer systems. *Journal of Polymer Science Part C: Polymer Symposia*, 34(1):19–30, January 1971. 84

[190] Matthew J. Large, Sean P. Ogilvie, Alice A. K. King, and Alan B. Dalton. Understanding Solvent Spreading for Langmuir Deposition of Nanomaterial Films: A Hansen Solubility Parameter Approach. *Langmuir*, 33(51):14766–14771, December 2017. 85, 101, 103

[191] Svetlana R. Derkach. Rheology of emulsions. *Advances in Colloid and Interface Science*, 151(1):1–23, October 2009. 93, 94

[192] Bernard P. Binks, John H. Clint, and Catherine P. Whitby. Rheological Behavior of Water-in-Oil Emulsions Stabilized by Hydrophobic Bentonite Particles. *Langmuir*, 21(12):5307–5316, June 2005. 93

[193] Rajinder Pal. Effect of droplet size on the rheology of emulsions. *AIChE Journal*, 42(11):3181–3190, 1996. 94

[194] D. M. Koenhen and C. A. Smolders. The determination of solubility parameters of solvents and polymers by means of correlations with other physical quantities. *Journal of Applied Polymer Science*, 19(4):1163–1179, April 1975. 102

[195] Matthew J. Large, Sean P. Ogilvie, Sultan Alomairy, Terence Vöckerodt, David Myles, Maria Cann, Helios Chan, Izabela Jurewicz, Alice A. K. King, and Alan B. Dalton. Selective Mechanical Transfer Deposition of Langmuir Graphene Films for High-Performance Silver Nanowire Hybrid Electrodes. *Langmuir*, 33(43):12038–12045, October 2017. 105

[196] Keith R. Paton and Jonathan N. Coleman. Relating the optical absorption coefficient of nanosheet dispersions to the intrinsic monolayer absorption. *Carbon*, 107:733–738, October 2016. 110

[197] Nannan Mao, Yanfeng Chen, Dameng Liu, Jin Zhang, and Liming Xie. Solvatochromic Effect on the Photoluminescence of MoS2 Monolayers. *Small*, 9(8):1312–1315, 2013. 114, 115

[198] Jungwook Choi, Hanyu Zhang, Haodong Du, and Jong Hyun Choi. Understanding Solvent Effects on the Properties of Two-Dimensional Transition Metal Dichalcogenides. *ACS Applied Materials & Interfaces*, 8(14):8864–8869, April 2016. 114

[199] Khaled Parvez, Robyn Worsley, Adriana Alieva, Alexandre Felten, and Cinzia

Casiraghi. Water-based and inkjet printable inks made by electrochemically exfoliated graphene. *Carbon*, 149:213–221, August 2019. 123

[200] Nadia Grossiord, Paul van der Schoot, Jan Meuldijk, and Cor E. Koning. Determination of the Surface Coverage of Exfoliated Carbon Nanotubes by Surfactant Molecules in Aqueous Solution. *Langmuir*, 23(7):3646–3653, March 2007. 124

[201] Lucas Ueberricke, Jonathan N. Coleman, and Claudia Backes. Robustness of Size Selection and Spectroscopic Size, Thickness and Monolayer Metrics of Liquid-Exfoliated WS2. *physica status solidi (b)*, 254(11):n/a–n/a, November 2017. 162

Appendix A

Experimental methods

A.1 Methods for Chapter 4

Materials

NMP for the as-received and sonicated samples was purchased from Sigma Aldrich, product number 270458. NMP for the aged samples was purchased from Sigma Aldrich and Fisher Scientific with the dates of receipt and product numbers as follows: NMP-9, 06/07/2007, Sigma 328634; NMP-4, 24/10/2012, Fisher M/5120/08; NMP-1, 01/10/2015, Sigma C112402. MoS_2 powder was purchased from Sigma Aldrich. Graphite powder was supplied by Zenyatta Ventures Ltd.

Characterisation methods

UV-visible spectroscopy measurements were performed using a Shimadzu UV-2501PC spectrophotometer and Shimadzu UV-3600 Plus spectrophotometer using quartz cuvettes. Photoluminescence spectroscopy was performed using Cary Eclipse spectrophotometer and a Shimadzu RF-6000 spectrofluorometer. Raman spectra were acquired using an NT-MDT NTEGRA Spectra system with 473 nm laser excitation and Renishaw inVia system with 532 nm laser excitation. The photoluminescence background was subtracted using spline interpolation and the spectra were then normalized to the Raman mode at $\sim$2900 cm^{-1}. Time-resolved photoluminescence measurements were performed with a Horiba DeltaFlex TCSPC system with excitation at 336 nm, 349 nm and 409 nm using a 6 nm bandpass. ^1H NMR spectroscopy

was performed on a Varian VNMRS 600 spectrometer operating at a ^{1}H frequency of 599.7 MHz.

Sonication and liquid phase exfoliation

Sonochemical degradation of NMP was performed with a Sonics Vibra-Cell VCX130 ultrasonic probe. 20 mL of NMP was sonicated for 1 hour at 75% amplitude (∼30 W power output), to produce the sample designated NMP(s). For the liquid-exfoliated graphene samples, graphite powder was added to 20 mL of NMP at an initial concentration of 25 g/L and sonicated for 1 hour at 75% amplitude. The sample was then centrifuged for 1 hour at 4000 g using a Thermo Scientific Sorvall Legend X1. For the liquid-exfoliated MoS_2 samples, MoS_2 powder was added to 20 mL of NMP at an initial concentration of 25 g/L. The supernatant was then discarded and the sediment was redispersed into another 20 mL of NMP. This was then sonicated for 1 hour at 50% amplitude with a pulse of 6 s on and 2 s off. The sample was then centrifuged for 1 hour at 2000 g, the sediment was discarded and the supernatant was collected. After the final centrifugation, all samples were left to stand overnight before characterisation. For the non-degraded samples, as-received NMP was used throughout the process. For the degraded samples, NMP(s) was used throughout the process.

A.2 Methods for Chapter 5

Viscosity effects and CPO/CHO mixing

Power measurements were performed using a Sonics Vibra-cell VCX-130 probe on 20 mL of solvent in identical glass vials with the probe at a fixed height relative to the bottom of the vial. MoS_2 powder, sodium cholate hydrate and all solvents were purchased from Sigma Aldrich. For the CPO/CHO mixing experiment, MoS_2 powder was added to 30 mL of CPO at an initial concentration of 10 g/L and subjected to 1 hour of continuous probe sonication (VCX130) at 60% amplitude. The dispersion was then centrifuged (Thermo Scientific Sorvall Legend X1 with High Conic II rotor) at 5000 g for 5 mins resulting in sedimentation of all material

except very small nanosheets and impurities. This centrifugation was performed using a Thermo Scientific Sorvall Legend X1. The supernatant was discarded and the sediment was redispersed in to 30 mL of fresh CPO and subjected to a further 3 hours of continuous probe sonication at 60% amplitude. The dispersion was then centrifuged (Thermo Scientific Sorvall Legend X1 with High Conic II rotor) at 5000 g for 5 mins to leave only few-layer nanosheets dispersed in the supernatant. The sediment was discarded and the few-layer MoS_2 dispersion (supernatant) was divided between two vials and diluted by a factor of 5, one into more CPO and one into CHO. These dispersions were subjected to further centrifugation of 5000 g for 10 mins to allow comparison of the effects of viscosity on the same initial dispersion of nanosheets. UV-visible extinction spectroscopy was performed using a Shimadzu UV3600Plus spectrometer.

LCC with speed variation

For the first set of liquid cascade centrifugation in the calibration experiment (speed variation experiment), the starting material (MoS_2, WS_2, BN, graphite all purchased from Sigma Aldrich) at a concentration of 20 g/L was immersed in in a 6 g/L aqueous solution of sodium cholate solution in a metal beaker and subjected to probe sonicating (VibraCell VCX500, flathead tip) for 1 hour at 60% amplitude. The beaker was mounted in a water bath connected to a chiller system to maintain the external temperature at 5 °C during sonication. The dispersion was then centrifuged in a Hettich Mikro 220R centrifuge equipped with a fixed-angle rotor 1016 at 2260 g for 2 hours. The supernatant was removed. From our experience, this relatively short initial sonication removes impurities in the supernatant which otherwise destabilise the dispersion. The sediment was redispersed in fresh surfactant solution (2 g/L). and subsequently sonicated for 5 hours at 60% amplitude with a pulse of 6 on and 2 off (water cooling). The resultant stock dispersion was centrifuged at 27 g for 2 hours, sediment discarded and the supernatant subjected to size selection. For the size selection of nanosheets, we used a centrifugation cascade increasing the speed and moving the supernatant on to the next stage each time. The sediment

after each centrifugation was collected and redispersed in fresh surfactant solution, while the supernatant was centrifuged at higher centrifugal acceleration. The final supernatant was discarded. For centrifugation <3000 *g*, a Hettich Mikro 220R centrifuge equipped with a fixed-angle rotor 1016 (50 mL vials filled with 20 mL each) was used. For centrifugation >3000 *g*, a Hettich Mikro 220R centrifuge equipped with a fixed-angle rotor 1195-A (1.5 mL vials). All centrifugation was performed for 2 hours at 15 °C. Centrifugal *g*-force was varied slightly depending on the starting material. graphene: 100 *g*, 400 *g*, 1000 *g*, 5000 *g*, 10000 *g*, 30000 *g*. BN: 400 *g*, 1000 *g*, 5000 *g*, 10000 *g*, 22000 *g*, 74000 *g*, WS_2 and MoS_2, 100 *g*, 400 *g*, 1000 *g*, 5000 *g*, 10000 *g*, 22000 *g*, 74000 *g*. On these dispersions, atomic force microscopy (AFM) was carried out on a Dimension ICON3 scanning probe microscope (Bruker AXS S.A.S.) in ScanAsyst in air under ambient conditions using aluminum coated silicon cantilevers (OLTESP-R3). The concentrated dispersions were diluted with water to optical densities <0.1 across the resonant spectral region. A drop of the dilute dispersions (20 µL) was deposited on a pre-heated (180 °C) Si/SiO_2 wafers (0.5x0.5 cm^2) with an oxide layer of 300 nm. After deposition, the wafers were rinsed with ∼5 mL of water and ∼5 mL of isopropanol. Typical image sizes were 10x10 μm^2 for larger nanosheets (100-1000 *g*, and 400-1000 *g*) and ranged down to 4x4 μm^2 for smaller nanosheets at scan rates of 0.5 Hz with 1024 lines per image. For the statistical analysis, only individualized nanosheets (no aggregates) were counted and their longest dimension (L), the dimension perpendicular to this (width, W) and the thickness measured. Thickness was converted to layer number by using known step heights [106, 56, 119]. The lateral dimension was corrected by a previously established correction to account for cantilever broadening and pixilation [201]. In each case 150-250 nanosheets were counted (depending on the polydispersity of the fraction) until the distribution histograms showed the typical lognormal distribution.

LCC with time variation

For the second set of liquid cascade centrifugation in the calibration experiment (time variation experiment), MoS_2 powder was added to 30 mL of aqueous surfactant

solution (6 g/L sodium cholate concentration) at an initial MoS_2 concentration of 25 g/L. The dispersion was then subjected to continuous probe sonication (Sonics Vibra-cell VCX130) at 60% amplitude for 1 hour, followed by centrifugation (Thermo Scientific Sorvall Legend X1 with High Conic II rotor) at 10000 g for 10 mins to remove unexfoliated material. The supernatant was discarded and the sediment was redispersed into fresh surfactant solution and subjected to probe sonication at 60% amplitude for 3 hours, followed by centrifugation at 10000 g for 20 mins. The sediment was redispersed into 3 mL of fresh sodium cholate solution to give the first sample and the supernatant was collected for the further centrifugation at 10000 g for 1 and 16 hours with sediment redispersed at each stage to give a series of narrowly size selected dispersions. UV-visible extinction spectroscopy was performed using a Shimadzu UV3600Plus spectrometer.

A.3 Methods for Chapter 6

Exfoliation and emulsification

MoS_2 and BN powders were purchased from Sigma Aldrich. Graphite powder was provided by Zenyatta Ventures Ltd. MoS_2 was subjected to an initial sonication-centrifugation step to remove impurities and very small nanosheets; the bulk powder was added to 30 mL of cyclopentanone (CPO) at an initial concentration of 25 g/L and sonicated using a Sonic Vibra-cell VCX130 at 60% amplitude for 1 hour under ice bath cooling. The dispersion was centrifuged (Thermo Scientific Sorvall Legend X1 with High Conic II rotor) at 5000 g for 5 mins, the supernatant containing the impurities and very small nanosheets was the discarded and the sediment was redispersed into 30 mL of fresh CPO. Graphite and BN powders were added to 30 mL of cyclohexanone (CHO) at an initial concentration of 25 g/L. The subsequent sonication step used was the same for MoS_2, graphite and BN; sonication using a Sonic Vibra-cell VCX130 at 60% amplitude for 3 hours under ice bath cooling. MoS_2 dispersions were centrifuged at 5000 g for 5 mins and graphene and BN dispersions were centrifuged at 5000 g for 30 mins. This typically yields dispersions of nanosheets with $\langle N \rangle < 10$ for

all materials, as confirmed with spectroscopic metrics by UV-visible extinction spectroscopy (Shimadzu UV3600Plus spectrometer). Extinction spectroscopy was also used in conjunction with previously measured extinction ceofficients to determine concentration of these dispersions. Concentrations for these processing conditions are typically ∼0.1 g/L. These cycloketone dispersions can be emulsified with deionised water by transferring to silanised vials and adding water at ∼1:10 by volume followed by vigourously shaking by hand to homogenise. This gives nanosheet-stabilised water droplets which sediment through the cycloketone continuous phase. These droplets were collected and deposited on PET to perform statistical measurements of average droplet diameter by optical microscopy (Olympus BX53-M optical microscope). In order to measure droplet size as a function of nanosheet volume fraction, the stock dispersion were diluted with cycloketone and fixed volume was emulsified with fixed volume of water to control droplet size while maintaining a fixed volume of droplets. These samples were transferred into channels milled into PTFE with copper tape contacts to allow electrical measurements using a Keithley 2600 sourcemeter. I-V characteristics were obtained and resistances normalised to channel dimensions to calculate conductivity. For Raman mapping of deposited droplets, samples were deposited onto silicon wafers and their Raman spectra were mapped using a Renishaw inVia Raman microscope with 660 nm excitation using a x50 objective. Indicative layer number distributions were calculated by mapping the A_1g and E^1_{2g} mode separation and converting to layer number based on the relationship established for mechanically-exfoliated MoS_2 [187].

Solvent transfer and emulsion inversion

In order to prepare emulsions stabilised by well-exfoliated nanosheets in solvents which are conventionally considered poor for LPE, cycloketone dispersions were subjected to further centrifugation of 10000 g for 16 hours to result in sedimentation of almost all of the dispersed nanosheets. The cycloketone supernatant was discarded and the sediment redispersed into a new oil phase such as pentane, hexane, ethyl acetate, methyl methacrylate, dichloromethane or styrene. These oil phases span

the range of surface energies of water-immiscible organic solvents and are immiscible with alternative high surface energy water phases; ethylene glycol and formamide (with the exception of ethyl acetate-formamide). As such, these combinations were used to identify emulsion orientation and stability, as shown in Figure 6.8. The solvent-transferred dispersions were emulsified with ethylene glycol, formamide and water at 1:1 by volume (to ensure sufficient oil and water phase to stabilise either orientation of emulsion) and their orientation determined by identifying buoyancy and/or stability on glass or silanised vials or at the air interface, as shown in Figure 6.6. These orientations were used to verify the surface energy model presented in Chapter 6 and found to be identical for graphene, MoS_2 and BN emulsions whether exfoliated or bulk material was used. In order to perform the inversion experiment shown in Figure 6.9, a CHO dispersion was diluted to varying volume fractions of pentane and the mixed solvent dispersion emulsified with water and orientation determined. Samples between which the emulsion orientation inverted were used to calculate a range for the surface energy of the nanosheet films.

Emulsion inks

Water-in-cycloketone emulsions of graphene and MoS_2 were prepared as described above. Samples were deposited by onto PET substrate heated to 80 °C by manual drop casting of ∼0.1 mL (per pass) of densely-packed emulsion over an area of ∼1 cm^2. The sheet resistance was measured using a Keithley 2600 sourcemeter after every deposition pass. Once dry, another 0.1 mL was deposited and this was repeated until optical microscopy showed the films to have nearly complete area coverage, around 5 passes as shown in Figure 6.10. At this stage, AFM was performed using a Bruker Dimension Icon with ScanAsyst-Air probes to measure topography and determine approximate thickness per pass. The deposition process was repeated until the sheet resistance began to decrease with the reciprocal of pass number, indicating that the thickness-independent bulk-like conductivity regime had been reached. Preliminary rheological measurements were performed using a TA Instruments AR2000 rheometer with PMMA parallel plates.

Emulsification of surfactant-exfoliated nanosheets and basic inversion

For the proof-of-concept emulsification of surfactant-exfoliated nanosheets, dispersions were prepared using the exfoliation parameters described above on dispersions of graphene, MoS_2 or BN in 0.25 g/L aqueous Triton X-100 solution, which yields a dispersion with the minimal amount of surfactant, likely bound to the sheets rather than free in dispersion. Surfactant concentration of 0.1 g/L was found to result in significantly reduced concentration, while dispersions produced by exfoliation at higher surfactant concentration required washing by vacuum filtration and redispersion in order to allow stable emulsification. For the emulsion inversion by basic deprotonation, cycloketone dispersions were prepared and emulsified with pH 13 KOH solution, resulting in formation of buoyant oil droplets in a continuous phase of the basic solution, which are stabilised when a sacrificial layer of droplets have burst and coated the air/water interface. Surfactant exfoliation and basic inversion can also be achieved by blending aqueous surfactant dispersions of nanosheets with KOH solution followed by emulsification with an arbritrary oil phase.

A.4 Methods for Chapter 7

Exfoliation and deposition

Exfoliation of MoS_2 in CPO was performed as described in A.3 with the centrifugation procedure modified depending on the experiment. The standard single-step centrifugation used for loosely size selected experiments was 5000 g for 5 mins with the supernatant collected and the sediment discarded. For size selection experiments, liquid cascade centrifugation was performed with centrifugation conditions given in the relevant sections below. In either case, dispersions were prepared at or diluted concentrations around 0.1 g/L. Langmuir deposition was performed with a NIMA 102A Langmuir trough equipped with a platinum Wilhelmy plate with subphase area $\sim$75 cm^2 and a transparent window to allow mounting on a Leica spotting microscope with x10 and x30 magnification to allow monitoring of film formation. For the spreading experiments, the behaviour of each solvent studied was established by

adding a 5 µL droplet from a micropipette onto a pristine water surface. Spreading solvents rapidly spread out over the surface and evaporate within several seconds under ambient conditions. Non-spreading solvents pool into one or more droplets and evaporate at a significantly slower rate, even for comparable boiling points to spreading solvents. To prepare an amphiphilic monolayer film, arachidic acid was dissolved into chloroform at ∼1 g/L concentration. 10 µL of the solution was spread onto the surface of the Langmuir trough. The isotherm of Figure 7.3 was obtained by closing the barriers at a rate of 10 cm^2/min with a target surface pressure of 30 mN/m. To measure the maximum spreading pressure of each solvent, the barriers were initially fully opened. The surface pressure was controlled in increments of 3 mN/m, and at each increment a 5 µL droplet of pristine solvent was added to the surface for observation. Each solvent was tested separately, with the trough water and arachidic acid film replaced in between solvent tests. Deposition of MoS_2 films was performed by drop-wise addition of the ∼0.1 g/L dispersion onto the water subphase with ∼0.1 mL deposited before cycling the barriers to homogenise the film before depositing more material and ∼2 mL of dispersion typically deposited to give high area coverage as confirmed by *in situ* optical microscopy after compression to 25 cm^2. Samples were transferred onto glass microscope slides of PET by the Langmuir-Schaefer horizontal deposition technique. Film morphology and sample thickness was characterised by AFM (Bruker Dimension Icon with Scan-Asyst Air probes). Films were further characterised by SEM using a Zeiss SIGMA field emission gun scanning electron microscope with Zeiss in-lens secondary electron detector. The working conditions used were 1.0 kV accelerating voltage, 20 µm aperture, and 2.8 mm working distance.

Spectroscopy

Samples for spectroscopic studies were prepared by liquid cascade centrifugation at 5000 *g* with sediments collected and supernatants subjected to the subsequent step at the following times: 2, 4, 8, 16 and 32 mins. Dispersions were diluted to suitable concentrations and characterised by UV-visible extinction spectroscopy using

a Shimadzu UV3600Plus spectrometer in quartz cuvettes with CPO reference sample. Dispersions were deposited as Langmuir films as described above with the deposited volume varied to give high area coverage to allow characterisation by UV-visible spectroscopy, as shown in Figure 7.7.

Electrical characterisation

Langmuir films were prepared as described above and deposited onto PET substrates with 30 nm sputtered gold bar electrodes (l/w $\sim$ 5) with part of the electrode area masked with Scotch tape to allow direct contact for electrical measurements. I-V characteristics were measured with a Keithley 2600 sourcemeter with potential difference -20 to 20 V. Photoconductivity measurements were performed under broadband illumination as a function of intensity with a Newport 92193H-1000 solar simulator. Samples for non-Langmuir deposition techniques were prepared using the same procedure as for the CPO exfoliation but instead using NMP or aqueous Triton X-100 solution (0.25 g/L) as the dispersant. NMP-exfoliated MoS_2 was deposited by vacuum filtration and surfactant-exfoliated MoS_2 was deposited by spray deposition. Sheet resistance and film thickness were measured to determine conductivity, shown in Figure 7.11. For the size-dependent conductivity experiment, liquid cascade centrifugation was performed on surfactant-exfoliated MoS_2 dispersions at 5000 g with sediments collected and supernatants subjected to the subsequent step at the following times: 2, 5, 10, 30 and 90 mins. The average nanosheet length $\langle L \rangle$ was measured using the spectroscopic metric and samples were spray coated to thicknesses >500 nm to allow measurement by focus-encoded optical microscopy.